Hierarchical Mechanics of Functional Amyloid Protein Based Materials

by

Max Isaac Solar

B.S., University of Pennsylvania (2009)

Submitted to the Department of Materials Science and Engineering
in partial fulfillment of the requirements for the degree of

Doctor of Philosophy

at the

MASSACHUSETTS INSTITUTE OF TECHNOLOGY

February 2015

Author .....
Department of Materials Science and Engineering
October 8, 2014

Certified by .....
Markus J. Buehler
Professor of Civil and Environmental Engineering
Thesis Supervisor

Certified by .....
Alfredo Alexander-Katz
Associate Professor of Materials Science and Engineering
Thesis Reader

Accepted by .....
Donald Sadoway
Chair, Department Committee on Graduate Theses

Hierarchical Mechanics of Functional Amyloid Protein Based Materials

by

Max Isaac Solar

Submitted to the Department of Materials Science and Engineering
on October 8, 2014, in partial fulfillment of the
requirements for the degree of
Doctor of Philosophy

Abstract

Amyloid and amyloid-like proteins are a broad class of misfolded protein structures known for their their roles in a variety of neurodegenerative diseases, but also for their impressive mechanical properties and their propensity to self-assemble at diverse length scales. These properties make amyloid and amyloid-like proteins excellent candidate materials for the design of engineered functional biomaterials. However, many of the fundamental structure-property relationships which could guide the design of amyloid-based functional materials for various applications are not well understood. In this thesis, a multiscale modeling and simulation approach is used to investigate these structure-property relationships at multiple length scales. Full atomistic simulations are used to study the tensile and bending response of single fibrils, as well as the inter-fibril interaction strength. It is found that in tension, the specific geometry of the fibrils does not significantly influence the deformation behavior, but the mechanical properties, most notably the tensile strength, depends strongly on the areal density of hydrogen bonds in the fibril cross-section. The mechanical response at the molecular scale is used to guide the development of a coarse-grained description of amyloid and amyloid-like fibrils. Next, the adhesive behavior of amorphous polymers is studied to identify design principles which enhance adhesive performance and could be applied to aid in the design of amyloid-based adhesives, an exciting potential functional role for amyloid-based biomaterials. Finally, mesoscale structures are investigated including a nanowire-like geometry and adhesive films. These studies demonstrate that the mechanics of larger scale amyloid based structures are largely determined by the inter-fibril interactions; the specific intra-fibril properties become less significant at larger scales. The results presented in this thesis form the foundation for the development of basic materials selection criteria to aid in the design of functional amyloid-based biomaterials for diverse applications.

Thesis Supervisor: Markus J. Buehler
Title: Professor of Civil and Environmental Engineering

Acknowledgments

There are so many individuals to whom I am thankful for providing me with seemingly endless support throughout my journey here at MIT.

I would like to thank my advisor, Professor Markus Buehler for welcoming me into his group and for providing guidance and support while also allowing me the freedom and flexibility to find my own path as a researcher. I would also like to acknowledge the members of my thesis committee, Professor Lorna Gibson and Professor Alfredo Alexander-Katz. Funding for this work was provided by the National Science Foundation, the Office of Naval Research, and by the Henkel corporation.

I am indebted to all of the members of the Buehler group, both past and present, for providing so much guidance and mentorship throughout the past three plus years. In particular, I would like to thank Steven Cranford, Graham Bratzel, Tristan Giesa, Leon Dimas, and Dieter Brommer for always being around to share and discuss ideas and and also for making our office such an enjoyable and fun place to spend my working hours.

I would never have made it through MIT had it not been for my incredible group of friends. Most notably Adam Jandl, Neil Patel, Jocelyn Newhouse, Brian Spatocco, Tom Fellows, Reid Van Lehn, and Dan Harris have always been there to support me in so many different ways. From Friendsgiving, Pumpkinfest, cabin and ski trips, to just hanging out at the Muddy on Friday evenings, these past five years have truly been the most fun years of my life. I never expected to form such deep friendships at MIT and I will always be thankful for the fun we have had together and the memorable life events we have celebrated together.

I am very thankful to my family - my mom and stepfather Vickie and Tim, my dad and stepmother Ron and Sharyl, and my sisters Sophie and Mara - for supporting and encouraging me throughout my (long and now continuing) education. All of you have always made sure I knew how proud you are of me and the work that I have done. I am also thankful to my east coast family - Corinne and the rest of the Siegels and Glassmans etc. - for welcoming me into their family and making sure that I have had another place to call home just a few short hours drive from Boston.

Last (but certainly not least), I am forever thankful to my beautiful and wonderful wife Emily. Over the past five plus years she has been more patient, understanding, and supportive than I knew it was possible for a person to be. Emily, I am so grateful that I have had you by my side; I would not have made it through the sometimes turbulent journey that is a PhD program at MIT without your incredible support and encouragement, and for always believing in me. Thank you buddy.

Contents

List of Figures

List of Tables

Chapter 1

Introduction and Motivation

The goal of this thesis is to provide fundamental insights into the structure-property relationships in amyloid and amyloid-like protein based materials across multiple length scales, which will inform and enable the future development of novel functional biomaterials. This chapter provides background on amyloid and amyloid-like proteins including their general structural features and mechanical properties, as well as a description of the pathological, and more importantly in the context of this thesis, functional roles, of these proteins in both natural and engineered structures.

1.1 General Features of Amyloid and Amyloid-Like Proteins

Amyloid proteins are broad class of proteins that may undergo a structural transformation from their native, functional folded state, into structures that self-assemble into highly organized, insoluble fibrilar structures. This process is illustrated schematically in Figure 1-1 [1]. During this transformation, the proteins lose their native form and functionality and take on a β-sheet rich structure (the amyloid form) which has new properties and functions. The specific structural details of the amyloid form as well as the resulting properties are discussed in more detail below (see Sections 1.1.1 and 1.1.2).

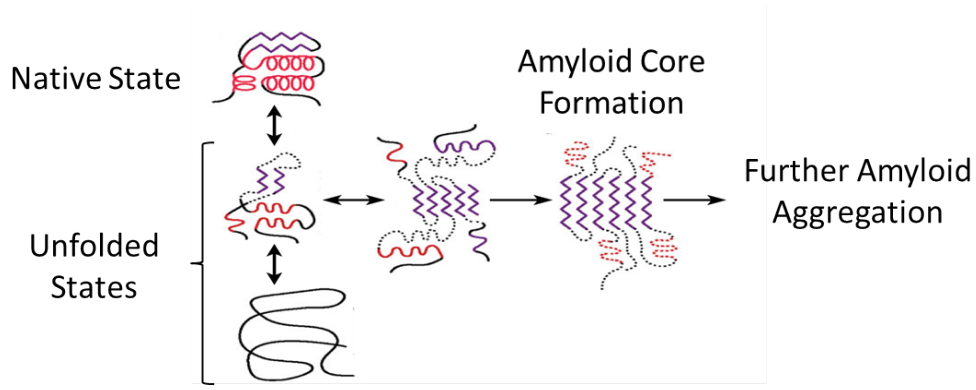

Figure 1-1: A schematic representation of a possible process by which an amyloid fibril is formed. A small β-sheet region which results from a misfolding event can promote further folding into the amyloid form which eventually leads to the formation of an amyloid fibril. β-sheet regions are indicated by purple color; figure adapted with permission from [1].

Amyloid proteins have garnered much interest in the past few decades mostly due to their roles in a wide variety of diseases, [1–7]; the role of amyloid proteins in pathological roles such as these will be discussed briefly below in Section 1.2.1. More recently, however, there is considerable and growing excitement over the utilization of amyloid and amyloid-like proteins in functional roles [4, 5, 8–11]. This excitement stems from both the discovery of diverse natural functional roles for amyloid protein fibrils as well as the characterization of their intrinsic structural and mechanical properties. Amyloid and amyloid-like fibrils feature impressive mechanical properties as well as a high propensity for self assembly, making them excellent candidate materials for building blocks of engineered functional biomaterials.

1.1.1 Structural Characteristics

Amyloid and amyloid-like proteins are defined by a set of common structural features, most importantly the so-called cross-β secondary structure. Beyond this secondary structural structural motif, however, amyloid and amyloid-like proteins (and superstructures comprising these proteins) exhibit a rich hierarchical structure extending from the atomic scale up to the centimeter scale.

Cross-β Secondary Structure

The cross-β secondary structure is the primary structural feature which is shared by all amyloid protein fibrils. This structure is defined by individual β-strands oriented perpendicular to a fibril axis, resulting in the formation of a dense hydrogen bonded network which extends the entire length of a fibril [2, 3, 12–14]; the cross-β motif is shown schematically in Figure 1-2. In this thesis, an amyloid-like protein fibril is defined as any protein structure which exhibits this cross-β structure in a fibril-like geometry.

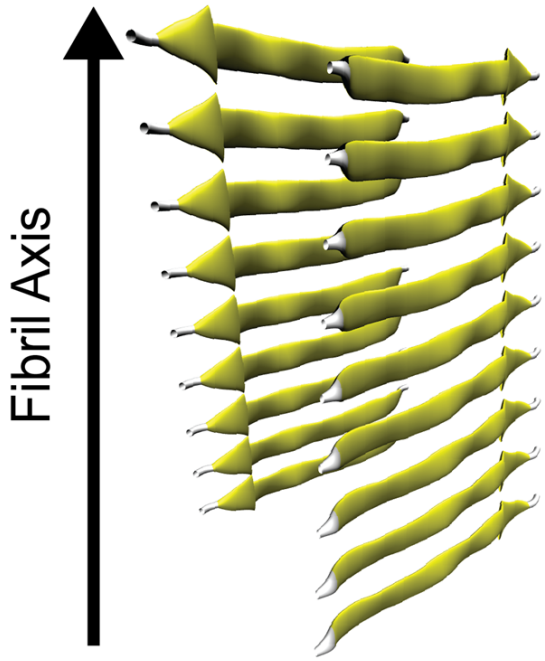

Figure 1-2: Schematic of the cross-β secondary structure found in amyloid and amyloid-like protien fibrils. Individual β-strands (represented by yellow arrows) are oriented perpendicular to the fibril axis resulting in β-sheet structures which span the length of the protien fibril.

In the context of functional amyloid based materials, the cross-β structure provides the foundation on which many of the remarkable properties of amyloid protein fibrils originate, most notably the mechanical properties discussed below in Section 1.1.2. These mechanical properties derive from the clustering of hydrogen bonds in the β-sheets which results in a cooperative effect that mitigates the innate weakness of

the individual hydrogen bonds [15, 16]. However, it is noted that since the cross-β structure effectively creates a single extended β-sheet crystal, amyloid fibrils tend to be rather brittle. This brittleness is found to be an important feature which controls the growth kinetics of amyloid fibrils [5, 17, 18], but it presents a possible barrier in utilizing amyloid and amyloid-like materials as structural building blocks in new biomaterials.

Hierarchical Structure

Another defining feature of amyloid and amyloid-like protein materials is a rich hierarchical structure, spanning length scales from angstroms to hundreds of microns or even centimeters [4, 5, 11, 19, 20]. At the smallest length scales, hydrogen bonding between domains in protein chains results in the formation of β-strands which further organize into the typical β-sheet structure over short length scales, thus forming oligomers or protofibrils. These small structures grow into longer fibrils which in turn come together and form large scale structures such as plaques or films. Importantly for the facile design and manufacture of amyloid based biomaterials, these hierarchical structures form naturally through various self-assembly processes at the different length scales. The hierarchical structure of amyloid and amyloid-like materials is illustrated in Figure 1-3 [11].

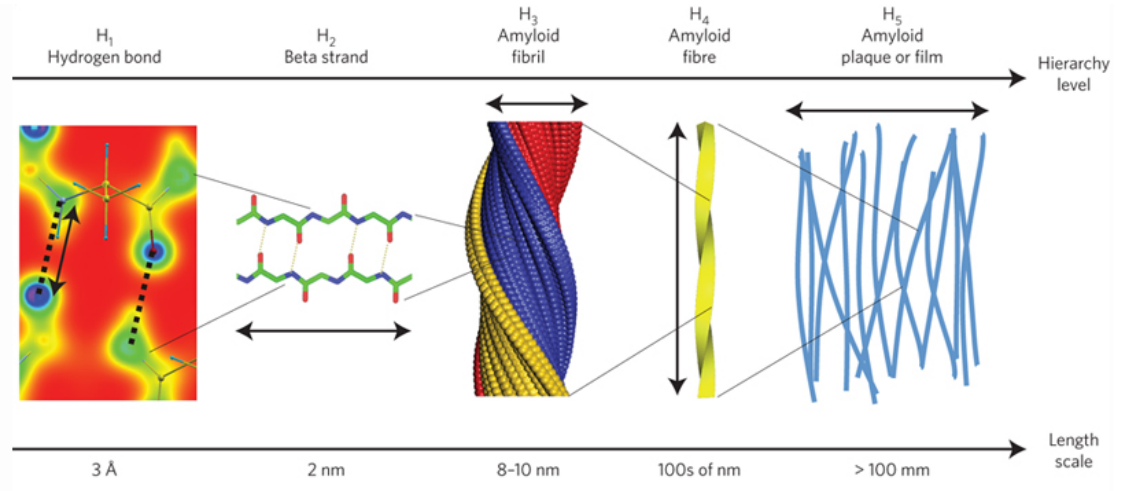

Figure 1-3: Amyloid and amyloid-like protiens feature a rich hierarchical structure with organization from the atomic to micrometer scale and larger. Figure reprinted with permission from [11].

1.1.2 Mechanical Properties

Much of the interest in the functional roles of amyloid and amyloid-like protein fibrils has its origin in their excellent mechanical properties; they are among the strongest and stiffest purely proteinaceous materials known with Young's moduli in the range of 10-30 GPa and a tensile strength on the order of 100s of MPa [21–27]. Figure 1-4(a) shows an Ashby plot of the strength and modulus of a variety of biological and inorganic materials [5]; amyloid proteins are second only to silks in overall performance of purely proteinaceous materials. Amyloid proteins have also been shown to feature very high bending rigidities relative to their cross-sectional moments of inertia; as shown in Figure 1-4(b) their performance approaches that of covalently bonded materials even though their strength is derived from weak hydrogen-bonded interactions.

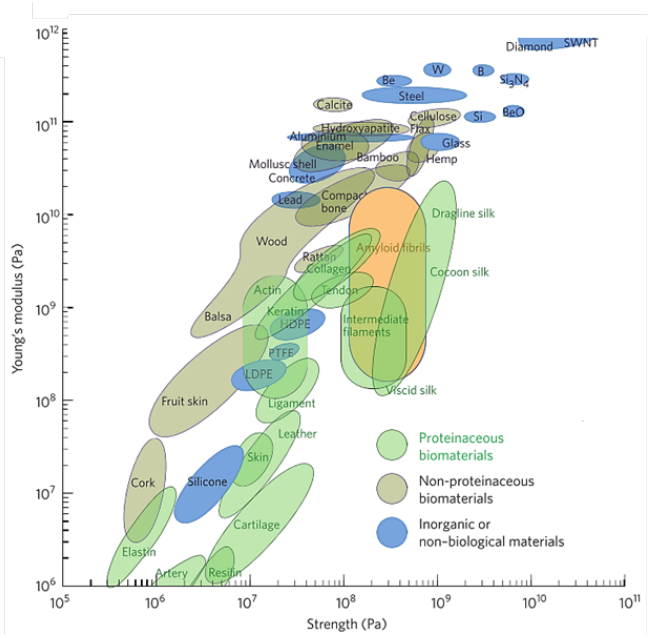

(a)

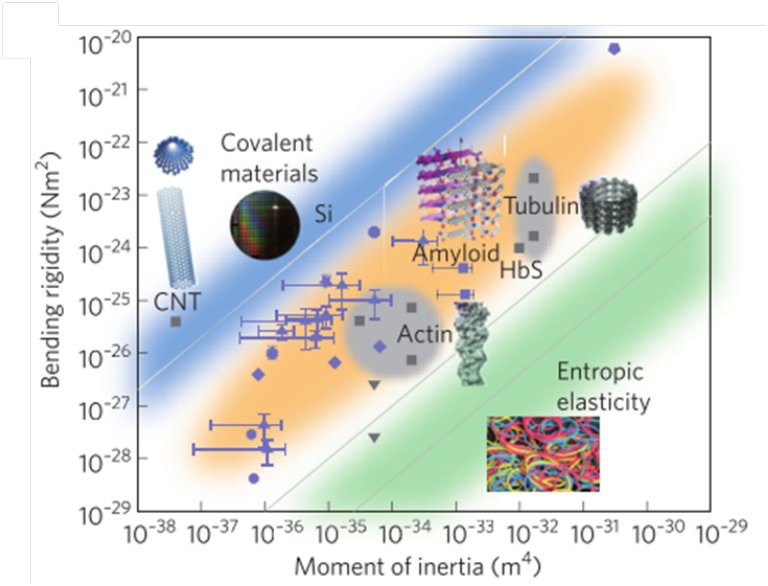

(b)

Figure 1-4: (a) shows an Ashby plot of the strength and modulus of a variety of purely proteinaceous biomaterials, non-proteinaceous biomaterials, and inorganic materials; the properties of amyloid fibrils are highlighted in orange. Amyloid fibrils are clearly among the strongest and stiffest purely proteinaceous materials, second only to silks in overall performance. (b) demonstrates that the bending rigidity of amyloid fibrils approaches that of materials with much stronger bonding for a given moment of intertia, again illustrating that amyloids are impressive materials in terms of their mechanical properties. Figures reprinted with permission from [5].

1.1.3 Diversity of Amyloid and Amyloid-Like Structures

One of the major challenges in understanding the structure-property relationships of amyloid and amyloid-like protein based materials lies in the diversity of amyloid and amyloid-like structures. There are dozens of known amyloid structures [5, 7, 28], and it has been suggested recently in the literature that the amyloid form is a more general structure that a large fraction of all proteins may be capable of forming [29]. Some of the diverse structures exhibited by amyloid and amyloid-like proteins are shown in Figure 1-5; structures vary from simple stacked β-sheet structures in either parallel or anti-parallel arrangements to β-helical structures, to even structures which combine these two motifs. Furthermore, single protein sequences have been found to exhibit multiple polymorphic structures, such as the two-fold and three-fold symmetric arrangements of the Aβ (1-40) amyloid fibril (shown in the bottom right of Figure 1-5).

This diversity stems from the different amino acid sequences that comprise the primary structure of the proteins; each sequence gives rise to a different secondary structure which can range from simple stacked β-sheet or β-helical arrangements to more complex combinations of those simple motifs. In different pathological and functional roles (discussed below) these structures have evolved to fulfill a specific biological requirement. However, although all of the amyloid or amyloid-like fibrils possess the same cross-β motif which provides the foundation for their excellent mechanical properties (and also enables various functional roles), the specific structure-property relationships in these materials remain poorly understood, and there are no clear guidelines for choosing or engineering an optimal amyloid or amyloid-like fibril for a specific application.

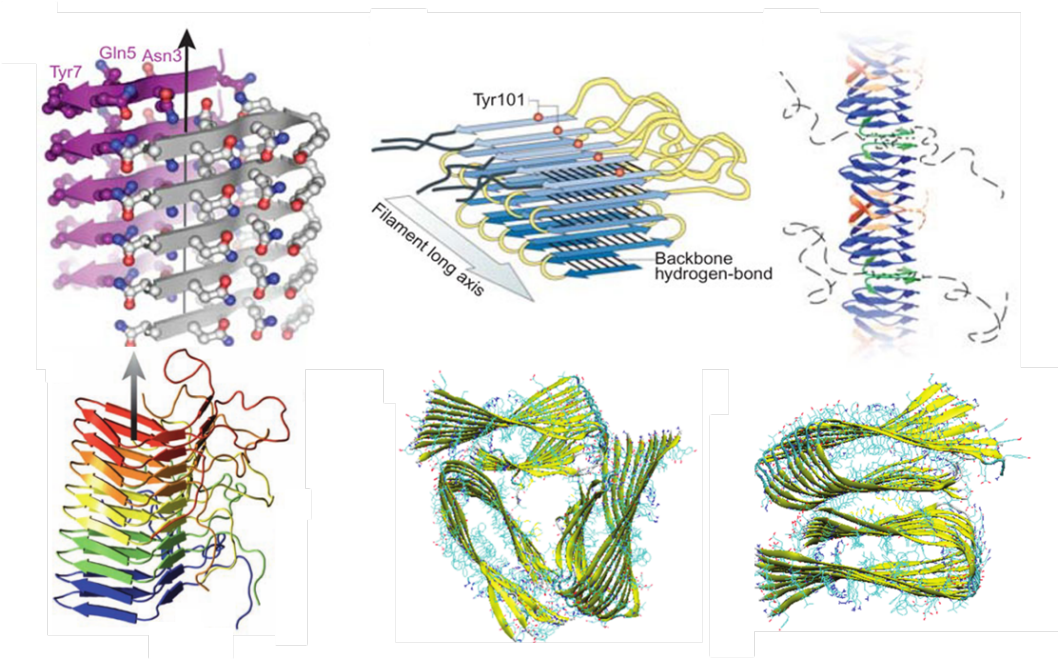

Figure 1-5: Many different proteins are capable of forming amyloid or amyloid-like structures, and the geometries realized by these proteins are quite diverse; the six different structures shown here illustrate this idea. This presents a challenge in a materials selection context; geometric and structural features which optimize the properties of functional amyloid based materials have not been identified. Figure adapted with permission from [30–32].

1.2 Roles in Nature

1.2.1 Pathological Roles

As mentioned above, amyloid and amyloid-like proteins are most (in)famous for their role in a variety of diseases, most notably Alzheimer's disease, but also Parkinson's disease, Type II Diabetes, and a host of prion related diseases such as Cruetzfeld-Jakob disease and "Mad Cow" disease [1–7]. The scope of these pathological roles is very large and growing. In 2006, Alzheimer's disease affected 26.6 million people worldwide, and its prevalence is expected to grow to 1in every 85 people by the year 2050, and Parkinson's disease is the next most prevalent neurological disease following Alzheimer's [33, 34].

The common feature in many of these diseases is the formation of insoluble fibrilar protein aggregates in both the intra- and intercellular spaces in various body tissues. In Alzheimer's disease, for example, the incorrect folding of a normally soluble protien (Aβ) results in the formation of insoluble amyloid fibrils which aggregate into large micrometer scale plaques (senile plaques) in the brain tissue (shown in Figure 1-6 [35]). These plaques disrupt the normal neurological pathways in the brain and eventually cause nerve cell death, leading to irreversible memory loss and dementia. Furthermore, it has been shown recently that even small oligomers formed from the Aβ and similar proteins are neurotoxic and can be a major contributing factor to the symptoms experienced in Alzheimer's disease [36–38] .

The scope of this thesis (discussed below in Section 1.4) is limited to investigating amyloid-based materials in functional roles, and thus the understanding amyloids in the context of aiding in the treatment of diseases lies outside of this scope. However, furthering the understanding of structure-property relationships in amyloid proteins could provide some important insights into the fundamental behaviors of amyloid fibrils thus and have a large impact on the development of new drugs and therapies to combat amyloid-related diseases.

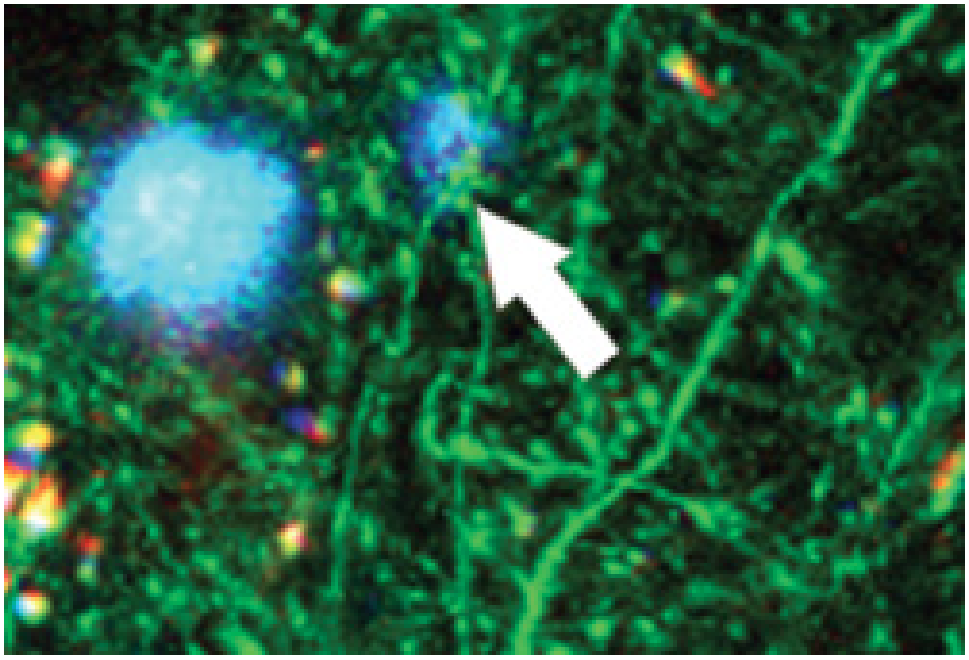

Figure 1-6: An image showing neurons (green) and two amyloid (Aβ) plaques (blue) in mouse brain tissue. Figure reprinted with permission from [35]

1.2.2 Natural Functional Roles

In addition to their various pathological roles, naturally occurring amyloid and amyloid protein fibrils also play a variety of functional roles. Examples of natural functional amyloid based materials include adhesive films, bacterial biofilms and coatings, catalytic scaffolds, and structures for storage of hormones [4, 5, 8–10, 39–44]. An example of an amyloid biofilm produced by the *E. coli* bacteria is shown in Figure 1-7 [5,44]; this film aids in host cell adhesion and also provides resistance to desiccation. The existence of these types of natural functional roles for amyloid and amyloid-like proteins indicates that the amyloid structure is not simply a misfolded, pathological state. Amyloids are also structures which are carefully designed by nature to take advantage of a few distinct structural motifs in order to provide function in wide variety of roles and environments.

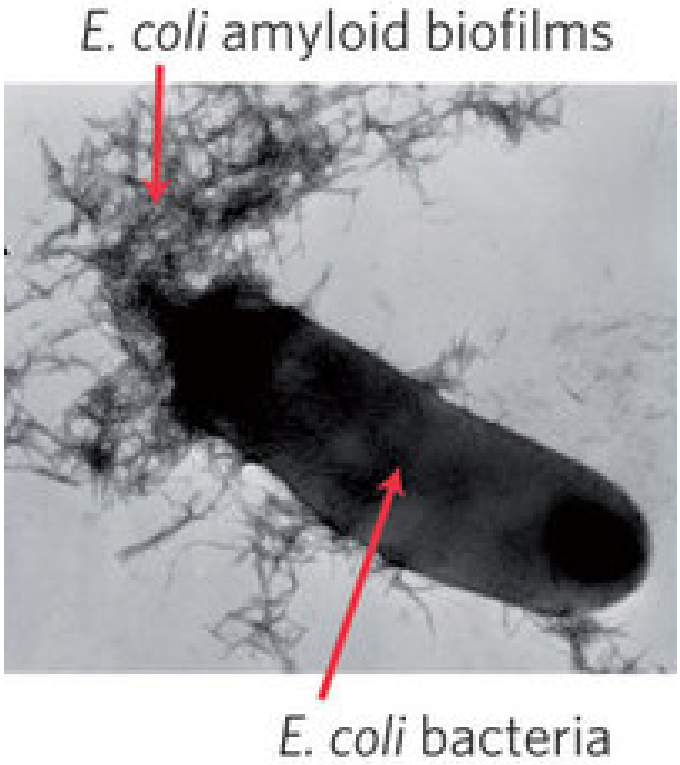

Figure 1-7: A micrograph of a functional amyloid-protein based bacteriral biofilm produced by the *E. coli* bacteria. The film comprises curli fibers which aid in adhesion of the bacteria to host cells and also provide resistance to desiccation. Figure reprinted with permission from [5].

1.3 Functional Amyloid-Based and Amyloid-Inspired Biomaterials

Perhaps more exciting than the discovery of natural functional amyloid-based materials is the advent to engineered amyloid biomaterials which take advantage of the unique combination of properties present in amyloid and amyloid-like structures. The innate capacity of amyloids to self-assemble into highly organized structures over diverse length scales makes amyloids an excellent candidate material for the bottom-up design and fabrication of novel biomaterials. Examples of how amyloids have already been utilized include the fabrication of templates for conducting nanowires and organic photovoltaics, as well as mechanically robust biofilms [5, 19, 45–47]. There is also considerable interest in exploiting the intrinsic "stickiness" of amyloid fibrils to design engineered amyloid based adhesives which could have applications in a variety of environments.

By controlling the structure of the proteins at the atomic scale through functionalization or the introduction of mutations [48], and also by controlling the aggregation and assembly process via environmental conditions such as pH or temperature, a diverse set of materials with highly tunable properties can be fabricated from a small set of universal building blocks. This idea is captured schematically in Figure 1-8 [5]. In order to fully realize this idea, however, a more complete understanding of the fundamental properties of the constituent amyloid fibrils (the basic building blocks) is required.

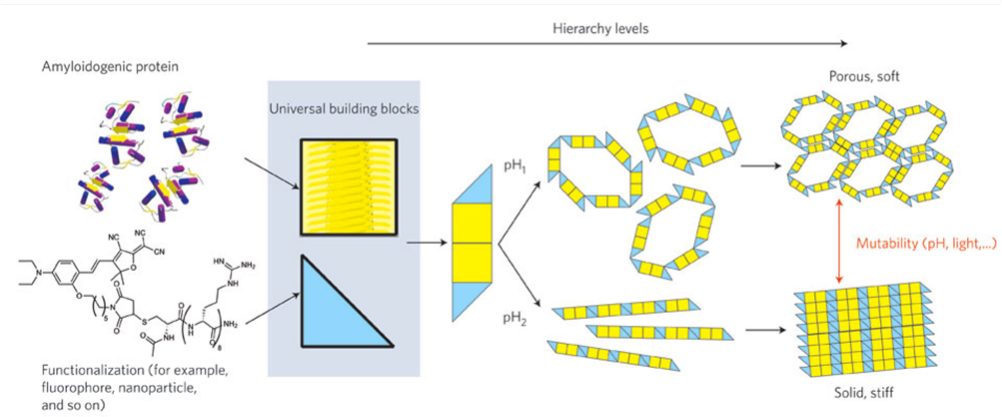

Figure 1-8: Amyloid proteins can be used as universal building blocks in the design of new materials. By using different amyloid or amyloid-like protein fibrils, functional groups, and processing condtions, a diverse set of structures and materials can be realized from a small set of building blocks. Figure adapted with permission from [5].

Amyloid and amyloid-like protein fibrils can also be combined with other natural or synthetic components to produce nanoscale composite materials that have interesting and desirable properties. One such composite structure is a graphene-amyloid nanocomposite, shown in Figure 1-9 [49, 50]. This structure exhibits tunable mechanical properties, shape-memory behavior, and enzyme sensing capabilities. By incorporating amyloid protein fibrils directly into the composite structure, many of the properties and characteristics that arise from the complex, multiscale structure of the amyloids is captured in the composite. However, given the immense diversity of amyloid and amyloid-like structures (see Section 1.1.3), there is much room for improvement and optimization in terms of choosing the best amyloid or amyloid-like protein for a given composite structure (and a given application of that composite). Even without such optimization, it is clear that amyloids have an immense amount of potential for the development of a new generation of novel biomaterials and nanocomposites.

1.3.1 Synthetic Amyloid-like Structures

In addition to utilizing naturally occurring amyloid and amyloid-like protein structures in engineered functional biomaterials, new synthetic structures are being devel-

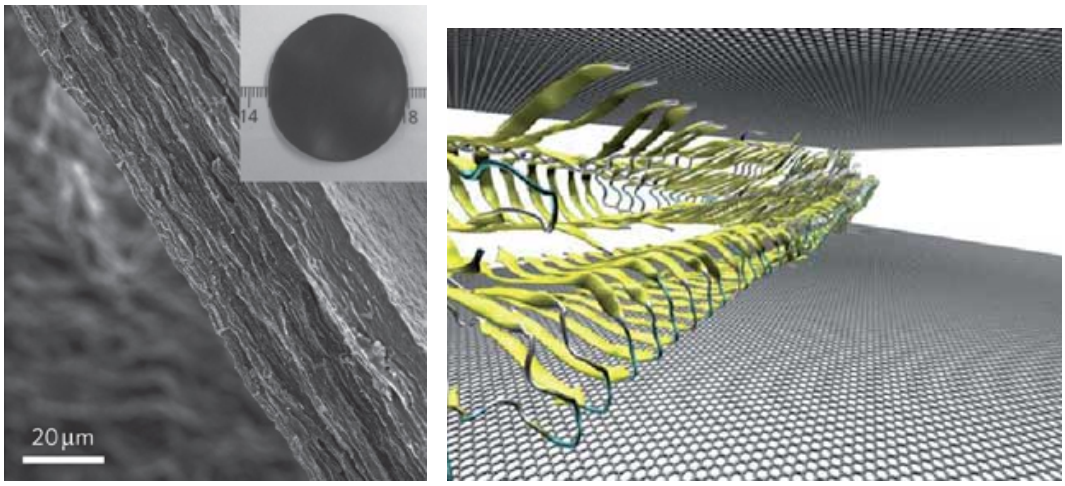

(a) (b)

Figure 1-9: A graphene-amyloid nanocomposite structure. (a) shows an SEM image of a film comprising the composite structure, and (b) shows a cartoon representation of the molecular scale structure of such a nanocomposite. (a) reprinted with permission from [49].

oped which are *inspired* by the cross-β structure of amyloid proteins. One common class of these structures are cyclic peptide nanotubes, such as the structures shown in Figure 1-10 [51–53]. These structures are designed to form hydrogen bonds between rings which stack and form β-sheet like structures extending up the fiber or nanotube axis. Furthermore, they can be readily functionalized with various polymer side-chains can influence their assembly and also allow for the engineering of the interactions between nanotubes. These structures offer an exciting opportunity to take what is learned from amyloid and amyloid-like protein structures and create engineered bioinspired materials with highly tunable properties.

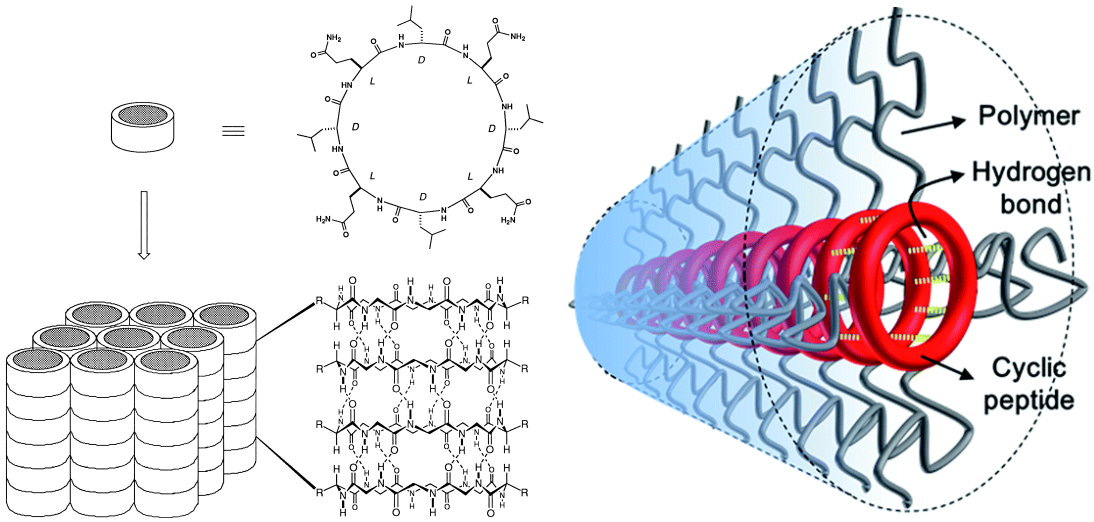

(a) (b)

Figure 1-10: Synthetic cyclic peptides stack are stabilized by hydrogen bonds which result in the formation of a cross-β-like structure similar to that of amyloid and amyloid-like protein fibrils. (a) shows a schematic of a cyclic peptide structure as well as an assemble of multiple nanotubes, and (b) illustrates how the cyclic peptides can be functionalized with polymer chains to influence their assemble and interactions between nanotubes. (a) reprinted with permission from [51], (b) reprinted with permission from [53].

1.4 Aim of the Present Study

As alluded to in the above discussion, the goal of this work is to improve the understanding of fundamental structure-property relationships in amyloid and amyloid-like protein materials, with a specific focus on functional applications of these materials. Specifically, the key topics that will be addressed in the present study are:

1. Furthering the understanding of specific structure-property relationships in amyloid proteins and amyloid-based materials across multiple length scales.

2. Identifying deformation mechanisms and mechanical properties which enhance the performance of functional amyloid-based structures (and similar functional materials).

3. Directly investigating the mechanical response of functional amyloid-based struc-

tures.

4. Beginning the development of a set of materials selection criteria to allow for the more effective utilization of amyloid and amyloid-like proteins in engineered biomaterials.

1.4.1 Approach and Outline

A multiscale modeling and simulation approach is used in this thesis to address the points listed above. This approach, discussed in more detail in Chapter 2, is well suited to systematically study mechanical properties and deformation behavior at both the molecular scale (via atomistic simulation) and at the micron and larger scales (via coarse-grained, mesoscale modeling and simulation).

This thesis is organized as follows: Chapter 2 provides some general background on the modeling and simulation techniques used throughout this work. In Chapter 3, atomistic scale simulations are used to investigate the mechanical behavior of various amyloid and amyloid-like protein fibrils under different boundary conditions including tension, bending, and inter-fibril shear. Chapter 4 integrates the results of these simulations into a new coarse-grained description of amyloid and amyloid-like protein fibrils which can be used to study a variety of amyloid-based structures. In Chapter 5, a model for polymer adhesion is discussed; while not a direct study of amyloid-based structures, the results from the study are general and can be applied to guide the development of functional amyloid materials, and the methods developed to study the polymer adhesives can be directly applied to study amyloid-based adhesives. Chapter 6 presents two studies of mesoscale amyloid structures using the model developed in Chapter 4, and compares the results for structures based on two distinct amyloid and amyloid-like fibrils with very different intrinsic properties. Finally, Chapter 7 summarizes the major findings of this work and provides some suggestions for future research based on this thesis.

1.5 Chapter Summary

Their impressive mechanical properties, combined with their high propensity for self assembly at multiple length scales, makes amyloid and amyloid-like proteins excellent candidate materials for the design of new biomaterials. Specific structure-property relationships in these proteins have not been studied extensively, and thus clear materials selection guidelines which could aid in optimizing the performance of new amyloid-based functional materials have not been suggested. This thesis investigates amyloid and amyloid-like structures using a multiscale modeling approach in order to elucidate these structure-property relationships and aid in the design of *de novo* amyloid-based biomaterials.

Chapter 2

Methodology

This chapter provides a brief overview of the computational modeling and simulation techniques used in the present work. A broad description of the multiscale modeling approach is presented first, followed by a description of each of the different simulation techniques used to investigate the structural features and mechanical response at the different length scales investigated. This chapter is intended to only provide the background for the computational techniques; specific simulation details are discussed in more detail in later chapters.

2.1 Multiscale Modeling Approach

A multiscale modeling approach is employed in order to study structure-property-function relationships across multiple length and time scales. Figure 2-1 schematically demonstrates this approach by showing the relevant length and time scales accessible via a variety of simulation techniques. The primary advantage of utilizing a multiscale modeling approach is in the ability to link disparate length scales and understand the interplay between structural features at the atomistic and molecular scales and the mechanical response of mesoscale and larger structures. For example, subtle changes in the the amino acid sequence of a protein can have effects on its larger scale structure which in turn can affect the function and mechanical performance of the protein molecule and larger assemblies based on the protein. Understanding these

types of relationships is crucial for designing new materials and ultimately optimizing their performance for various applications. The work in this thesis will focus on non-reactive molecular dynamics and coarse-grained molecular dynamics (both described below), but even just these two techniques allow for the investigation of material properties and behaviors from sub-nanometer to micron length scales.

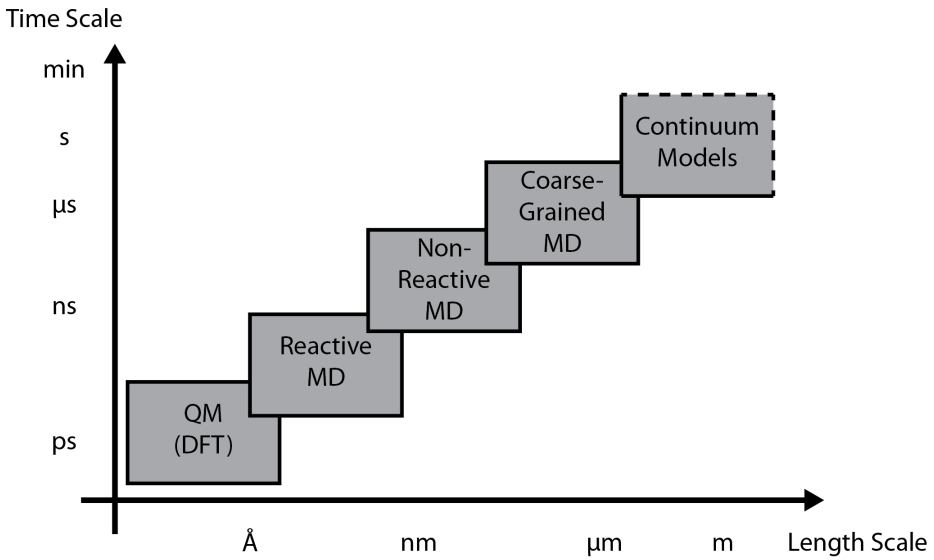

Figure 2-1: Multiscale Modeling Paradigm. Combining different simulation techniques allows for the study of the same materials across multiple lenght and time scales. Information learned at smaller length scales is used to build and paramterize larger scale models in which the important and relevant mechanisms and behaviors are represented appropriately. Figure adapted from [54]

2.2 Molecular Dynamics Simulations

The primary computational technique used in this thesis is Molecular Dynamics (MD) simulations. Although this technique originated with simple studies of small collections of noble gas atoms in the 1950s and 60s [55,56], the dramatic scaling of computational power and the development of sophisticated interatomic potentials has allowed MD to remain a relevant and immensely useful computational tool. The main idea behind MD is to solve Newton's laws of motion for a collection of particles which interact through a prescribed interaction potential, resulting in a trajectory for each

particle through time. At each point in time, the equation of motion for each atom or particle is solved:

$$F_i = m_i a_i \tag{2.1}$$

where F_i, m_i, and a_i are the force, mass and acceleration of the particle, allowing for the determination of the position and velocity of each particle at each time step, $r_i(t)$ and $v_i(t)$, respectively. The total energy of a collection of N particles is given by the sum of the kinetic and potential energies of all of the particles:

$$E = K + U \tag{2.2}$$

where the kinetic energy K is given by:

$$K = \frac{1}{2}\sum_{i=1}^{N} m_i v_i^2 \tag{2.3}$$

and the total potential energy depends on the position of the relative positions of each of the particles in the system:

$$U(r) = \sum_{i=1}^{N} U_i(r) \tag{2.4}$$

The equation of motion to be solved then becomes:

$$F_i = m_i a_i = m_i \frac{d^2 r_i}{dt^2} = -\nabla_{r_i} U(r_i) \quad i = 1...N \tag{2.5}$$

This equation is iteratively solved by updating the positions of the particles based on their old positions their current accelerations. With the Verlet Algroithm, this is expressed as:

$$r_i(t + \Delta t) = -r_i(t - \Delta t) + 2r_i(t) + a_i(t)(\Delta t)^2 + O((\Delta t)^4) \tag{2.6}$$

At each time step, the acceleration is calculated as:

$$a_i = \frac{F_i}{m_i} = \frac{-1}{m}\nabla_{r_i} U(r_i) \quad i = 1...N \tag{2.7}$$

Although the equations to be solved are quite simple on the surface, the difficulty comes in the definition of a good potential energy function $U(r)$, the so called force field. The force fields used for both atomistic scale molecular dynamics and coarse-grained molecular dynamics studies are discussed briefly below, and the specific simulation details including atomistic scale force field parameters and coarse-grain model parameterization techniques are discussed in more detail in later chapters.

2.2.1 Atomistic Scale Molecular Dynamics

Atomistic scale molecular dynamics, also known as all atom MD, involves performing MD simulations on a system that includes explicit representations of each atom, often (but not always) including any water molecules which may solvate the system. The challenge in performing reliable all-atom MD simulations is in choosing an appropriate force field (potential energy function) for a given system. The discussion here will focus on force fields for describing biological and polymeric materials, since those are the focus of this thesis. A few of the widely used classical force fields for describing these types of materials are the CHARMM force field [57], AMBER force field [58], DREIDING force field [59], UFF force field [60], GROMOS force field [61], and the OPLS force field [62, 63]. These force fields share a similar description of the interactions between atoms; in general the total system energy is defined as the sum of the bonded, angle, torsional, electrostatic, and van der Waals interactions:

$$U_{System} = U_{bond} + U_{angle} + U_{torsion} + U_{electrostatic} + U_{vdW} \tag{2.8}$$

These interactions are shown schematically in Figure 2-2. In some more modern force fields, additional terms are added which couple these basic interactions. These force fields are typically parameterized based on quantum mechanics (Density Functional

Theory) simulations and the resulting parameters are often tuned to better match experimental observables, including structure and mechanical and thermodynamic properties. This results in force fields with a large number of "atom types" to describe the changes in the interactions that atoms have in different chemical environments. Often, mixing rules are defined to describe the interactions between atom types which have not been explicitly parameterized. Furthermore, since water is often a major component of biological systems, these force fields also include specific interaction potentials for water molecules, most commonly the TIP3P, TIP4P, and SPC models [64].

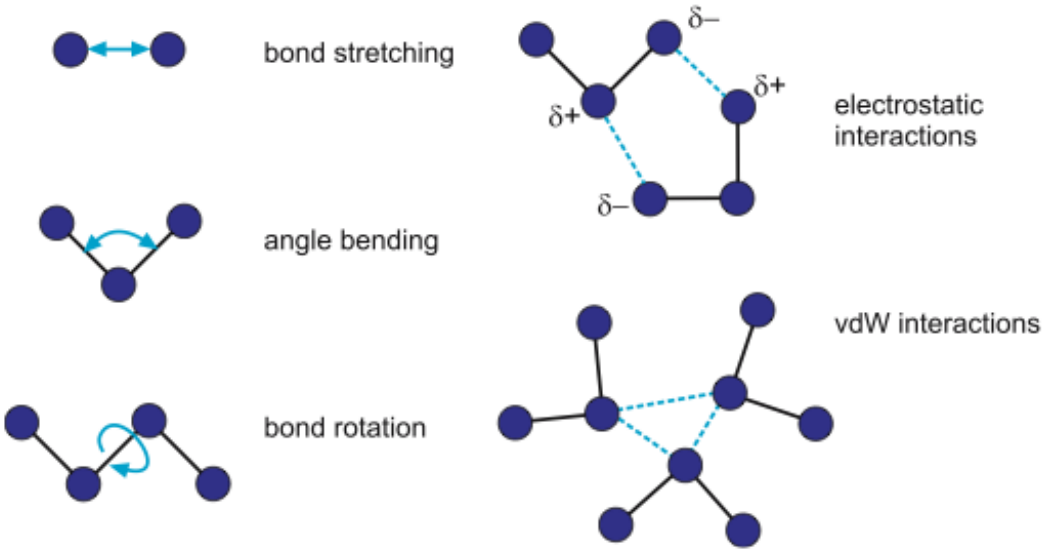

Figure 2-2: Schematic representation of the different interactions which make up a typical all atom force field. Figure reprinted with permission from [54].

In the present work, the CHARMM force field is used for all of the atomistic scale MD simulations as it has been successfully used to study the mechanical properties of amyloid and similar protein molecules [15, 16, 24, 25, 48, 65–68]. Mechanical characterization techniques in MD simulations are discussed below in Section 2.2.4.

2.2.2 Coarse-Grained Molecular Dynamics

Coarse-grained MD, in contrast to all atom MD, is a modeling technique in which groups of atoms are described by a single particle. The degree of "coarse-graining" ranges widely from united atom models in which hydrogen and carbon atoms are combined into a single "united atom" or the MARTINI force field in which whole amino acids are combined into one to two coarse-grained beads [69, 70], all the way to models with a much coarser description in which hundreds or thousands of atoms are coarse-grained into a single bead. The coarse-grained MD used in this thesis will follow the latter description as it is intended to describe larger scale structures rather than molecular scale features. Coarse-graining has two primary benefits in terms of computational cost reduction. Most obviously, since many atoms are described by a single particle, coarse-graining allows for the study of systems at scales which are beyond the computational capability of an all atom description, and thus allows MD simulations to be used to study structures into the micrometer and larger scales. Furthermore, the potential energy functions in coarse-grained descriptions are typically simpler than those used in all atom simulations, particularly in coarse-grained models which do not have explicit electrostatic interactions as these are typically some of the most computationally expensive calculations. These simpler potential energy functions further speed up coarse-grained simulations and allow for larger systems to be studied or longer time scales to be investigated.

Much as all atom force fields like those described above are often parameterized from smaller scale quantum mechanics based simulations, coarse-grained potentials are often parameterized from atomistic scale simulations using the aforementioned all atom force fields; this method is summarized in Figure 2-3. This is the so-called fine-trains-coarse approach, and it follows from the multiscale modeling approach described above in Section 2.1. By feeding the results of smaller scale simulations into coarser models, the relevant physics are preserved and the behavior of larger scale structures can be investigated. It is noted that it is often a good practice to validate these types of coarse grained models by comparing a property of interest, for example

the mechanical response, to experimental measurements when they are available.

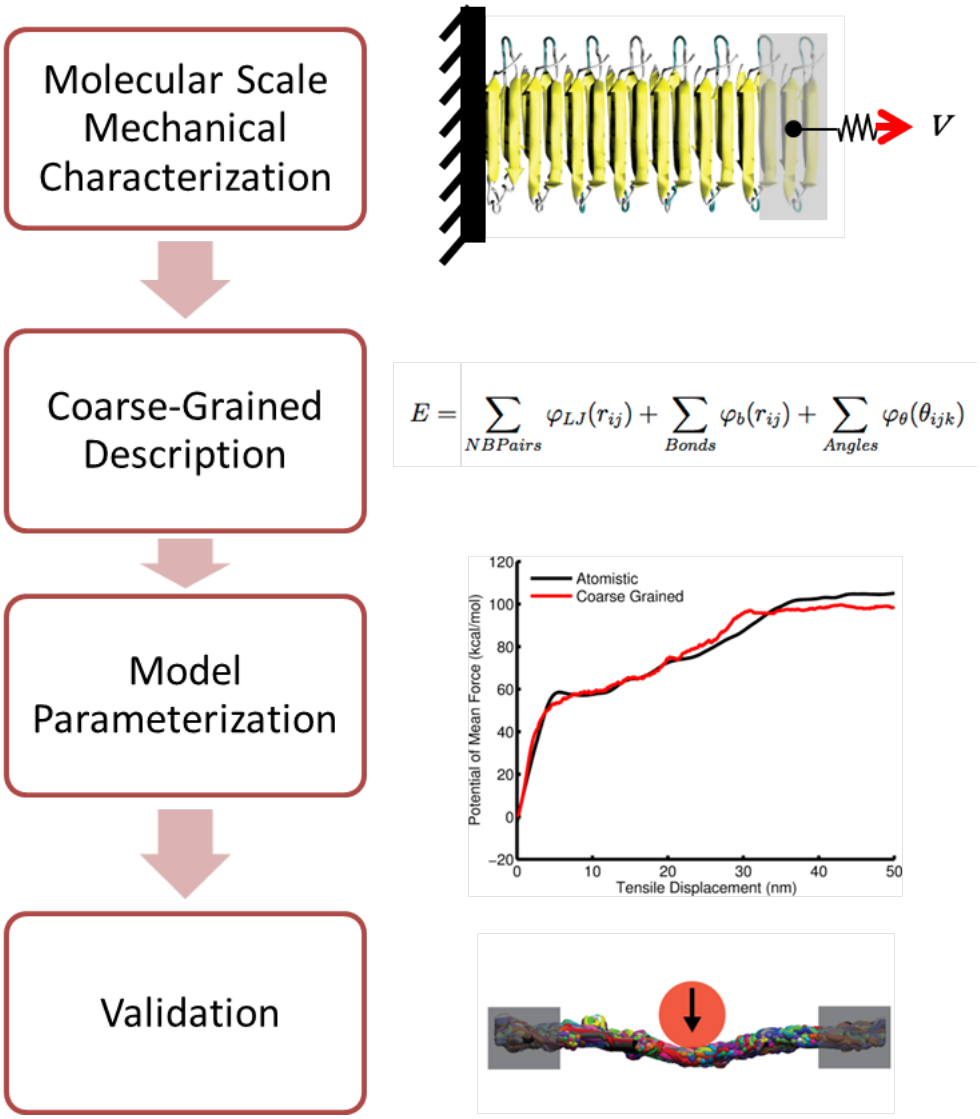

Figure 2-3: Schematic of the "fine-trains-coarse" approach for the parameterization of a coarse-grained model based off of atomistic scale simulation results.

2.2.3 Langevin Dynamics Simulations

Langevin Dynamics is a common extension to classical MD and is often a better description of the equations of motion for coarse-grained models as it includes the effects of an implicit solvent interacting with the coarse-grained particles. In Langevin

Dynamics, the standard equations of motion (Equation 2.5) are replaced by:

$$F_i = m_i a_i = -\nabla_{r_i} U(r_i) - \gamma m_i v_i + \sqrt{2 m_i \gamma k_B T} R(t) \quad i = 1...N \tag{2.9}$$

where the first term is the classic conservative force, the second term is a frictional term that is proportional to a given particle's velocity, and the third term is a random force which simulates an interaction with an implicit solvent [71]. The $R(t)$ term is a stationary Gaussian process with $\langle R(t) \rangle = 0$ and $\langle R(t) R(t') \rangle = \delta(t - t')$. The γ factor controls the frictional drag on the particles and is related to the size of the particles by:

$$\gamma = 3\pi\eta D \tag{2.10}$$

where η is the dynamic viscosity of the solvent (water) and D is the particle diameter.

2.2.4 Steered Molecular Dynamics

In order to characterize mechanical response of a system in an MD (or Langevin Dynamics) simulation, appropriate boundary conditions must be applied to induce deformation. One of the main methods used in this thesis to accomplish this Steered Molecular Dynamics (SMD). SMD is a non-equilibrium technique in which the system is "steered" along a prescribed reaction coordinate in order to investigate a particular response response. In an SMD simulation, a moving harmonic restraint (spring) is attached to the center of mass of an atom or group of atoms (the SMD group), effectively pulling on that group. This adds an additional term to the total energy of the system:

$$U_{SMD} = \frac{1}{2} K_{SMD} \left(vt - (\mathbf{r} - \mathbf{r}_0) \cdot \mathbf{n} \right)^2 \tag{2.11}$$

where K_{SMD} is the spring constant of the SMD spring, $\mathbf{r}$ and $\mathbf{r}_0$ are the position and original position of the group to which the SMD spring is attached, respectively, v is the pulling velocity, and $\mathbf{n}$ is the pulling direction [54]. This results in a force being

applied to the SMD group of:

$$F_{SMD} = K_{SMD}\left(vt - (\mathbf{r} - \mathbf{r}_0) \cdot \mathbf{n}\right) \tag{2.12}$$

This force can be monitored over the course of an SMD simulation to obtain the force-displacement response along the pulling direction. The SMD method is shown schematically in Figure 2-4 along with its similarity to an AFM pulling experiment in which the AFM tip is attached to a portion of a molecule and displaced while the force is recorded.

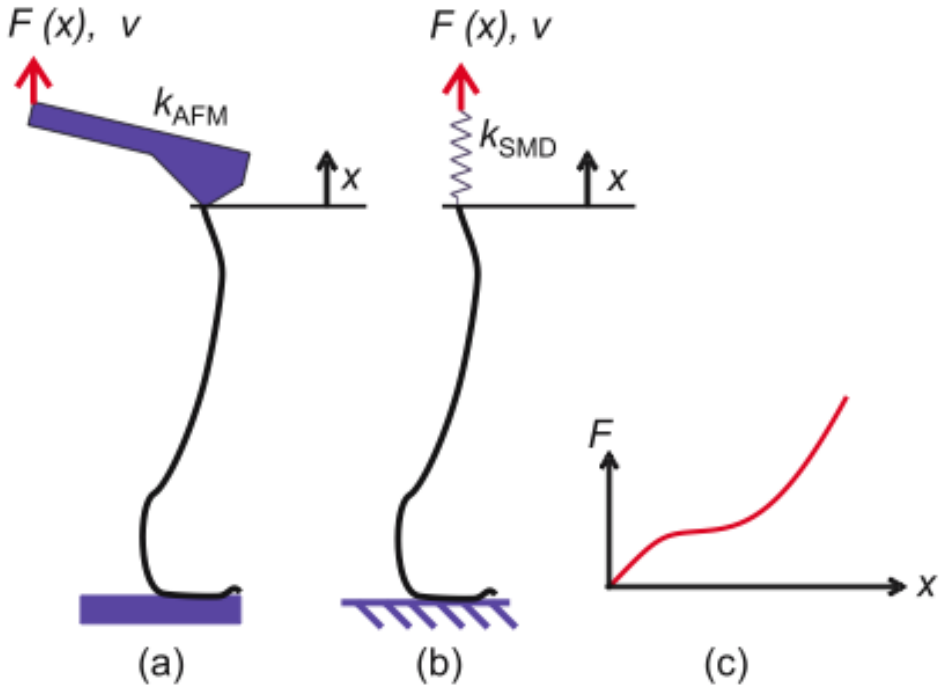

Figure 2-4: Schematic representation of (a) an AFM experiment and (b) an equivalent SMD simulation. The force-displacement response of a molecule can be measured by recording the force in the SMD spring (c). Figure reprinted with permission from [54].

2.3 Chapter Summary

This chapter presented a brief overview of the modeling and simulation methodology employed in this thesis. A multiscale approach is used to enable the development of a bottom up model of of amyloid and amyloid-like protein fibrils which can be used to study the mechanical response of structures at multiple length scales. At the atomistic or molecular scales, full atomistic MD simulations are used in which each atom, including water molecules, is explicitly represented and an all atom force field is used to describe their interactions (the CHARMM force field). To study larger length scales, a fine-trains-coarse approach is used to parametrize a coarse-grained description. Finally, steered molecular dynamics is a versatile tool for probing a variety of responses in MD simulations and it is one of the primary methods used in this thesis to investigate the mechanical response of systems in both full atomistic and coarse-grained simulations.

Chapter 3

Structure-Property Relationships at the Atomistic Scale

Understanding the behavior of amyloid and amyloid-like protein fibrils at the atomistic scale is crucial for building a foundation for understanding larger scale properties and behaviors, and ultimately for engineering *de novo* amyloid-based functional materials. One of the key challenges in understanding the structure-property relationships in these materials, however, lies in the diversity of the secondary structures exhibited by different amyloid and amyloid-like fibrils. This chapter focuses on exploring these structure-property relationships at the atomistic scale and developing simple guidelines for choosing or engineering optimal amyloid fibrils for use in functional amyloid-based biomaterials. Furthermore, the work in this chapter also lays the groundwork for the development and parameterization of a larger scale model of amyloid and amyloid-like fibrils; this work is described in Chapter 4.

3.1 Tensile Response

Perhaps the most notable and exciting property of amyloid and amyloid-like fibrils in the context of functional material design is the tensile response. Amyloid fibrils are among the strongest and stiffest purely proteinaceous materials known; previous experimental and computational work has found their Young's Moduli to be in the

range of 10-30 GPa and their strength in the 100s of MPa [21–24, 26, 68, 72]. As described above, these impressive mechanical properties originate from the cross-β secondary structure motif, but what is not clear is the relationship between the size, shape, and connectivity in these cross-β protein fibrils and their specific mechanical responses. In this section, the relationship between molecular geometry and the tensile and failure response in amyloid and amyloid-like fibrils is investigated; a qualitative and quantitative analysis of the deformation mechanisms and mechanical response is performed, and the role of hydrogen bond organization and rupture dynamics in determining the mechanical response is closely examined.

3.1.1 Model and Methods

Six different protein structures spanning three distinct secondary structure motifs are investigated by performing full atomistic molecular dynamics simulations: two fibrils comprising stacked β-sheets (Figure 3-1(a)), three β-helical fibrils (Figure 3-1(b)), and a mixed structure comprising stacked β-helical units (Figure 3-1(c)). All three motifs possess the cross-β structure characteristic of amyloid fibrils, yet they differ in the specific connectivity within the fibril as well as the size and shape of the structure. It is noted that these six structures do not span the entire range of possible amyloid or amyloid-like structures. However, they are representative for many commonly observed structural motifs and thus cover a broad range of structures.

The two stacked β-sheet structures considered are the Aβ (1-40) amyloid fibril [31, 72] and the Iowa Mutant Aβ amyloid fibril (Protein Data Bank (PDB) [73] code 2LNQ [74]) as shown in Figure 3-1(a)(i) and (a)(ii), respectively. The two structures have a rectangular cross-section but differ in the stacking of the β-sheets; the Aβ (1-40) fibril features parallel stacking while the Iowa Mutant fibril features antiparallel stacking. The three β-helical fibrils are the Yersinia Adhesin (YadA) collagen-binding domain (PDB code 1P9H [75]), the *Lolium perenne* ice-binding protein (PDB code 3ULT [76]) and the C-terminal domain of the GlmU enzyme from *E. coli* (PDB code 1FWY [77]) shown in Figure 3-1(b)(i), (b)(ii), and (b)(iii), respectively. The structure based on the GlmU enzyme is constructed by replicating residues 276-311 up the

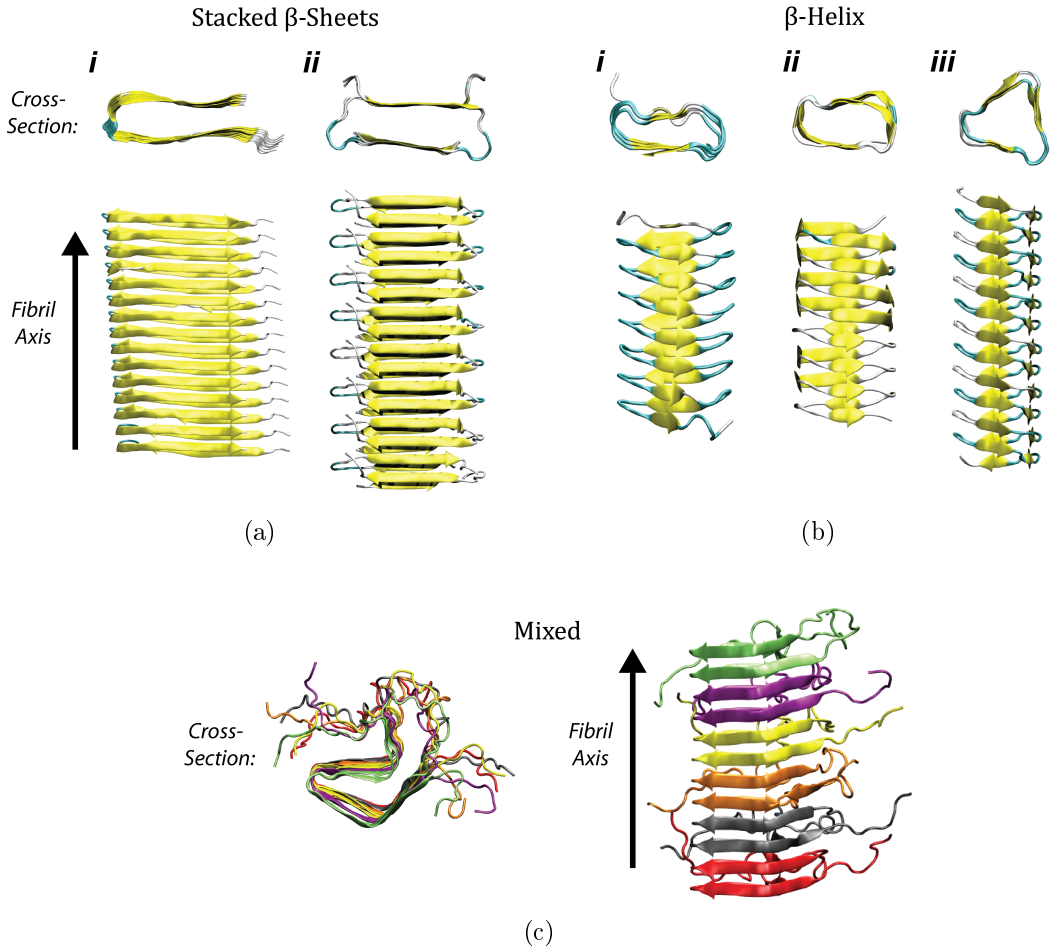

Figure 3-1: Amyloid and amyloid-like protein fibril structures considered. All of the structures posses the cross-β secondary structure motif but differ in their connectivity, size, and shape. (a) Stacked Structures: (i) the Aβ (1-40) amyloid fibril and (ii) the Iowa Mutant Aβ amyloid fibril. (b) β-helix structures: (i) the YadA collagen-binding domain, (ii) the *Lolium perenne* ice-binding protein and (iii) the C-terminal domain from the GlmU enzyme in *E. coli*. (c) A mixed structure from the HET-s amyloid fibril; color indicates separate β-helical subunits.

helix axis to form a continuous backbone [72]. The first two β-helical fibrils feature a rectangular cross-section while the third has a triangular cross-section; all three structures are left-handed β-helices. The mixed structure is the HET-s prion fibril (PDB code 2KJ3 [78]) as shown in Figure 3-1(c); it features a stacked arrangement of 2-layer β-helical units.

All structures are initially prepared with the Visual Molecular Dynamics package (VMD) [79] and all simulations are performed with GROMACS version 4.6.2 [80–83] and the CHARMM27 force field [57]. The simulations are performed on a multicore workstation with an NVIDIA Tesla K20 to enable GPU acceleration. A 1.4 nm cutoff is used for short-range interactions, and the particle mesh Ewald algorithm [84, 85] is used to calculate long-range electrostatic interactions. Each protein structure is placed in a periodic box with explicit TIP3P water molecules and 0.1 M NaCl. Energy minimization is performed followed by a three step equilibration procedure. NVT simulation is performed for 50 ps at 300K followed by NPT simulation for 100 ps at 300K and 1 bar; during these first two steps, the positions of the heavy atoms are restrained. The final equilibration step is 5000 ps of NPT simulation at 300K and 1 bar without position restraints. In all simulations, temperature and pressure are controlled by the Nosè-Hoover thermostat [86, 87] and a Parrinello-Rahman barostat [88, 89], respectively, and the LINCS algorithm [90, 91] is used to constrain bond lengths and thus enable a 2.0 femtosecond time step.

Tensile deformation is accomplished by performing steered molecular dynamics (SMD) simulations; SMD has been shown to be an effective method for probing the mechanical response of protein molecules *in silico* [92]. The bottom layer of each structure is held fixed; a spring with a spring constant of 5000 kJ mol^{-1} nm^{-2} is attached to the center of mass of the top three layers of each structure and is pulled upward along the fibril axis at a constant velocity of 5×10^{-5} nm ps^{-1} for a total of 100 nanoseconds in each case. The force in the spring is recorded as a function of the displacement in the protein in order to obtain a stress-strain curve for each structure. This SMD setup is similar to atomic force microscopy (AFM) experiments which have been successfully used to probe the mechanical properties of small protein

molecules including amyloid fibrils [5, 19, 21, 92]. In order to account for stochastic effects, a total of three SMD runs are performed for each structure and the results are averaged; an additional 500 ps equilibration is performed on each structure prior to the SMD run in order to sample a new configuration.

3.1.2 Results and Discussion

Mechanical Response

Representative stress-strain responses for the six protein structures investigated are shown in Figure 3-2(a). The stress-strain curves are obtained from force-displacement results from the SMD pulling simulations. The appropriate initial lengths and cross-sectional areas are measured from the equilibrated structures using molecular visualization, and are summarized in Table 3.1. It is interesting to note the similarities in the stress-strain response across the six structures; despite the diversity of the geometries, they each exhibit a large initial peak in the stress at low strains, followed by an extended region of deformation at very low stresses. The stacked structures (Figure 3-2(a)(i)) reach the lowest stress values and also exhibit the most brittle behavior with a relatively smaller UTS and narrower initial peaks, indicating that only a small amount of energy can be dissipated through tensile deformation in these structures. In contrast, the helical structures (Figure 3-2(a)(ii)) and especially the mixed structure (Figure 3-2(a)(iii)) are more robust as indicated by the higher peak stresses and wider initial peaks.

Table 3.1: Summary of the geometric parameters used and the mechanical properties extracted from this study. The values for Young's Modulus and ultimate tensile strength (UTS) are the average from three simulations for each structure.

Structure		Initial Length (nm)	Cross-Sectional Area (nm^2)	Young's Modulus (GPa)	Ultimate Tensile Strength (MPa)
Stacked	Aβ (1-40)	7.85	5.46	13.0	242.6
	Iowa Mutant Aβ	6.96	3.64	11.7	402.3
Helical	YadA CBP	3.52	1.40	12.6	553.7
	LpIBP	3.74	1.89	26.9	693.4
	GlmU C-Terminus	5.37	2.20	23.3	629.8
Mixed	HET-s Prion	5.38	2.10	9.8	917.0

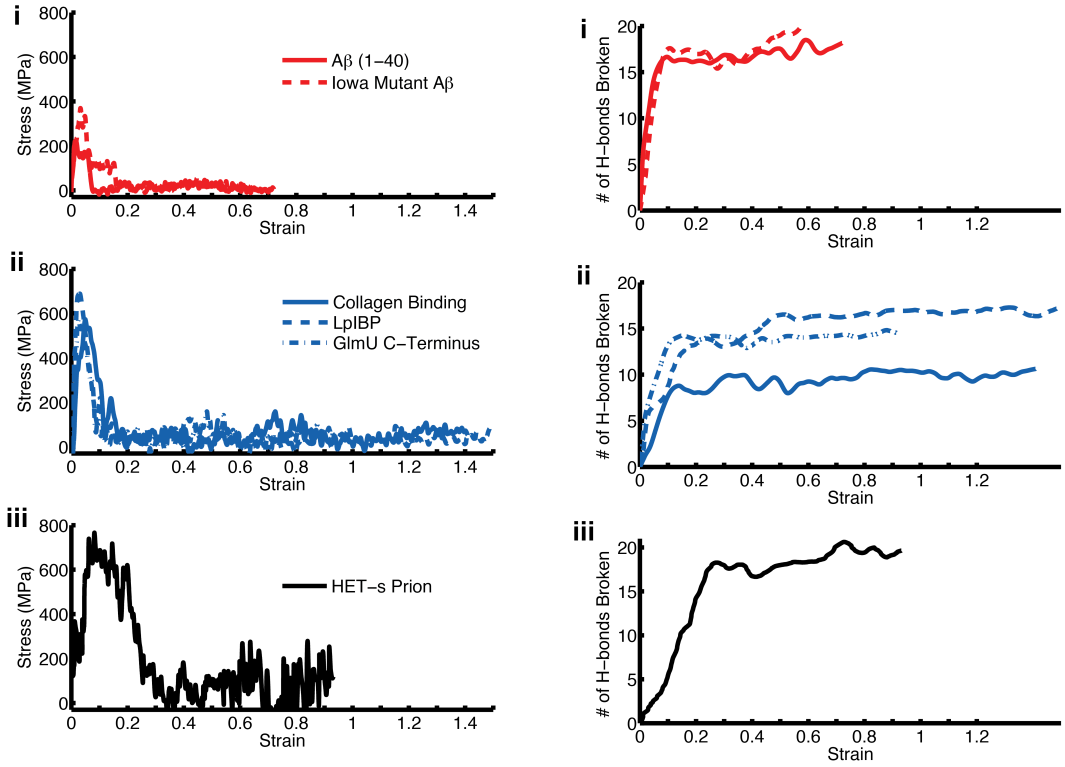

(a) (b)

Figure 3-2: Stress vs. Strain and Hyrdogen Bond Breaking vs. Strain. (a) Representative stress-strain curves for (i) stacked structures, (ii) helical structures, and (iii) mixed structure. It is notable that the mechanical response across the three structures is quite similar; in each case there is an initial high stress regime followed by an extended low stress regime as the strain is further increased. For both the stacked and helical structures, the initial peak in stress occurs within approximately 10% strain; for the mixed structure, the peak is broader, extending to approximately 30% strain. (b) Number of hydrogen bonds broken in the failure process for (i) stacked structures, (ii) helical structures, and (iii) mixed structure. All of the curves exhibit an initial high slope regime at low strains corresponding to rapid rupture of hydrogen bonds followed by a slow rupture regime at higher strains. The rapid rupture process occurs in the same strain regime as the peak in the stress-strain curves indicating the importance of hydrogen bond rupture in determining the mechanical response.

The number of hydrogen bonds broken as a function of the tensile strain is shown in Figure 3-2(b). Hydrogen bond analysis is performed in VMD with distance and angle cutoffs of 0.35 nm and 30 degrees, respectively; only hydrogen bonds in the regions which undergo permanent deformation are considered to isolate effects of hydrogen bond rupture on the mechanical response. For each structure, two distinct regimes are found for the hydrogen bond rupture dynamics: a fast rupture regime at low strains and a slow rupture regime at higher strains. In the stacked and helical structures, fast hydrogen bond rupture occurs within 10-15% strain, while in the mixed structure, the fast rupture process takes place over approximately 25% strain. In all of the structures, this fast hydrogen bond rupture process corresponds with the peak in the stress-strain curve, indicating that the fast rupture of hydrogen bonds is a key mechanism which determines the mechanical performance of these cross-β protein structures. In contrast, the slow hydrogen bond rupture process which occurs at larger strains requires very little stress. These results agree well with a previous study which found that the instantaneous strength of a small β-helical nanotube depends on the rate of hydrogen bond rupture, with faster rupture resulting in higher strengths [67]; the present work demonstrates that this relationship persists across a variety of secondary structural motifs in protein filaments.

The Young's Moduli and ultimate tensile strength (UTS) are found from the small-strain regime and are averaged over the three SMD runs; the results are shown in Figure 3-3 and listed in Table 3.1. The results agree well with previous computational and experimental reports on similar β-sheet structures which find the elastic modulus in the range of 10-30 GPa and the strength on the order of 100 MPa [5, 21, 53, 66, 93]. We note that atomistic results for strength and elastic modulus can be sensitive to the cross-sectional area used in their calculation and thus the shaded regions in the "Ashby-like" plot in Figure 3-3 qualitatively illustrate the broad range of properties accessible with these types of protein fibrils. In general, the stacked structures exhibit lower moduli and UTS while the helical structures tend to be more stiff and robust with higher moduli and UTS; the mixed structure exhibits a combination of these properties with a large UTS and a low elastic modulus. These results indicate the

emergence of an interesting pattern in the mechanical properties of these types of cross-β protein fibrils, and could provide a basis for choosing or designing protein fibrils with specific mechanical properties for functional materials; however, more work is required to see if this pattern holds across many more protein structures.

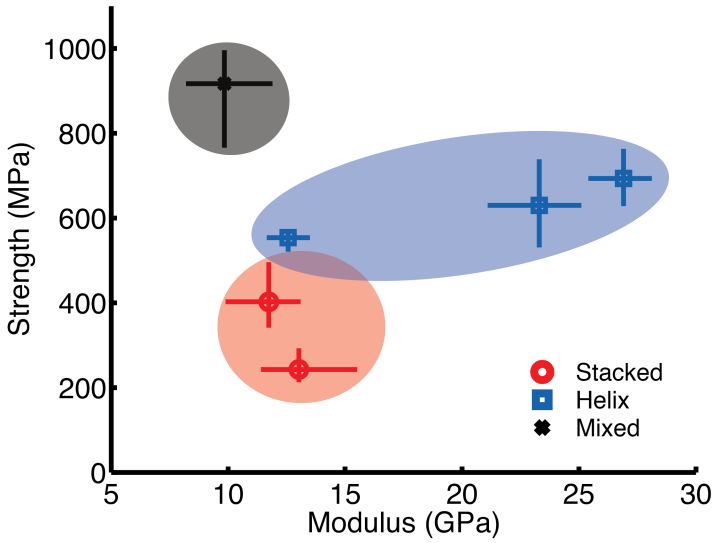

Figure 3-3: Ashby-like plot to summarize the tensile strength over the moduls for the six structures considered; the best performers can be identified in the top right corner of the plot. The shaded regions qualitatively illustrate the broad range of properties accessible with these different structures, and the error bars indicate the minimum and maximum calues observed for each structure.

Deformation and Failure Pathways

In order to better understand the origins of the stress-strain responses, the deformation and failure pathways in the different protein structures are examined. Figure 3-4 shows snapshots from the SMD simulations for the three structural motifs. In the Aβ(1-40) structure (Figure 3-4(a)(i)), the hydrogen bonds between two β-strands on one side of the fibril break, and a two-strand segment is left which slowly peels off with additional tensile deformation. The Iowa mutant fibril (Figure 3-4(a)(ii))deforms very similarly, except that the initial fast rupture event involves two groups of hydrogen bonds as shown in Figure 3-5(a). The helical structures exhibit the same two step deformation pathway with the initial fast rupture process involving rupture of the

hydrogen bonds making up approximately a full turn of the β-helix as shown in Figure 3-5(b) followed by a slow unwinding of the helical structure. In the YadA collagen binding protein (Figure 3-4(b)(i)) and the ice binding protein (not shown), the initial rupture involves breaking the hydrogen bonds between two sets β-strands due to the rectangular cross-sectional shape of these proteins; in contrast, the GlmU C-terminal β-helix (Figure 3-4(a)(ii)) has a triangular and thus hydrogen bonds between three sets of β-strands are broken during the initial rupture process. Interestingly, the rupture in the mixed structure HET-s fibril (Figure 3-4(c)) occurs within one of the β-helical units, rather than between them. As with the GlmU C-terminal β-helix, the triangular cross-section of the HET-s structure results in the disruption of three sets of β-strands during the initial rupture event.

These deformation pathways, along with the analysis of the hydrogen bond rupture dynamics, clearly demonstrate the importance of cooperative deformation and rupture of hydrogen bonds for determining the mechanical response of these amyloid and amyloid like protein fibrils. All of the useful mechanical properties originate from the fast rupture of hydrogen bonds which occurs cooperatively in specific groups of hydrogen bonds between β-strands along the fibril axis, rather than in random positions along the fibrils.

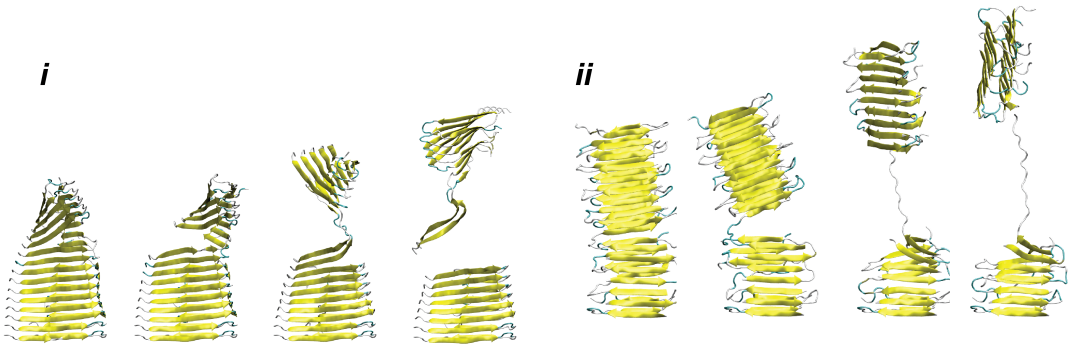

(a)

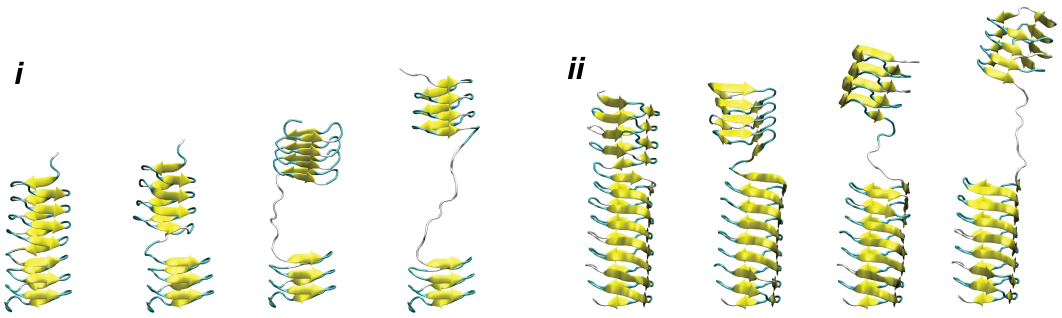

(b)

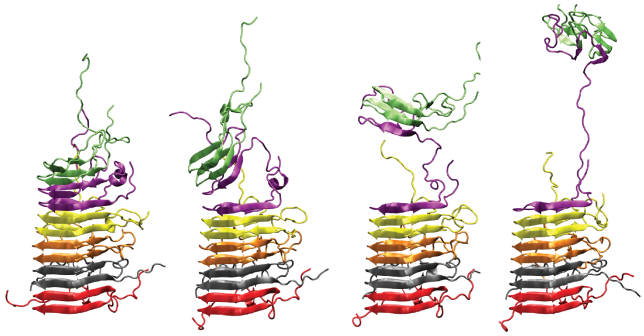

(c)

Figure 3-4: Deformation and faiulre pathways for (a) stacked structures, (b) helical structures and (c) the mixed structure. In each case there is an initial rupture event in which a large group of hydrogen bonds experience simultaneous rupture followed by an extended unforlding or unpeeling process as additional hydrogen bonds rupture one-by-one.

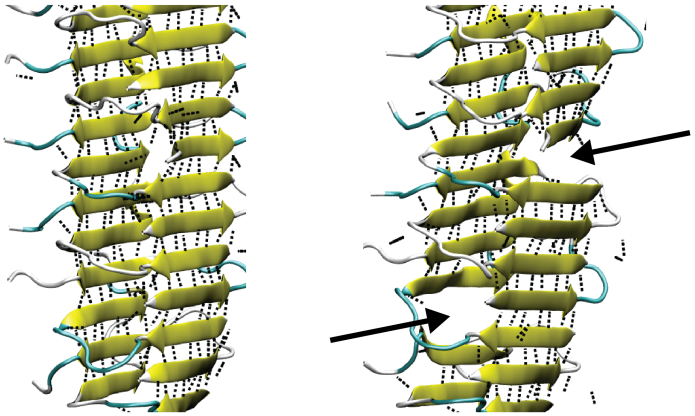

(a)

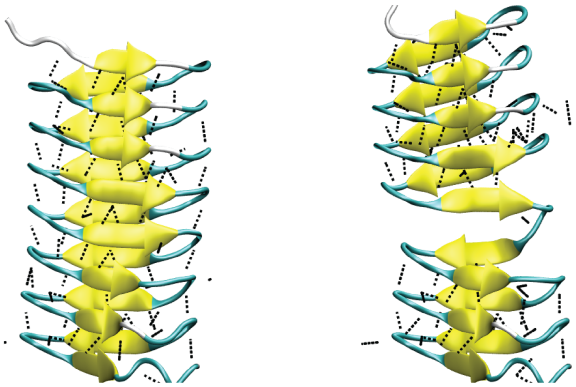

(b)

Figure 3-5: Simultaneous hydrogen bond rupture in (a) the Iowa Mutant Aβ stacked structure and (b) the YadA collagen-binding domain β-helix. The Iowa Mutant structure achieves a relatively large ultimate tensile strength due to the fact that the initial rupture event involves breaking hydrogen bonds at two locations as indicated by the arrows. In the β-helical structure, the hydrogen bonds in approximately one full turn of the helix rupture concurrently

The relationship between the peaks in the stress-strain curves and this cooperative hydrogen bond rupture provides an interesting opportunity to understand the specific effect of the cooperative rupture of hydrogen bonds in determining the tensile strength of these cross-β protein fibrils. Previous studies have demonstrated that in β-sheet nanocrystals, geometric confinement effects control the rupture strength of hydrogen bond assemblies loaded in shear [15, 16, 66, 94]. Figure 3-6 shows the relationship between the UTS and the number of hydrogen bonds per unit area broken

during the initial rupture event; the number of hydrogen bonds broken is found from the plots shown in Figure 3-2(b). We find that the UTS increases linearly as the areal density of broken hydrogen bonds increases. Each additional hydrogen bond per square nanometer of cross-sectional area results in an increase in the UTS of approximately 100 MPa, indicating that each hydrogen bond adds an additional 100 pN to the rupture force of the fibril.

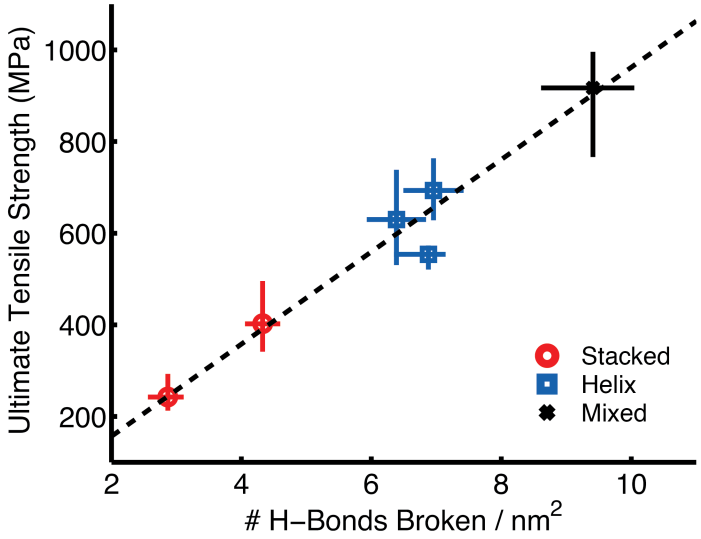

Figure 3-6: Variation in the ultimate tensile strength with the number of hydrogen bonds which break per unit cross-sectional area in the initial rupture event; the eror bars indicate he minimum and maximum values observed. A linear realationship is found which indicates that each additional hydrogen bond in the cross-section which ruptures results in a 100 MPa increase in the ultimate tensile strength, or an effective increase of 100 pN in the rupture force.

This understanding of the relationship between hydrogen bond organization and mechanical properties is quite significant in that it elucidates a clear design principle for creating high strength protein filaments: maximize the areal hydrogen bond density in the cross-section of the protein fibrils. It is also very interesting that the two structures which have a triangular cross-section (the GlmU β-helix and the HET-s mixed structure) exhibit the highest UTS. It has recently been suggested that a triangular core is a universal design pattern which is able to create stiff biological nanostructures [95]; our results extend this result and show that a triangular geometry might be a good design pattern for achieving high strengths in protein filaments.

The triangular geometry generally allows for a high areal density of hydrogen bonds which deform and break cooperatively, giving rise to a higher UTS.

Finally, the cumulative work performed during the tensile test can provide an interesting comparison of the relative energy scales involved in the tensile deformation of the different structures considered in this study. The work is calculated from the Potential of Mean Force (PMF), which is defined as the cumulative sum of the force times the displacement. Figure 3-7 shows the PMFs for the tensile tests of the six different structures. Again, these PMF curves illustrate the change in deformation mechanism as the curves shift from a high slope to low slope; in the context of the PMF, this corresponds with the fast accumulation of work as the structures reach peak stresses at low strains compared to the slow accumulation of additional work as the structures continue to unfold at low stresses. Interestingly, with the exception of the mixed structure, the total work performed in the tensile tests is quite similar, even though the structures feature very different geometries, however since this energy scale is an extensive, direct comparisons cannot be made as in the stress-strain response.

3.1.3 Conclusions

This section described an atomistic scale investigation into the tensile response of amyloid and amyloid-like fibrils featuring three distinct structural motifs. This work revealed two important features of the mechanical response of these protein fibrils: the *deformation* mechanisms by which these protein fibrils accommodate tensile deformation are largely *independent* of the geometry of the fibrils, and conversely, that the *strength* of the fibrils *is dependendent* on the fibril geometry. Regardless of the geometry, the structures exhibited a similar deformation pathway; for small deformations, the hydrogen bonds in the fibrils work cooperatively to provide the characteristic high strength, and as the deformation is increased, multiple hydrogen bonds rupture in rapid succession as the ultimate tensile strength is reached. The deformation process then shifts to one in which the remaining hydrogen bonds break one-by-one and provide very little additional tensile strength, much like a crack propagating through a brittle material. In contrast, the specific strength of the amyloid fibrils is quite sen-

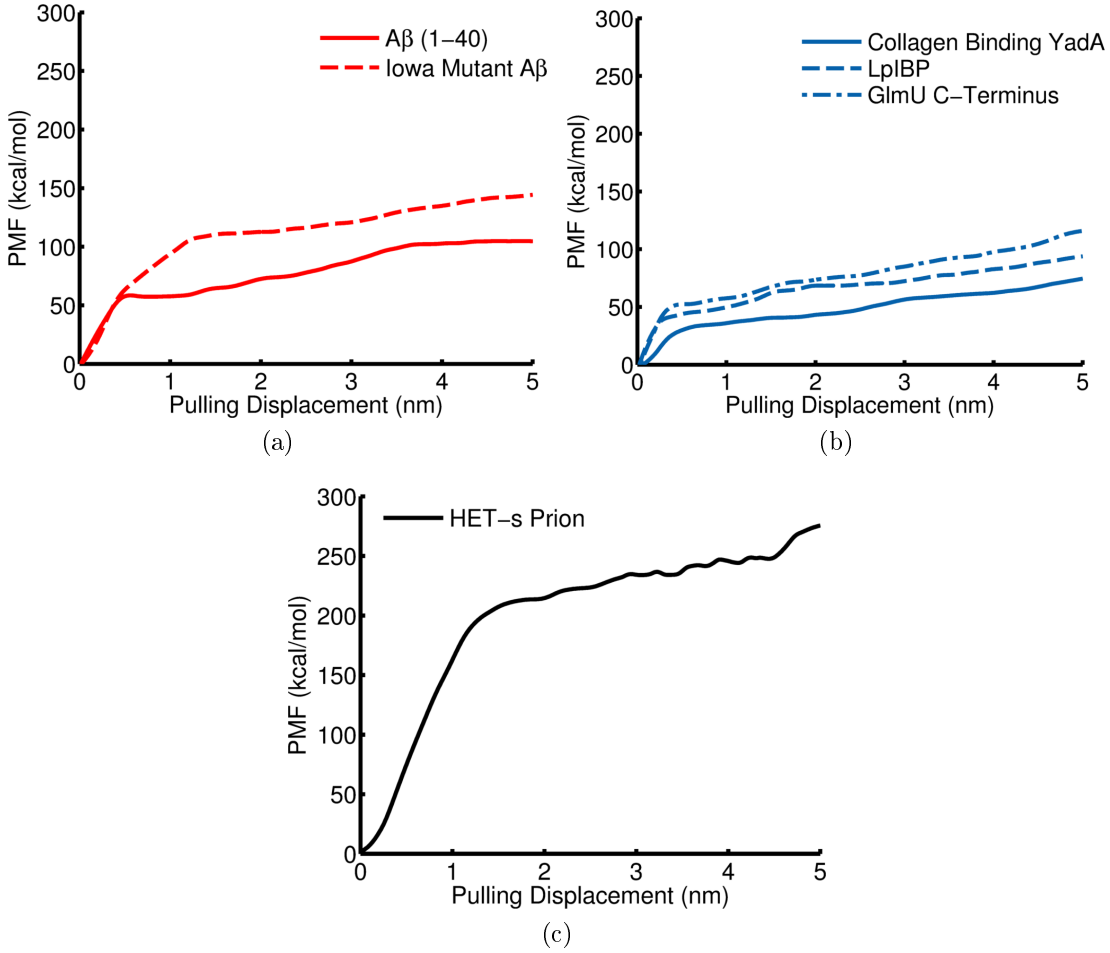

Figure 3-7: Potential of Mean Force curves fromt the tensile test simulations for (a) the stacked structures, (b) the helical structures, and (c) the mixed structure. The final (maximum) value of the PMF curve gives a measure of the total work performed in deforming the structures during the tensile tests.

sitive to the specific structure of the fibrils. Geometries which accommodate a higher density of hydrogen bonds into the fibril cross-section are generally able to achieve a higher strength since they allow for more hydrogen bonds to work cooperatively in the small strain regime and enhance the mechanical response.

The results from this work demonstrate that the specific amino acid sequence in these amyloid and amyloid-like fibrils is relatively unimportant compared to the organization and areal density of hydrogen bonds in the cross-β structure. Thus, the complex problem of choosing an optimal amyloid protein for use in an engineered functional role out of hundreds or thousands of potential proteins is reduced to identifying structures which maximize the hydrogen bond density in the fibril cross-section. This work provides some basic but important insights into the structure-property relationships in amyloids and provides the foundation for a consistent framework for choosing amyloid and amyloid-like fibrils for the design of novel functional biomaterials.

3.2 Bending Response

In addition to their impressive tensile properties, amyloid and amyloid-like protein fibrils are also notable for their high bending rigidity [21]. As with the tensile response discussed above in Section 3.1, the relationship between the secondary structure type, the size of the structure, and the resulting mechanical properties of various protein filaments and fibrils has not been extensively investigated. This section explores the nanomechanics of filamentous proteins under lateral loading conditions to identify key mechanical properties including the bending rigidity. Since the main structural feature of amyloid and amyloid-like fibrils is the cross-β secondary structure which only comprises hydrogen bonds along the fibril axis, the contribution of shear effects in the bending response is also investigated. Hydrogen bonded interfaces may not provide significant resistance to shear deformation, and the effects and importance of this deformation pathway have not been studied significantly. As was done with the tensile testing study (Section 3.1), multiple protein structures are investigated which have unique defining geometric characteristics.

3.2.1 Model and Methods

Molecular Models

Two widely found β-sheet rich protein structures are considered in this study which both feature the cross-β motif characteristic of amyloid and amyloid-like fibrils: an amyloid protein fibril comprising individual layers stacked upon each other and held together by hydrogen bonds between the β-sheets, and a β-helix structure which has a continuous covalently bonded backbone in addition to β-sheets parallel to the helix axis. The stacked structures are the two-fold symmetric Aβ (1-40) amyloid fibril, and are built according to [31] with lengths ranging from 1.92 to 9.58 nm. Figure 3-8(a) shows a 3.83 nm Aβ fibril. Parallel left-handed β-helix structures are built with coordinates obtained from the Protein Data Bank (identification code 1FWY) [73,77]. Residues 276-311 are copied and translate up the helix axis to form a continuous backbone as shown in Figure 3-8(b). Structures ranging from 6 to 20 turns are investigated, corresponding to lengths of 3.73 to 10.72 nm. Additionally, an alpha helix structure is considered as a comparison to the two β-sheet rich structures; the structure is shown in Figure 3-8(c). Initial coordinates are taken from the Protein Data bank (identification code 1GK6) [73,96], and a segment comprising ten residues (2.3 nm) is taken for this study. The choice of ten residues is motivated by recent work which suggests that alpha helices of this length are most stable to self-unfolding or formation of tertiary structures [97].

For all structures, the protein structure and coordinate files are created using tools in VMD [79] and NAMD [98] with CHARMM topology and force-field parameter files [57]. All simulations are performed with periodic boundary conditions in explicit water boxes with system sizes ranging from approximately 6,000 to 100,000 atoms. All structures are minimized and equilibrated with a NPT (isothermal-isobaric) ensemble set to a temperature of 300 K and a pressure of 1 atm. A time step of 1 femtosecond is used for each simulation, with a total simulation time ranging from 1.5 to 3 ns; the simulations are stopped when the structure reaches a stable configuration. The stability of all structures is verified from root-mean-square deviation (RMSD) data

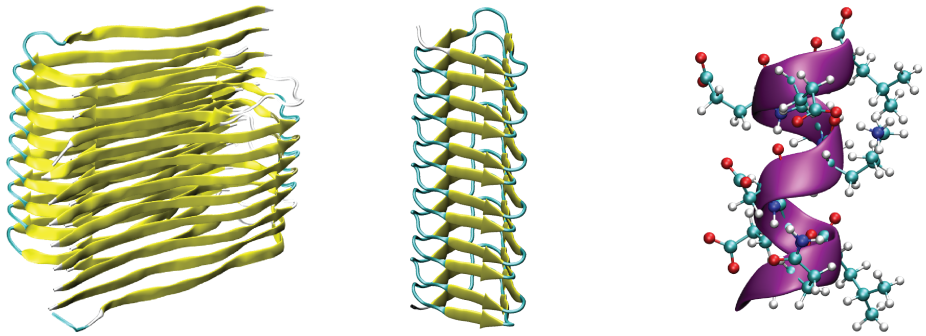

(a) (b) (c)

Figure 3-8: Protein structures considered for the bending study. (a), (b), and (c) show representative structures for the Aβ (1-40) amyloid fibril, the β-helical nanotube, and the alpha helix, respectively.

from the molecular dynamics trajectory; all structures are considered equilibrated once the RMSD has plateaued for at least 0.5 ns.

Loading Conditions

All three structures are subjected to loading conditions similar to those of a cantilever beam under constant tip loading as shown in Figure 3-9. For the Aβ (1-40) fibrils, the motion of the C_α atoms in the bottom layer are constrained and a constant force is applied to four C_α atoms in the top layer as illustrated in Figure 3-9(a). For the β-helix and alpha helix structures, the C_α atoms in the bottom turn of the helix are held fixed and a constant force is applied to one C_α atom in the top turn as shown in Figures 3-9(b) and 3-9(c). The choice of C_α atoms for the application of the loading boundary conditions is based on the goal of probing the mechanical response of the overall protein structure. Since the C_α atoms comprise the protein backbone, applying the forces to these atoms allows for some degree of consistency across the different structures considered, and it also prevents any effects that could arise from restricting the motion of side-chain groups.

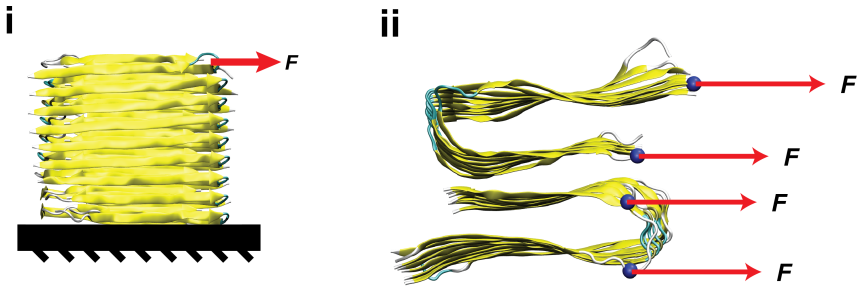

(a)

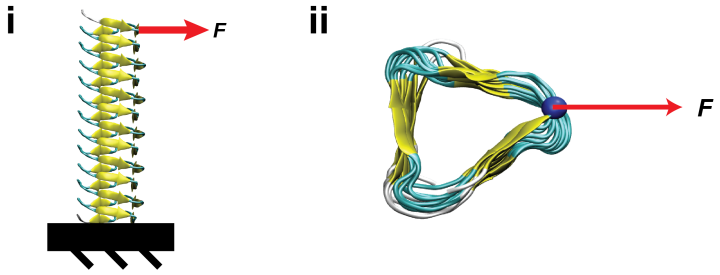

(b)

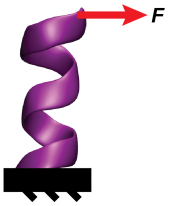

(c)

Figure 3-9: Tip loading boundary conditions used for the bending study. The atoms highlighted in blue in (a)(ii) and (b)(ii) are those to which the force is applied. For the alpha helix structure shown in (c), the force is applied to the terminal C_α atom.

For each structure, an appropriate force is chosen in order to generate adequate bending deformation while not resulting in failure. The forces applied range from 20 pN for the alpha helix up to 400 pN for the shortest (and stiffest) Aβ structure. These force levels are on the same order of magnitude as those applied in AFM protein unfolding experiments [27]. The tip displacement and bending profile measurements are performed once the structure has equilibrated under the applied load; equilibration is verified from root-mean-square deviation data. To reduce the effects of thermal fluctuations, atom positions are averaged over the final 100 simulation steps when

calculating tip displacements and bending profiles.

Continuum Theory and Bending Analysis

Analysis similar to that reported in [16] is performed here, incorporating shear deformation effects in an extended beam model [99] to describe the behavior of the different protein structures considered. In this model, the displacement of the tip is given by:

$$\delta_{tip} = \frac{PL}{D_t} + \frac{PL^3}{3D_b} \tag{3.1}$$

where P is the applied load, $D_b = EI$ is the bending rigidity, and $D_t = GA$ is the shear rigidity. The effective bending stiffness is given by:

$$k_{eff} = \frac{P}{\delta_{tip}} = \left(\frac{L}{D_t} + \frac{L^3}{3D_b} \right)^{-1}. \tag{3.2}$$

For comparison, an analysis based on classical beam theory without any shear effects (pure bending) is also performed. For this model, the tip displacement is given by:

$$\delta^*_{tip} = \frac{PL^3}{3D_b} \tag{3.3}$$

and the effective bending stiffness is given by:

$$k^*_{eff} = \frac{P}{\delta^*_{tip}} = \frac{3D_b}{L^3}. \tag{3.4}$$

The ratio of the two terms in equation 3.1:

$$s = \frac{3D_b}{L^2 D_t} \tag{3.5}$$

is effectively a shear contribution factor and gives a quantification of the importance of shear effects in the overall bending deformation; when s is less than one, pure bending cannot adequately describe the behavior, but when s is greater than one, pure bending theory should suffice. The length for which s is equal to one gives an approximation of the critical length at which this transition occurs.

The effective stiffnesses from tip displacement for both the extended beam model (equation 3.2) and the pure bending model (equation 3.4 are used to estimate material properties of the three protein structures, including the Young's Modulus, Shear Modulus, and persistence length ($\xi = EI/k_BT$) [100]. Values of D_b and D_t are obtained for each structure by fitting plots of the effective bending stiffness vs. fibril length. A simple geometric analysis of the atomic coordinates is used to calculate I and A for each structure; the calculated value for the Aβ structure agrees well with previous experimental findings [21], but experimental values for the other structures are not available in the literature and thus the geometric analysis alone is used. Bending profiles are calculated from:

$$\delta(y) = \frac{Py}{D_t} + \frac{P}{D_b}\left(\frac{Ly^2}{2} - \frac{y^3}{6}\right), 0 \leq y \leq L. \tag{3.6}$$

As is done in [16], the values of D_b and D_t are further refined from the original fit for each bending profile, but they are kept within the 95% confidence interval of the original fit from the tip displacement data.

Finally, fluctuations in the bending response are analyzed by recording the value of the tip displacement over the final 100 simulation steps. Gaussian curves are fit to the data in order to provide a quantitative measure of the magnitude of the tip fluctuations in each of the three structures.

3.2.2 Results and Discussion

Figure 3-10 shows a plot of the effective bending stiffness as a function of length for both the Aβ (1-40) amyloid fibrils and the β-helix structure. The simulation results are plotted along with curves showing predictions from both the extended beam model and the pure bending model. It is evident from Figure 3-10(a) that for the amyloid structure, shear effects must be included to accurately describe the bending behavior, and they are most important for shorter fibrils. For the smallest fibril considered in this study, shear accounts for approximately 60% of the total deformation as determined from the shear contribution factor. From the values of

D_b and D_t calculated from the fit, the critical length at which shear deformation is predominant in the amyloid structure is approximately 2.3 nm (about 6-7 layers). Shear deformation has been shown to be important for describing the mechanical behavior in many other hierarchically organized structures. Materials such as bone, microtubules and collagen all feature shear dependent deformation at different length scales; in particular, β-sheet nanocrystals in silk feature a structure similar to the amyloid, and exhibit similar shear dominated deformation for small lengths [16, 20, 101, 102].

In contrast, shear effects in the β-helix structure are rather unimportant. As seen in Figure 3-10(b), the curves for both bending models are virtually indistinguishable; pure bending describes the behavior of the β-helix very well. Furthermore, shear effects would not become important until the length of the β-helix structure is reduced to a value less than the length of a single turn ($L \approx 0.6$ nm). The stark difference in bending behavior between the two β-sheet rich structures is explained by the differences in their structural organization. The amyloid structure comprises individual layers that are held together only by weak hydrogen bonds, and thus the layers are easily sheared. The β-helix structure, however, has a continuous, covalently bonded backbone, which provides an additional degree of resistance to shear deformation.

Figures 3-11(a) and 3-11(b) show a series of simulation snapshots of the deformation profiles of the different sizes of amyloid fibrils and β-helices considered in this study. A simple visual comparison of the bending behavior of the two structures illustrates the difference between shear-dominated deformation in the Aβ (1-40) fibrils and pure bending in the β-helices, especially for shorter lengths. The shear deformation in the amyloid structure is evidenced by the linear shape of the deformed structures; even a small amount of sliding of individual β-sheets in the direction of the applied load (in the direction of the applied load) allows the structure to accommodate the load without significant stretching of the hydrogen bonds along the fibril axis. As the length of the amyloid is increased, however, the local strain induced by the tip load becomes smaller and the energy penalty for bending diminishes to the point at which the structure no longer exhibits a significant amount of shear deformation (and

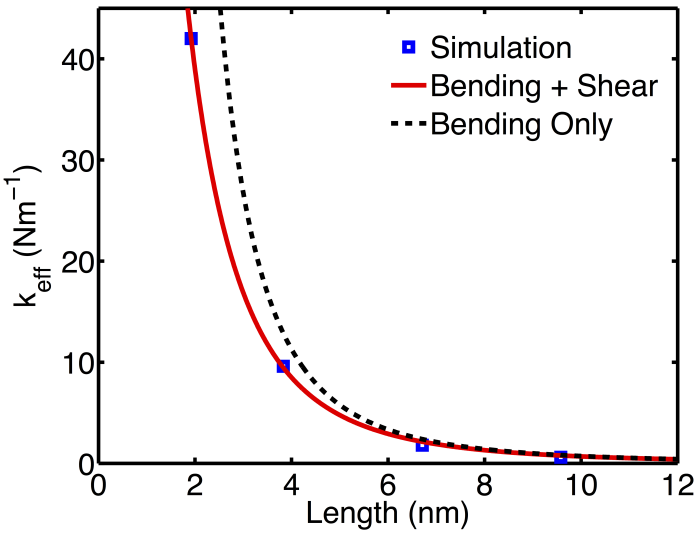

(a)

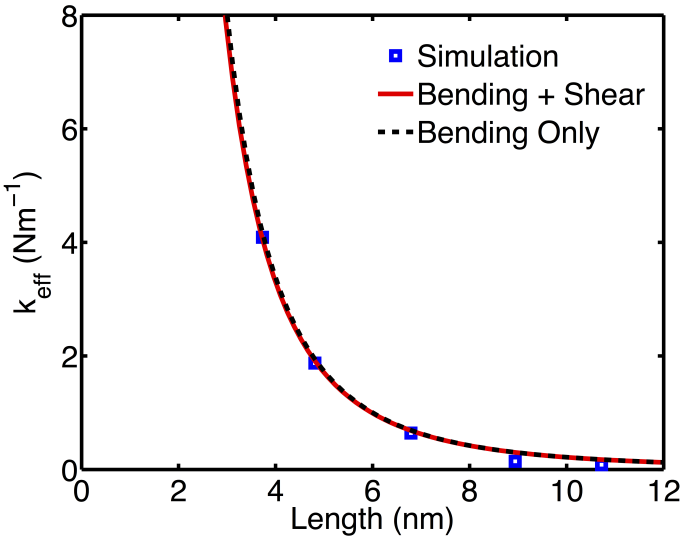

(b)

Figure 3-10: Effective bending stiffness as a function of length for (a) Aβ (1-40) amyloid fibril and (b) β-helices. The curve labeled "Bending + Shear" is the fit from equation 3.2 (extended beam model) and the curve labeled "Bending Only" is fit from equation 3.4 (pure bending model). The divergence of the two curves in (a) shows the predominance of shear deformation in the stacked amyloid structure for shorter length fibrils. In (b) the curves for pure bending and bending with shear are indistinguishable for all lengths considered, indicating that shear deformation does not play a role in the bending deformation of the β-helical structure. The difference in behavior between (a) and (b) is due to the structural differences between the amyloid fibrils and β-helices. In the amyloid fibrils, individual layers are only held together by weak hydrogen bonds and are easily sheared. The β-helix structure has a continuous, covalently bonded backbone, which in addition to hydrogen bonds along the helix axis, provides an additional layer of interaction and resistance to shear deformation.

thus transitions to a pure bending dominated deformation pathway). The pure bending deformation in the β-helical structure is seen via the highly non-linear deformed shape, even at the shortest length scales. In this structure, the additional connectivity of the continuous covalently-bonded backbone combined with the triangular shape of the fibril cross-section results in high shear resistance at all length scales.

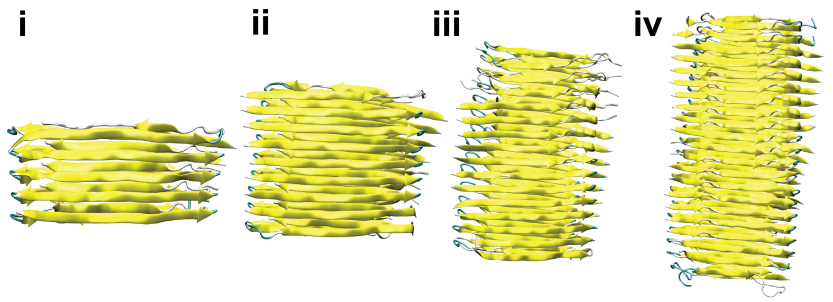

(a)

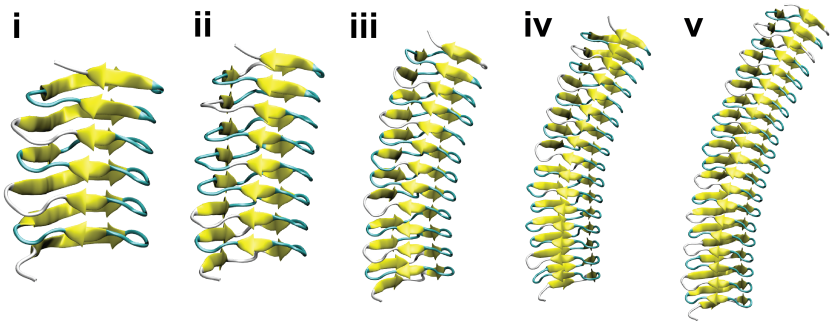

(b)

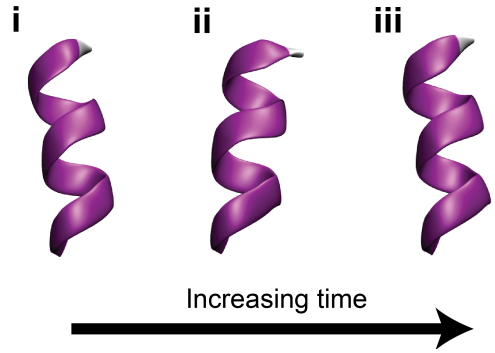

(c)

Figure 3-11: (a) and (b) show simulation snapshots of the bending deformation profiles for the different sizes of amyloid and β-helices considered in this study. The smaller amyloid structure in (a) feature a more linear strain distribution due to the larger shear contribution, while a nonlinear strain distribution consistent with pure bending deformation can be seen in even the smallest structure in (b). (c) shows three snapshots of the alpha helix structure under constant lateral loading from the same simulation trajectory. The entropically driven behaviour of the alpha helix can be seen in the unpredictable back and forth motion of the structure under constant applied force.

Figures 3-12(a) and 3-12(b) plot the displacement profiles for each case. The solid

curves show the continuum theory predictions from equation 3.6. It is notable that the continuum theory predictions describe the bending profiles of the two cross-β structures quite well. This result, combined with the effective bending stiffness analysis discussed above, indicate that although these structures are in no way "continuum beams", the robust mechanical properties imparted to the fibrils by the cross-β secondary structure causes them to behave in a way commensurate with continuum beams even at molecular length scales. Furthermore, as seen from the convergence of the extended and classical beam models in Figure 3-10, for length scales greater than $\sim 5-10$ nm, even just the classical bending theory (without shear effects) is an excellent model to describe the bending response of these types of protein filaments. Thus in the context of biomaterial design based on these types of amyloid and amyloid-like fibrils, where the length scales of individual fibrils is generally on the order of 100 –1000 nm, any design considerations regarding flexural properties can safely be made purely on the basis of the classical beam theory.

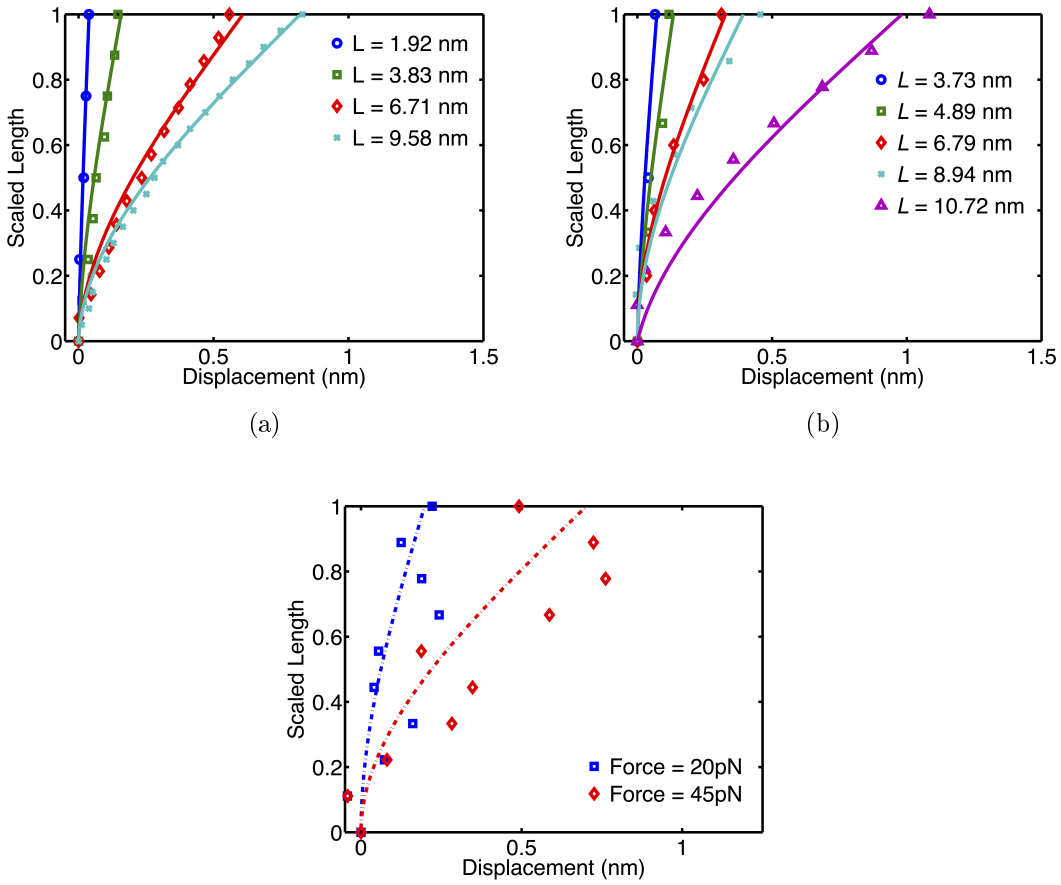

Figure 3-12: Bending profiles for the three structures considered in this study. (a) Amyloid fibril, (b) Îš-helix, and (c) Alpha helix. The solid curves in (a) and (b) show fits based on continuum theory (equation 3.6), and in general, the results agree quite well with the theory. The deformation profiles for the alpha helix structure for two different loads are shown in (c). The highly non-uniform nature of the deformation profiles illustrates the predominance of statistical fluctuations in the bending behavior. The dashed lines show fits to the profiles from equation 3.6 without the inclusion of the shear term (pure bending). The predicted bending rigidity from these fits is overestimated by up to two orders of magnitude (compared with experimental data), further illustrating that the classical continuum mechanical theory cannot be applied to describe the deformation behavior of the alpha helix structure.

In addition to the analysis of the importance of shear, material properties are estimated from the fitted values of D_b and D_t. For the amyloid fibril, the Young's Modulus is found to be $E = 9.9$ GPa and the bending rigidity $EI = 2.41 \times 10^{-25}$ Nm^2. These findings are in good agreement with previous simulation results [21,

24–26, 103] as well as experimental results [21, 22, 27] which find E in the range of 10 to 30 GPa and EI in the range of 0.1×10^{-25} to 2.5×10^{-25} Nm^2. The shear modulus is found to be $G = 10.2$ GPa for the amyloid fibril. This value is close to simulation results [26], which report a shear modulus of 5.6 GPa for Aβ(1-40) amyloid fibrils; the higher modulus reported here is possibly due to differences in loading conditions and simulation techniques, however the difference (approximately 5 GPa) is smaller than the spread in the experimentally measured values of the Young's modulus (approximately 20 GPa as indicated above). For the β-helical nanotube, the Young's modulus is found to be $E = 29.1$ GPa and the bending stiffness $EI = 6.2 \times 10^{-26}$ Nm^2. These findings agree well with previous results which find $E = 26.4$ GPa [104]. Due to the very small contribution of shear in the bending deformation of the β-helix structure, its shear modulus cannot be reliably extracted from these findings. The material properties extracted from this study are summarized in Table 3.2.

Table 3.2: Summary of the geometric parameters used as well as the mechanical properties extracted from this atomistic scale bending study.

			Structure		
Parameter/Property			Aβ (1-40) Amyloid	β-Helix	Alpha Helix
Cross-Sectional Area	A (m^2)		1.34×10^{-17}	—	—
Second Moment of Area	I (m^4)		2.52×10^{-35}	2.13×10^{-36}	—
Young's Modulus	E (GPa)	This Study	9.9	29.1	—
		Previous Work	10-30 [21, 22, 24–27, 103]	26.4 [20]	—
Shear Modulus	G (GPa)	This Study	10.2	—	—
		Previous Work	5.6 [26]	—	—
Bending Rigidity	EI (Nm^2)	This Study	2.41×10^{-25}	6.2×10^{-26}	$2\text{–}4 \times 10^{-28}$[a,c]
		Previous Work	0.1×10^{-25} –2.5×10^{-25} [21, 22, 24–27, 103]	—	$\sim 4 \times 10^{-30}$[b]
Persistence Length	ξ	This Study	$\sim 60 \mu$m[a]	$\sim 15 \mu$m[a]	$\sim 60 - 100$nm[a,c]
		Previous Work	0.5-100 μm [5, 25]	1.4μm [67]	~ 1 nm [105]

[a] These values are calculated from the bending rigidities found in this study
[b] This value is calculated from the persistence length reported in reference [105]
[c] These values are expected to disagree with literature findings. Since they are based on fits to continuum theory, the fact that they disagree to such a large extent further supports the idea that continuum theory cannot be used to describe the mechanical response of the alpha helix with a length greater than its persistence length.

A final analysis of deformation behavior of protein filaments is made on the basis of persistence length. Broadly, the persistence length provides a limiting length scale above which statistical/entropic fluctuations dominate and continuum mechanics does not well describe the deformation behavior. To examine this directly, we compare the behavior of the two β-sheet rich proteins, both with lengths on the order of 1–10 nm and $\xi > 1\mu$m, to that of an alpha helix with a length of 2.3 nm and $\xi \sim 1$ nm [105]. As established through the analyses above, both β-sheet rich structures

are well described by continuum theory. The alpha helix, however, is not. Figure 3-11(c) shows three snapshots from the lateral loading simulation of the alpha helix. Although a constant force is applied, the alpha helix moves back and forth erratically over the simulation trajectory. Figure 3-12(c) plots the average deformation profile of the alpha helix over the final 250 ps of the simulation for two different applied loads. Both profiles show the highly non-uniform bending behavior that originates from the large influence of entropic effects. The dashed curves in Figure 3-12(c) show fits to the bending profiles based on equation 3.3. The bending rigidities obtained from these fits are $EI = 4 \times 10^{-28}$ Nm^2 and $EI = 2 \times 10^{-28}$ Nm^2 for the 20 pN and 45 pN force levels, respectively. Based on a persistence length of 1 nm, however, the bending rigidity of the alpha helix should be $\sim 4 \times 10^{-30}$ Nm^2, a factor of up to 100 smaller than the values obtained from the continuum theory fits. This large discrepancy again demonstrates that the continuum theory cannot be used to describe the mechanical behavior of the alpha helix.

Figure 3-13 shows the distribution of tip displacements over the final 100 simulation steps for the three structures considered in this study (the distributions shown for the amyloid fibril and β-helix are for the shortest length of each structure); a Gaussian function is fit to each distribution. It is found that the fluctuations in the tip distribution for the amyloid fibril and the β-helix are quite small; the standard deviations of both distributions are approximately 0.05 nm (smaller than one Angstrom, the characteristic length of typical chemical bonds). In contrast, the distribution for the alpha helix spans a much larger range of tip displacements, and the standard deviation of approximately 0.5 nm. This distribution is consistent with the emergence of entropic elasticity, where the deformation behavior is dominated by fluctuations. This fluctuation analysis further shows that continuum mechanical theory breaks down for length scales that exceed the persistence length of filamentous protein structures, and that in this regime, the mechanical response can only be described by theories that incorporated statistical effects [106].

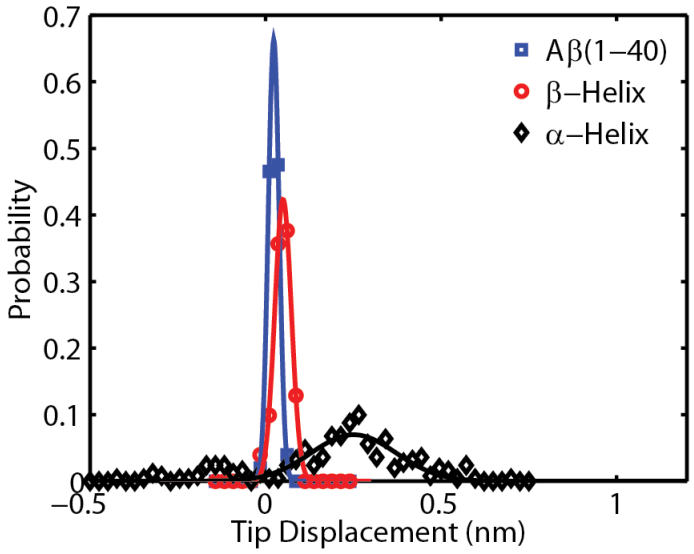

Figure 3-13: Fluctuation analysis for the three structures considederd in thebending simulations. The tip displacement dristributions are plotted as well as Gaussian fits. The amyloid and β-helix structures exhibit some small fluctuations (~ 0.1 nm) in the tip displacement ove the simulation trajectory, but in contrast, the tip displacement for the alpha helix is much larger, spanning over 1 nm. This analysis demonstrates that for the amyloid and β-helix structures with lengths well below their persistence lengths, fluctuations due to entropic effects play a negligible role in descrbing the overall mechanical response. In contrast, the deformation behavior of the alpha helix is dominated by fluctuations; continuum beam theory, which does not account fro these entropic fluctuationsm cannot provide an accurate description of the mechanical response of the alpha helix.

3.2.3 Conclusions

These results provide additional insight into the ways in which protein secondary structure type, size, and organization, affect mechanical behavior and properties. They also illustrate key differences in deformation behavior that arise from different structural motifs. It is found that both amyloid fibrils and β-helical nanotubes, with predominantly cross-β secondary structures and lengths well below their persistence lengths, are very well described by continuum mechanical theory. For the amyloid structure, the inclusion of shear deformation in the overall description of the bending behavior is essential at the smallest length scales owing to the fact that the hydrogen bonded Îš-sheet layers are easily sheared, but shear effects become negligible at longer lengths, specifically those that would be useful for functional materials based on these types of fibrils (typically > 100 nm). The behavior of the β-helix structure, however, can be described with just the contribution from pure bending. The continuous, covalently bonded backbone of the Îš-helix prevents significant shear deformation under lateral tip loading even for the shortest lengths considered. Further, mechanical properties calculated from this study are in good agreement with previous computational and experimental results (Table3.2).

The comparison of behavior on the basis of persistence length is very much in line with theoretical predictions. The two structures studied with lengths below their persistence length feature deformation behavior consistent with continuum theory, while the alpha helix structure with a length greater than its persistence length is characterized by more erratic behavior dominated by statistical (entropic) fluctuations. The persistence length is found to be an excellent metric for separating length scales at which continuum theory is applicable, and those for which a statistical treatment must be used to describe mechanical response [106].

3.3 Inter-Fibril Interactions

Amyloids are considered to be quite "sticky" and readily aggregate, and thus understanding the strength of the interaction which mediates this aggregation behavior can

provide some basic insights into the mechanics of larger scale amyloid based structures. This section discusses the atomistic simulations used to investigate the energy scale for the inter-fibril interactions. In particular, the inter-fibril sliding (shear) behavior is investigated which is closely related to the inter-fibril adhesion strength.

3.3.1 Methods

Two structures are considered in this study: the Aβ (1-40) amyloid fibril and the YadA collagen binding β-helix. The significant geometric differences in these two structures discussed above, including size and connectivity, allow for a comparative analysis which can elucidate important features of these amyloid and amyloid-like protein fibrils which impact and control their inter-fibril interactions.

As discussed later in Section 4.3.2, the dominant inter-fibril interaction for mesoscale and larger amyloid-based materials is the shearing interaction, or inter-fibril sliding. Thus for each of the two structures, a small scale shear test is set up to directly investigate this response. Figure 3-14 shows the initial structures for each of the fibrils investigated as well as a schematic of the boundary conditions applied (the structures are not shown to scale). Each structure comprises two protofibrils of length $\sim 3.5 - 4.5$ nm; after generating the initial configurations with VMD, the same equilibration procedure is followed as described in Section 3.1. For the shear test, one of the protofibrils is restrained and SMD pulling is performed on the other fibril with a velocity of 0.1 m s^{-1}. All other simulation parameters are identical to those described above in Section 3.1 for the tensile test simulations.

For each of the two structures, three independent shear tests are run; an additional 100 ps of equilibration is performed from the end of subsequent equilibration runs to obtain a new starting configuration. The results from the three runs are averaged together to reduce any stochastic effects in the inter-fibril response.

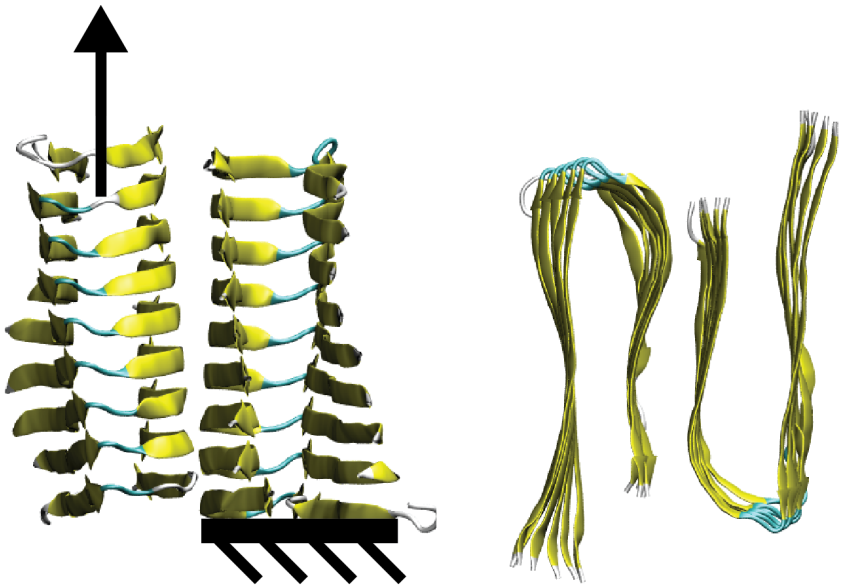

(a)

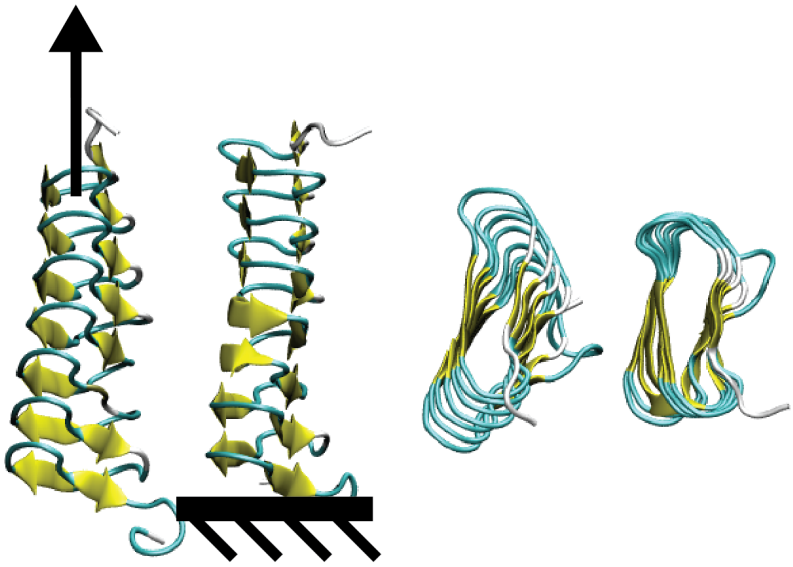

(b)

Figure 3-14: Initial structures and schematics of shear test boundary conditions for (a) the Aβ (1-40) amyloid fibril and (b) the YadA collagen binding β-helix. Each panel shows the side and top view. For the shear test, the right protofibril is restrained and SMD pulling is applied to the left protofibril at a constant velocity of 0.1 m s^{-1}. The two structures are not shown to scale, however it is noted that the Aβ structure in (a) features a much larger shear interface than the YadA structure (b).

3.3.2 Results and Discussion

Figure 3-15 shows the potential of mean force (PMF) for the two structures investigated and clearly shows a significant difference in the strength of their inter-fibril interactions. The shapes of the two curves are qualitatively quite similar, and both feature small "bumps" indicating a stick-slip behavior. This is verified via molecular visualization of the shear test trajectories with VMD; as the fibrils are pulled against each other, the β-strands find favorable configurations and stick for a short period of time, resulting in a small scale stick-slip response.

Although the two structures behave qualitatively similarly, they are quantitatively quite different. The energy scale for the inter-fibril interactions for the Aβ (1-40) fibril is ~ 17 times greater than that of the YadA collagen binding β-helix. The This is in stark contrast to the tensile test results in which the Aβ fibril was found to require only ~ 1.4 times the work to deform than the Yada collagen binding fibril. These results, as well as the relative interaction strengths of the inter- and intra-fibril interactions, are summarized below in Table 3.3. Importantly, in the Aβ (1-40) structure, the inter-fibril interactions are much stronger than the intra-fibril interactions, while in the Yada collagen binding β-helix, the opposite effect is observed as the intra-fibril interaction is stronger than the inter-fibril interaction.

Table 3.3: Summary of the energy scales for the inter- and intra-fibril interactions.

Structure	Maximum of PMF in Tension (kcal mol^{-1})	Maximum of PMF in Shear (kcal mol^{-1})	Relative Strength of Inter- vs. Intra-Fibril Interactions
Aβ (1-40) Amyloid Fibril	105.5	578.3	5.5
YadA Collagen Binding β-helix	74.8	33.6	0.45

The adhesion strength per unit length is estimated for the two structures by dividing the maximum of the PMF by the length of the shear interface. For the Aβ structure, this is found to be 13.8 kcal mol^{-1} Å^{-1}. This is in reasonable agreement with previous computational results which estimated a value of 4.39 kcal mol^{-1} Å^{-1} [107]; the difference is attributable to the different boundary conditions used (dynamic (in the present work) versus static). For the Yada collagen binding structure, it is estimated to be 2.02 kcal mol^{-1} Å^{-1}.

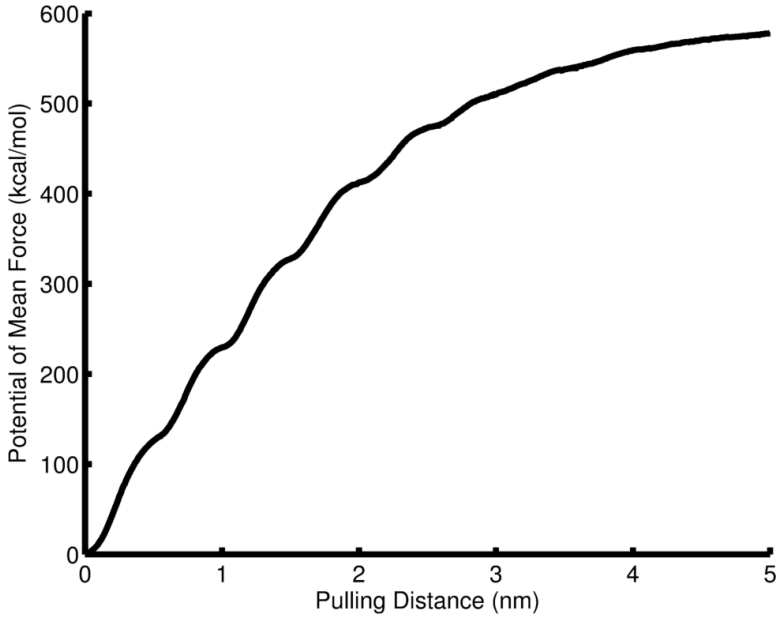

(a)

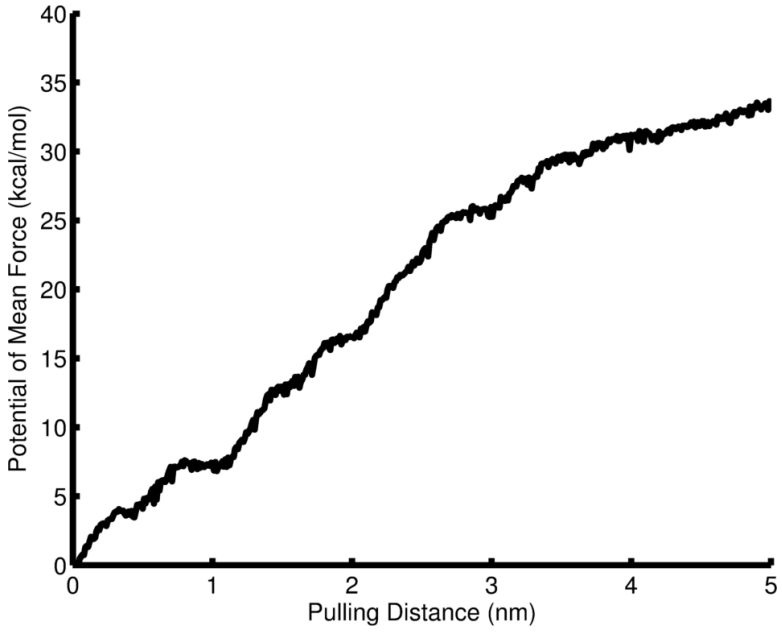

(b)

Figure 3-15: Potentail of Mean Force Curves from inter-fibril shear tests. (a) shows the response of the Aβ (1-40) amyloid fibril and (b) shows the response of the YadA collagen binding β-helix. The drastic difference in the scales of the two plots indicates the siginificant difference in the strength of the inter-fibril interactions for these two structures.

Figure 3-16 shows snapshots from the shear tests for the two structures and qualitatively illustrate the differences in deformation. The Aβ (1-40) (Figure 3-16(a)) fibrils maintain strong adhesion and alignment throughout the shear test, again indicating a strong inter-fibril interaction. In contrast, the YadA collagen binding β-helix fibrils with their much weaker inter-fibril interactions, do not maintain a strong inter-fibril interface during the shear as water molecules (not shown) are able to disrupt the interface (see Figure 3-16(b)).

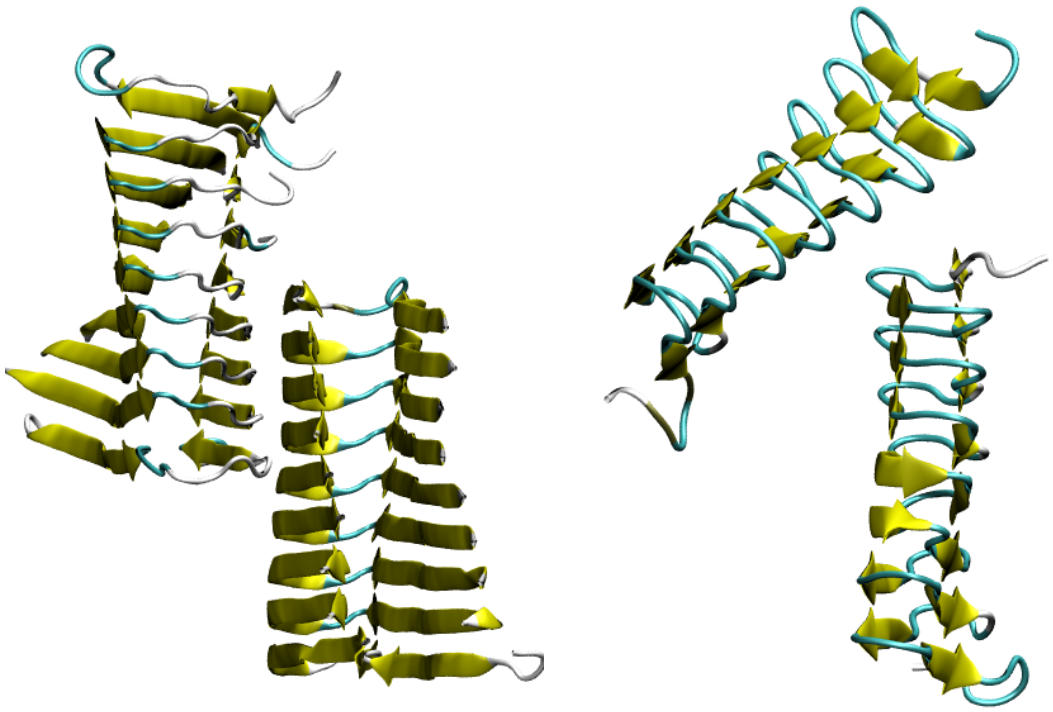

(a) (b)

Figure 3-16: Snapshots from the shear test simulations for the two structures considered. (a) shows the Aβ (1-40) amyloid fibril which maintains a parallel interface throughout the shear test due to its strong inter-fibril interactions. (b) shows the YadA collagen binding β-helix which exhibits deformation out of the plane of the inter-fibril interface due to its relatively weak inter-fibril interactions.

3.3.3 Conclusions

A simple shear test was performed to asses the strength of the inter-fibril interaction in two amyloid or amyloid-like structures with very different geometries and connectivities. The inter-fibril response, and more importantly the strength of the inter-fibril response relative to the strength of the intra-fibril interaction was found to be very different between these two structures. These significant differences in the relative interaction strengths could provide a very useful criterion for choosing amyloid or amyloid-like fibrils which optimize the mechanical response in different functional roles. Structures like the Aβ (1-40) fibril which have very strong inter-fibril interactions could form very strong adhesive films where the inter-fibril interactions serve as the foundation for the strength of the larger structure. However this may come at the cost of reduced deformability, as the relatively weak intra-fibril interactions can fail (fibril fracture) to facilitate maintaining existing inter-fibril connections. In contrast, structures like the YadA collagen binding β-helix structure may be preferable for applications requiring enhanced deformability, and it is possible that even in spite of the relatively low inter-fibril adhesion strength, these fibrils may yield robust larger scale structures. These effects will be investigated and discussed more thoroughly in Chapter 6. Furthermore, the results discussed here for the shear test are similar to those discussed above for the tensile tests (see Section 3.1) in that the qualitative features of the mechanical response are found to be mostly independent of the specific structure, but the specific mechanical properties are found to vary significantly across the different structures.

3.4 Chapter Summary

The origin of the excellent mechanical properties of amyloid and amyloid-like protein fibrils has long been known to be their cross-β secondary structure with a hydrogen bonded network extending the length of the fibril. What was not clear, however, is how the *specific* geometrical details of the structures affect the *specific* mechanical response. In a materials selection context, this becomes a problem considering the

fact that there are a large number of proteins which form amyloid or amyloid-like structures, and as new synthetic amyloid-inspired structures are created, guidelines are needed to aid in their design. This chapter explored the specific structure property relationships in amyloid and amyloid-like fibrils at the molecular scale and identified key features which control the mechanical behavior of individual fibrils.

Chapter 4

Coarse-Grained Model for Amyloid and Amyloid-like Fibrils

This chapter describes the development of a coarse-grained model to understand the mechanics of functional amyloid structures; the implementation of the model to investigated the mechanical properties of structures based on different amyloid or amyloid-like fibrils is discussed in Chapter 6. This modeling work builds on the atomistic scale results from Chapter 3 to continue the development of a bottom-up model which describes the behavior and mechanical response of amyloid and amyloid-like fibrils at multiple length scales.

4.1 Motivation

Existing Coarse-Grained Models

Previous studies in the literature have employed a variety of coarse-grained descriptions to study various properties of amyloid fibrils, including a aggregation kinetics [108] and elastic properties [109]. In particular, a series of papers by Paparcone *et al.* report the development of a bead-spring amyloid fibril model used to study the mechanical properties of amyloid fibrils and mesoscale assemblies of amyloid fibrils [24, 25, 68, 107]. This model, described in detail in Appendix A, provides the

framework on which the model described in this chapter is developed, and is implemented in a preliminary coarse-grained investigation of the properties of amyloid-based "nanowire" structures. The results of that study reveal some interesting behaviors in amyloid-based materials (see Appendix A for discussion); however, the model is very limited due to the fact that it was parameterized from force-controlled atomistic simulations. These boundary conditions do not allow for drops in the force to be observed as the displacement is increased, and thus do not capture many of the important features of the force-displacement response of amyloid structures which were identified and discussed in Chapter 3.

New Coarse-Grained Model

The new model developed and discussed here is simple by design but captures the relevant physics necessary to describe and investigate the mesoscale response of functional amyloid-based materials, in particular the drops in the force that occur due to hydrogen bond rupture during tensile deformation. Although the model is parameterized to quantitatively match the behavior and mechanical properties observed at the atomistic scale, the model is not intended to be quantitatively predictive for the mechanical properties at the mesoscale. While the mechanical properties should be on the correct order of magnitude, a simple model like the one described in this chapter is not intended to be truly quantitatively predictive. However, since the model is consistent between parameterizations of different amyloid and amyloid-like fibrils, it allows for excellent qualitative and comparative analysis of the relative performance of different constituent fibrils, and can allow for the identification of general features which optimize the mechanical performance of the mesoscale structures.

The goal of the coarse-grained modeling described in this chapter is to provide simple insights into the hierarchical mechanics of amyloid-based functional materials, and to allow for the development of the first materials selection guidelines for for *de novo* amyloid-based materials.

4.2 Functional Description

This section describes the functional formulation of the mesoscale amyloid fibril model. Amyloid and amyloid-like fibrils are described with a bead spring model in which three layers of the cross-β structure are coarse-grained into a single bead, and the properties of the beads and and springs are chosen to match the atomistic scale simulation results described in Chapter 3. The total energy is given by:

$$E = E_{NB} + E_b + E_\theta = \sum_{NBPairs} \varphi_{LJ}(r_{ij}) + \sum_{Bonds} \varphi_b(r_{ij}) + \sum_{Angles} \varphi_\theta(\theta_{ijk}) \tag{4.1}$$

Here φ_{LJ} is the typical 12-6 Lennard-Jones potential:

$$\varphi_{LJ}(r_{ij}) = 4\varepsilon \left[\left(\frac{\sigma}{r_{ij}} \right)^{12} - \left(\frac{\sigma}{r_{ij}} \right)^{6} \right] \quad r_{ij} < r_c \tag{4.2}$$

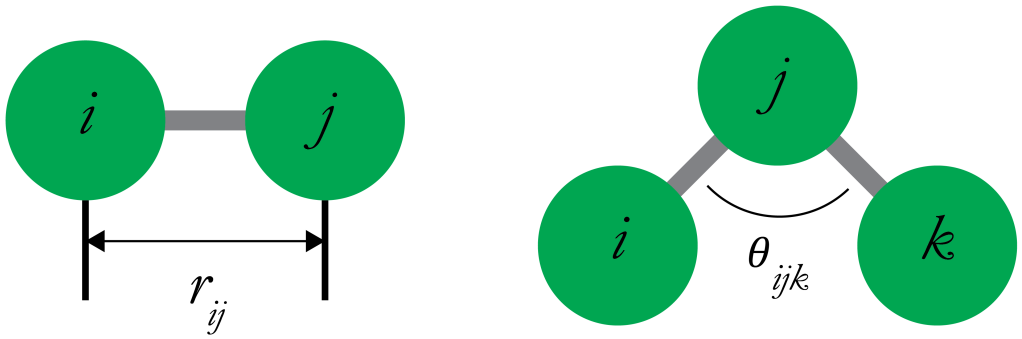

(a) (b)

Figure 4-1: A simple schematic of the (a) bonded interaction and (b) angle interaction. The bonded interaction is calculated as a function of the separtion between bonded beads and the angle interaction as a function of the angle formed by bonded triplets. The non-bonded interaction (not shown) is calculated for all non-bonded pairs within a prescribed cutoff distance.

The bond potential φ_b is described by a breakable Morse-potential with a shift to match the tensile response of the amyloid and amyloid-like fibrils described in

Section 3.1:

$$\varphi_b(r_{ij}) = D\left(1 - e^{-\alpha(r_{ij}-r_0)}\right)^2 + \delta\left(r_{ij} - r_0\right) \quad r_{ij} < r_{break} \tag{4.3}$$

where D and α are the parameters which control the energy scale and shape of the bond potential, and r_0 is the equilibrium bond length; a simple schematic of the bonded interaction is shown in Figure 4-1(a). Since the spacing between β-sheets in all of the amyloid and amyloid-like fibrils is controlled by the length of the hydrogen bonds along the fibril axis rather than the specific amino acid sequence, the value for r_0 is the same for every structure considered with $r_0 = 14.4$ Å (the spacing between β-sheets is 4.8 Å and each bead comprises 3 β-sheets). An example force-displacement response for this bond potential is shown in Figure 4-2; this functional form captures the initial peak and drop in the stress-strain response of the amyloid and amyloid-like fibrils which results from the cooperative deformation and failure of a group of hydrogen bonds in the fibril cross-section, and the addition of the shift (the $\delta(r_{ij} - r_0)$ term) captures the small stress response observed at larger strains during the one-by-one rupture of hydrogen bonds.

As discussed in Section 3.2, shear effects are found to be unimportant in determining the bending response of these cross-β structures beyond very short fibril lengths. Thus in defining the angle potential for this coarse-grained description, shear effects are ignored and the angle term is defined up to describe classical bending with a harmonic bending function:

$$\varphi_\theta(\theta_{ijk}) = K_{bend}\left(\theta_{ijk} - \theta_0\right)^2 \tag{4.4}$$

with $\theta_0 = 180°$ for all structures considered. The bending stiffness is derived by utilizing an energy equivalence between the coarse-grained bending potential (Equation 4.4) and the elastic energy from classical bending theory [107]. Under bending deformation for three beads in angle triplet (similar to three point bending), the

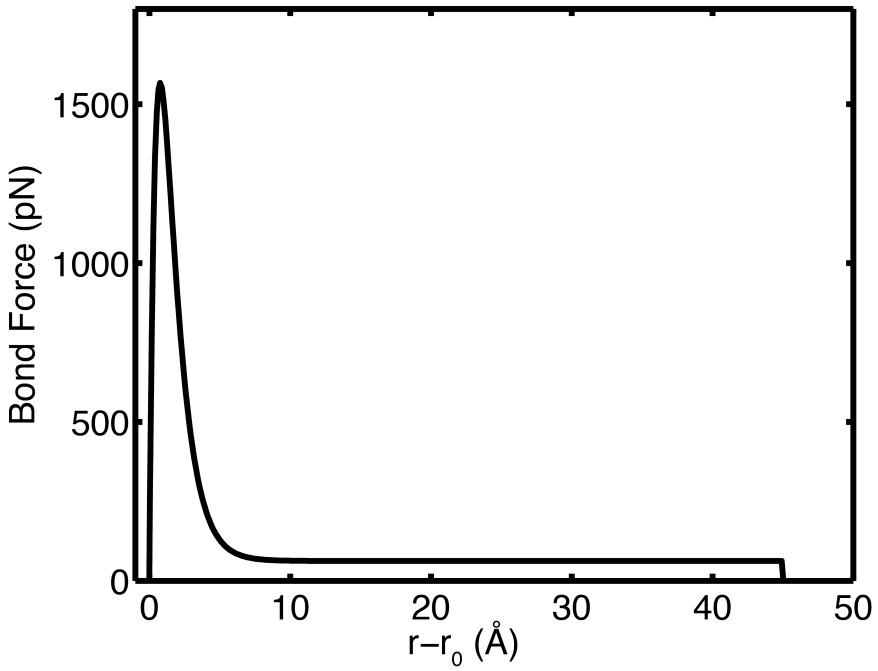

Figure 4-2: An example bond potential (force vs. extenstion) for the coarse-grained amyloid and amyloid-like fibril model. The breakable Morse bond with a shift is able to describe the relevant tensile behavaior for the amyloid and amyloid-like fibrils described in Section 3.1.

displacement perpendicular to the fibril axis is given by

$$\delta = \frac{PL^3}{48EI} \tag{4.5}$$

where P is the applied load and $L = 2r_0$ is the axial length of the angle triplet. The total elastic energy in bending resulting from such displacement δ is given by

$$U(\delta) = \frac{6EI}{r_0^3}\delta^2 \tag{4.6}$$

By setting this energy equal to the energy for the angle interaction φ_θ (Equation 4.4) and noting that for the triplet of beads in the angle with the displacement applied to the central bead (and for small deformations), $\theta - \theta_0 \approx 2\delta/r_0$. The resulting bending stiffness is given by

$$K_{bend} = \frac{3EI}{r_0} \tag{4.7}$$

The coarse-grained model is implemented and run with the LAMMPS simulation package on a multicore linux workstation and utilizes GPU acceleration to enhance the performance of the simulations [**?**, 110–112].

4.3 Model Parameterization

In general, a fine-trains-coarse approach is used to parameterize the coarse grained model; this approach is described in Section 2.2.2. The parameters for the coarse-grained amyloid fibril model are determined by matching the mechanical response measured from fully atomistic simulations to the response of an equivalent coarse-grained description. This is essentially a "force-matching" method for parameterizing the force field [113].

In order to provide more reliable fits, the matching of the mechanical response is carried out via the potential of mean force (PMF) for each interaction which is parameterized. The PMF is defined as the cumulative work performed along a desired reaction coordinate; in this case the reaction coordinate is the tensile or shear dis-

placement for the tensile and inter-fibril shearing tests, respectively, and the PMF is the cumulative sum of the force times the displacement. Since the PMF is essentially an integral of the force-displacement response, it is much smoother than the actual force-displacement curve and thus fitting the coarse-grained PMF to the atomistic scale PMF is more reliable and diminishes the effects of noise in the data. Furthermore, by comparing the PMFs for the different deformation pathways both for single structures and between structures, insights into the relative importance of different deformation pathways can be highlighted by comparing the relevant energy scales.

4.3.1 Fitting Procedure

The fitting of the coarse-grained model is carried out by performing a brute force parameter sweep over the relevant parameters in the coarse-grained model. Small coarse-grained systems are set up which match the size of the atomistic scale simulations described in Chapter 3, and equivalent mechanical test simulations are defined. These simulations are run while sweeping through a range of parameters for the potential function being fitted, and the set of parameters which minimize the square error between the PMF of the coarse-grained response and the PMF of the atomistic response are chosen as the best fit. This procedure is iterated over successively smaller intervals with a smaller loop increment for each parameter to refine the fits. This procedure is carried out in MATLAB (see Appendix B).

4.3.2 Non-Bonded Interactions

The two parameters which describe the non-bonded interactions are the Lennard-Jones parameters ε and σ. In the coarse-grained description, the non-bonded interactions control the inter-fibril mechanics; the inter-fibril properties discussed in Section 3.3 are used to parameterize the coarse-grained model. It is noted that there are many methods which can be used to parameterize these kinds of interactions; perhaps the most common is to match the potential energy as a function of inter-fibril separation between the coarse-grained and fully atomistic representations. In the

present work, however, the parameterization is carried out such that the inter-fibril shear response of the coarse-grained model matches that of the atomistic response. The work described later in Chapter 5 and Appendix A shows that sliding of chains or fibrils (inter-fibril shear) is an essential deformation pathway in determining the global mechanical response of the systems of interest, and thus the coarse-grained description described here is parameterized using the relevant deformation pathways. A parameterization based on the potential energy as a function of inter-fibril separation might be a better description for a model meant to describe static structures, but for the dynamic mechanical response investigated with the present model the inter-fibril shear response is a more appropriate training test.

First, the parameter σ is directly related to the physical size of the amyloid or amyloid-like fibrils. The mean of the radii of gyration in the two directions perpendicular to the fibril axis are used to define the equilibrium non-bonded distance, which is related to σ by

$$r_0^{NB} = 2^{\frac{1}{6}}\sigma \tag{4.8}$$

It is noted that this value defines the radius of the spherical beads, which is always larger than the bond distance between adjacent beads within a fibril (14.4 Å). To account for this and to prevent the non-bonded potential from creating a compressive stress in the fibrils, the non-bonded interaction is suppressed for first, second, and third nearest neighbors which are bonded within a fibril (the so-called 1-2, 1-3, and 1-4 interactions). Thus there is significant overlap of the beads and the σ parameter essentially defines the radius of cylindrical fibril.

The energy scale for the non-bonded interactions is defined by the ε parameter; it defines the depth of the potential energy well in the Lennard-Jones potential. The value of ε for each amyloid or amyloid-like structure is determined through the fitting procedure described above (see Appendix B for the MATLAB code). Figure 4-3 shows an example of the atomistic scale shear test alongside the coarse-grained representation.

An example of the atomistic scale PMF for the inter-fibril shearing response and

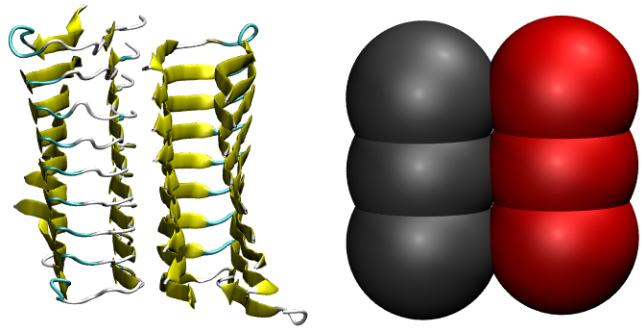

(a)

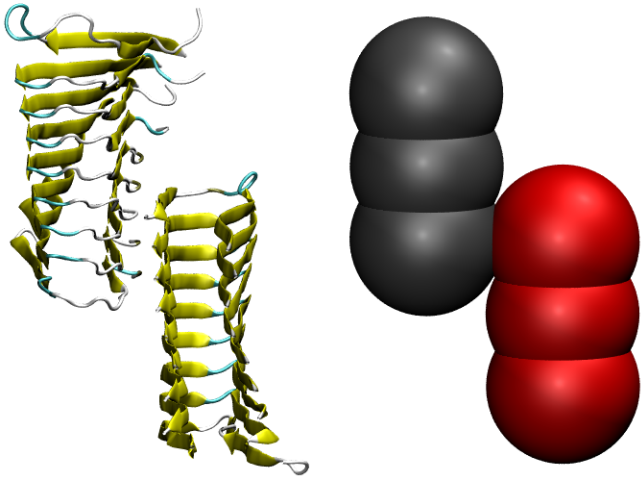

(b)

Figure 4-3: Schematic of the shear test setup for the non-bonded interaction parameterization. (a) shows the initial structure and (b) shows a snapshot after some shear deformation has been applied. In each panel the atomistic structure is on the left and the equivalent coarse-grained representation is on the right.

the corresponding coarse-grained PMF with the best fit ε is shown in Figure 4-4. The coarse-grained model shows good overall agreement with the atomistic scale results; the humps in the coarse-grained PMF are due to the spherical nature of the beads which results in larger scale roughness a the shear interface compared to the atomistic fibrils. Importantly, the coarse-grained description does an excellent job on average of capturing the relevant energy scales involved in inter-fibril shearing.

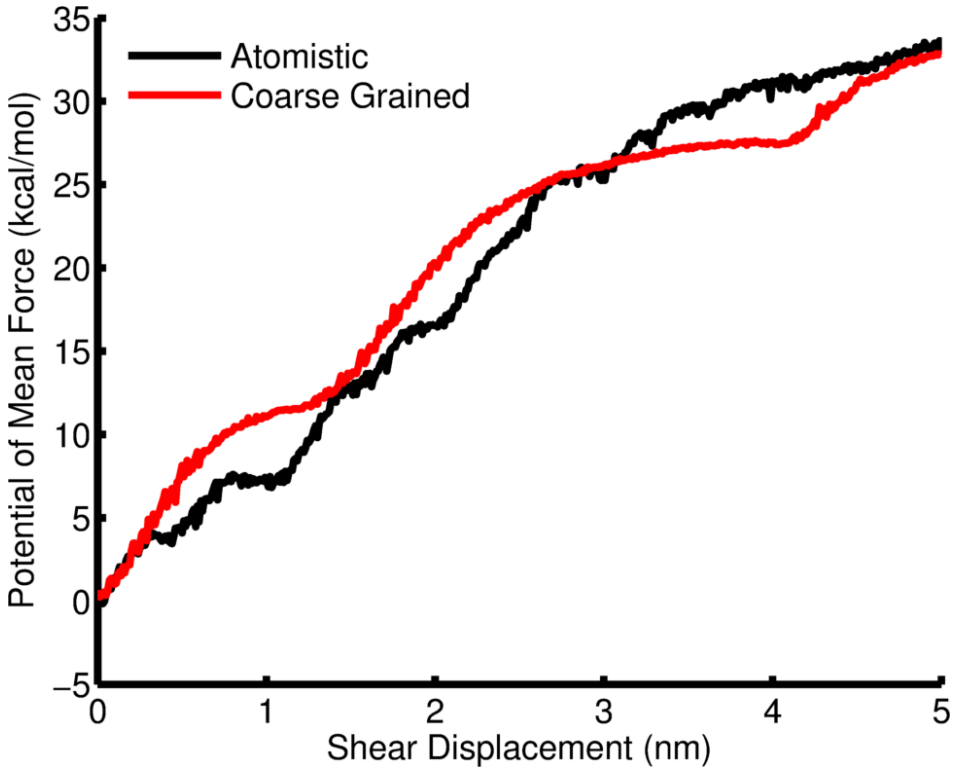

Figure 4-4: Representative atomistic and best fit coarse-grained PMF curves from inter-fibril shearing simulations; this particular set of curves are for the YadA collagen bindinig domain β-helix fibril. The coarse-grained description shows good agreement with the atomistic response.

4.3.3 Bonded Interactions

The bonded interaction in the coarse-grained model is described by the four parameters D, α, δ, and r_{break}. The values of D and α together define the energy scale and shape of bonded interaction potential, δ sets the force in the bond for large strains,

and r_{break} defines the cutoff for the bonded interaction (the bond distance at which the bond breaks). The parameterization for D, α, and δ is carried out using the fitting procedure described above and fitting the results to the atomistic scale tensile test results from Section 3.1. Figure 4-5 shows a representative setup of the atomistic and coarse-grained tensile test used to parameterize the bond potential.

In the present work, r_{break} is set to 45 Å for all structures; while there is some variation in the breaking distance between structures, the force values at large bond strains are very small and thus are not expected to contribute significantly to the mechanical response. It is noted that the β-helical structures do not have a true failure point like the stacked structures do after all of the hydrogen bonds between two β-strands are broken due to the addition of the continuous covalently bonded backbone. However it was seen in Section 3.1 that the stress-strain response of the β-helices is very similar to the stacked structures, so a similar cutoff is implemented; this cutoff is also necessary for computational efficiency.

A representative tensile test PMF for an atomistic and coarse-grained representation is shown in Figure 4-6, in this case for the Aβ (1-40) amyloid fibril. Again the coarse-grained model exhibits excellent agreement with the atomistic scale results.

4.3.4 Angle Interactions

The angle interactions which define the bending properties in the coarse-grained model are controlled by the bending stiffness, K_{bend}, defined above in Equation 4.7. The bending stiffness is directly related to the bending rigidity EI which in the present work is calculated from the elastic properties determined from the atomistic scale tensile test results discussed in Section 3.1. The cross-sectional moment of area I is calculated for each structure from the atomistic geometry and is multiplied by the Young's modulus E to obtain the bending rigidity and ultimately the angular bending stiffness K_{bend} for each amyloid or amyloid-like structure. It is noted that the bending rigidity is also related to persistence length of the fibrils by

$$\xi = \frac{EI}{k_B T} \tag{4.9}$$

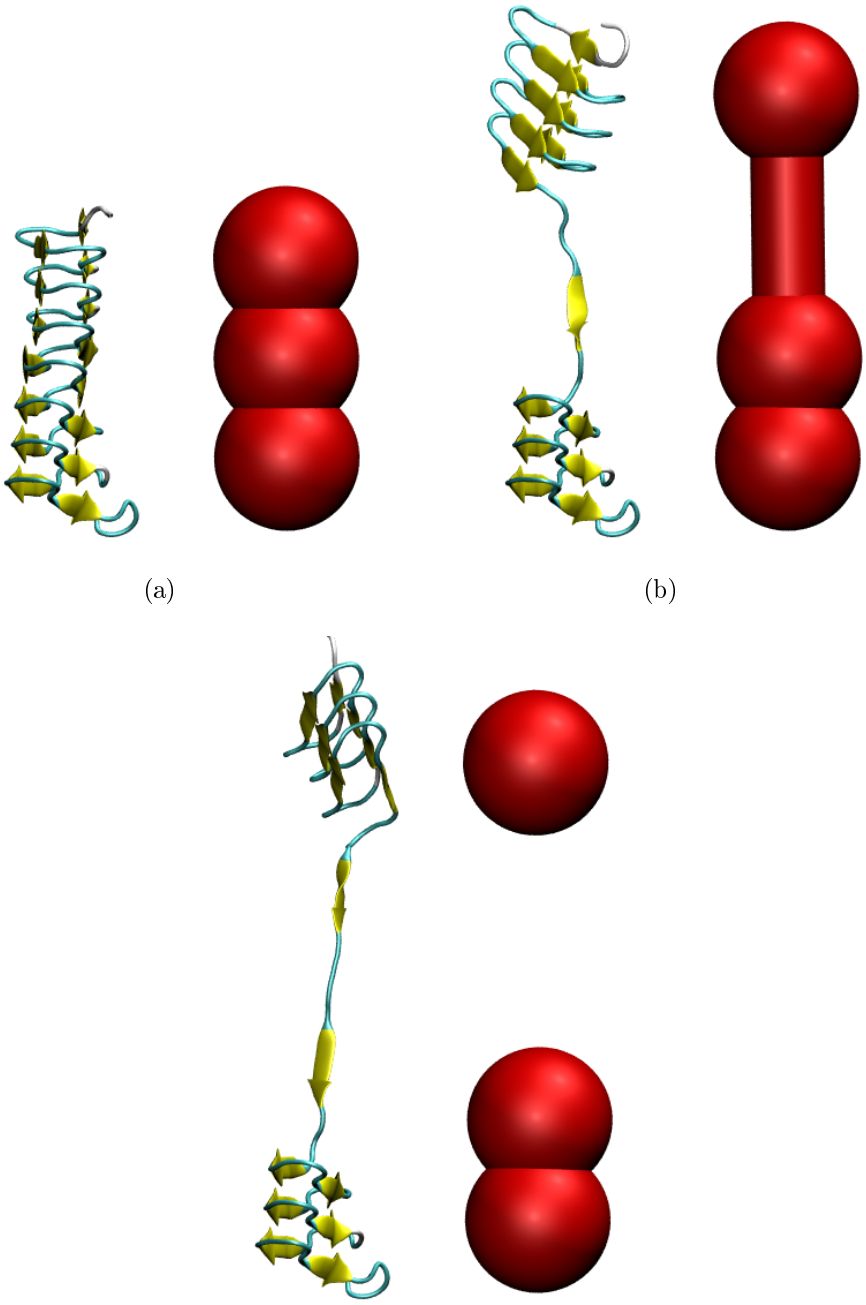

(a) (b)

(c)

Figure 4-5: Schematic of the shear test setup for the non-bonded interaction parameterization. (a) shows the initial structure, (b) shows a snapshot after some tensile deformation has been applied, and (c) shows a snapshot in which the deformation has exceeded the breaking distance for the coarse-grained bond potential. In each panel the atomistic structure (shown with a cartoon representation) is on the left and the equivalent coarse-grained representation is on the right.

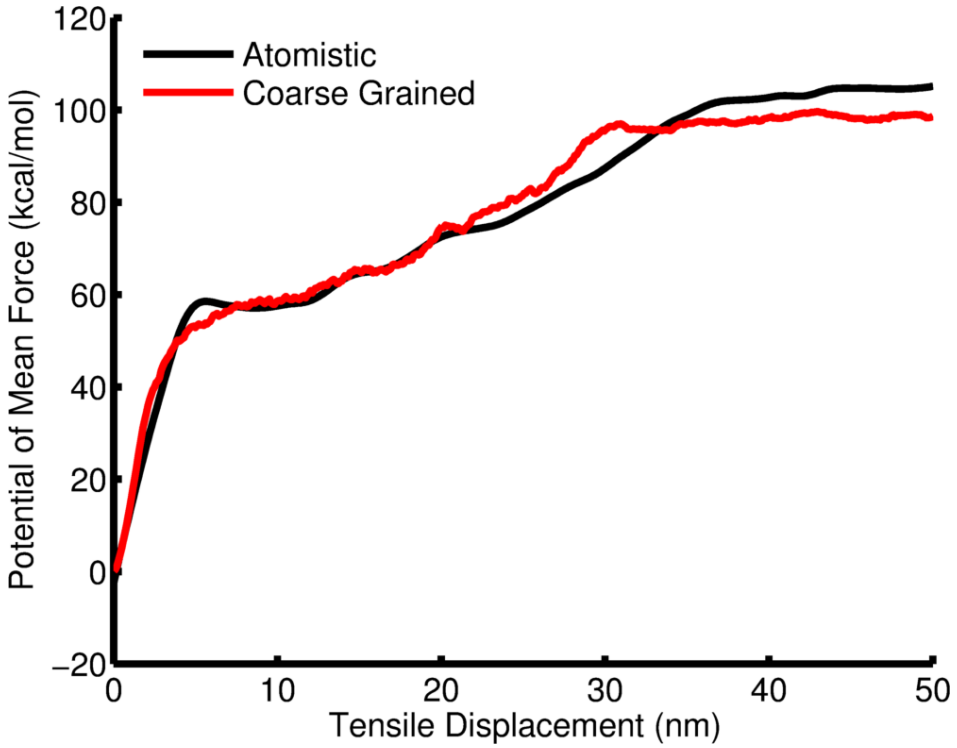

Figure 4-6: Representative atomistic and best fit coarse-grained PMF curves from tensile test simulations; this particular set of curves are for Aβ (1-40) amyloid fibril. As in the inter-fibril shearing simulations, here the coarse-grained description shows good agreement with the atomistic response.

where k_B is the Boltzmann constant and T is the temperature. It follows that the bending stiffness can be defined through the persistence length by

$$K_{bend} = \frac{3k_BT\xi}{r_0} \tag{4.10}$$

This allows for a simple validation of the value for the bending stiffness for structures with persistence lengths which have been measured experimentally.

4.3.5 Other Simulation Parameters

The final parameters required to complete the coarse-grained description are the bead mass, as well as the specific simulation parameters used to define and integrate the equations of motion for the coarse-grained model. The mass of each bead is simply defined by the total mass of the atoms which comprise three β-sheet layers in the atomistic structures. For stacked structures this definition is straightforward; for helical structures, the mass per layer is defined by taking the total mass of an atomistic structure and dividing by the total number if periods of the helix structure.

Langevin Dynamics simulations (described in Section 2.2.3) are performed with the coarse-grained description. A time step of 100 fs is used for all coarse-grained simulations, and the damping parameter (γ) is calculated for each amyloid-or amyloid-like fibril from the bead size (discussed above in Section 4.3.2) and using the dynamic viscosity of water $\eta = 128.3$ kcal fs mol^{-1} Å^{-3}.

4.4 Film-like Geometry Generation

Many of the applications of functional amyloids utilize the fibrils in a film-like geometry, and thus the coarse-grained modeling discussed in this chapter will focus on the properties of amyloid-based films. One of the simplest methods by which these amyloid-based films are generated experimentally is by simply casting a solution containing amyloid fibrils and allowing the solution to evaporate [19]; alternatively, a vacuum filtration method has been used in which a solution of amyloid fibrils is

drawn through a filter, resulting in a thin film being deposited onto the filter which can then be removed to achieve a free standing film [49]. The film-like geometry is created *in silico* with a deposition process which is meant to emulate these types of deposition methods. Initial structures are generated with fibrils randomly oriented in a direction parallel to the film plane and a random height above the film; an example structure is shown in Figure 4-7(a). It is noted that periodic boundary conditions are used in the film directions to create an "infinite" film geometry. The film is "deposited" by adding a wall potential parallel to the film plane to create a surface onto which the film can be deposited and then by imposing a gravitational force onto the fibrils in the direction perpendicular to the film plane. The wall potential is defined by a 9-3 Lennard-Jones interaction:

$$\varphi_{wall}(z) = \varepsilon_{wall}\left[\frac{2}{15}\left(\frac{\sigma_{wall}}{z}\right)^9 - \left(\frac{\sigma_{wall}}{z}\right)^3\right] \tag{4.11}$$

where z is the height of a particle above the wall and ε_{wall} and σ_{wall} define the interaction strength and equilibrium distance for the wall potential, respectively. The values for these parameters are chosen to be similar in magnitude to those of the non-bonded interactions within the fibrils; the actual values for the wall potential are not considered important as the wall potential is implemented to simply provide a surface onto which the fibrils can be deposited.

After the deposition process, the wall potential is removed, and the free-standing film is allowed to equilibrate. During this equilibration process, the lateral dimension of the film is allowed to change in order to relax the structure and prevent the buildup of any residual stresses. Figure 4-7(b) shows a representative amyloid film structure following the equilibration procedure. As evidenced by the differences between the initial configuration with relatively uniform coverage of the film and the final equilibrated film structure, the equilibration process results in significant aggregation of the fibrils and the film structure resembles a network of small scale bundles (similar to the structures discussed in Appendix A). The strong attraction between the amyloid and amyloid-like fibrils combined with their typically high bending rigidity and

brittleness results in a significant amount of fibril fracture during the equilibration process; the extent to which this effects the mechanical properties of the mesoscale structures is examined in Chapter 6.

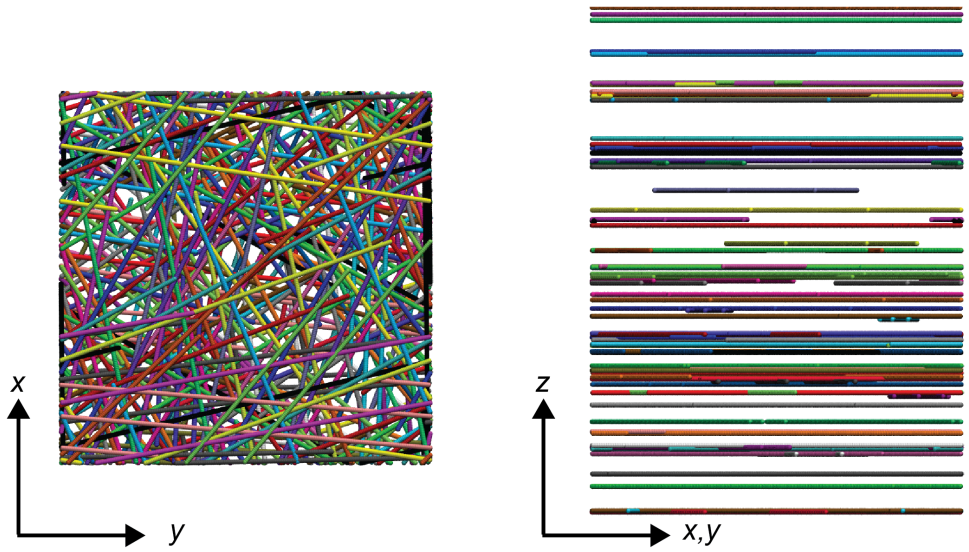

(a)

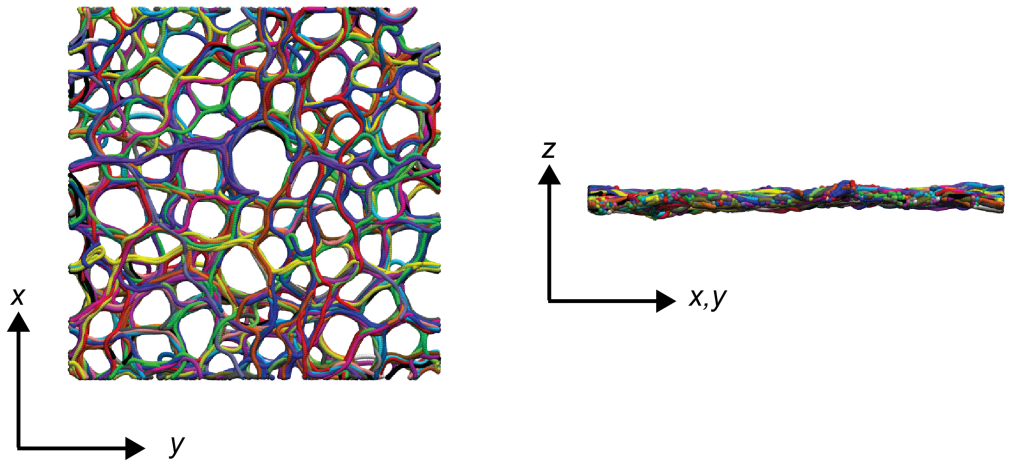

(b)

Figure 4-7: Representative simulation snapshots demonstrating the method used to generate film-like geometries with the coarse-grained amyloid and amyloid-like fibrils. (a) shows the side and top view of the initial structure with parallel to the film plane but with random orientations and a random height above wall potential (effectively the deposition substrate). (b) shows the top and side view of the same structure following the equilibration runs.

4.5 Model Validation

As stated above, the primary goal of the model described in this chapter is to allow for qualitative and comparative analysis of the performance of mesoscale structures based on different amyloid or amyloid-like fibrils. However, the model should provide reasonable quantitative agreement with experimental results for the mechanical properties of similar functional amyloid-based structures to be considered a valid model. A simple study is discussed in this section which provides such validation for the model fitting procedure described above.

A bending simulation is performed to emulate the three point bending experiments performed by Knowles, *et al.* [19] on free-standing amyloid-based films. This study is one of the few in the literature which has directly reported the mechanical properties of a functional amyloid-based structure. They found the Young's modulus for films based on β-lactoglobulin or lysozome protein fibrils to be in the range of 5-7 GPa. It is noted that a direct comparison for these structures cannot be made since the atomistic structures of the amyloid form these proteins are not available in the Protein Data Bank and therefore atomistic scale simulations from which a coarse grained model could be parameterized could not be performed. In this validation study, a film structure comprising fibrils of the Aβ (1-40) amyloid fibril are used; although the structures are different, the general similarity of the mechanical properties of amyloids should allow for a reasonable comparison with this structure.

The bending simulation is set up to emulate the boundary conditions of the three-point bending test; the boundary conditions are shown schematically in Figure 4-8a. The film is square with initial dimensions of 341 $\times$ 341 $\times$ 21 nm. 15 nm on the edges of the film in one of the film plane directions are held fixed, and a cylindrical indenter with a radius of 25 nm is created parallel to the film and subsequently moved downward into the film at a constant velocity of 1 m s^{-1}. The indenter interacts with the film via a harmonic interaction with a spring constant of 100 kcal mol^{-1} $^{-1}$. The force on the indenter is recorded as a function of the indentation depth and a linear fit is performed on the results to obtain an effective stiffness, k_{eff}. The analysis of

the effective stiffness is performed as in [19] to obtain the modulus from the measured stiffness of the film. The modulus is given by:

$$E = \frac{k_{eff} L^3}{48 I} \tag{4.12}$$

where the cross-sectional moment of inertia is:

$$I = \frac{w h^3}{12} \tag{4.13}$$

where w is the width of the film (in the direction parallel to the axis of the cylindrical indenter in the present study), L is the free (unclamped) length of the film, and w is the film thickness [114].

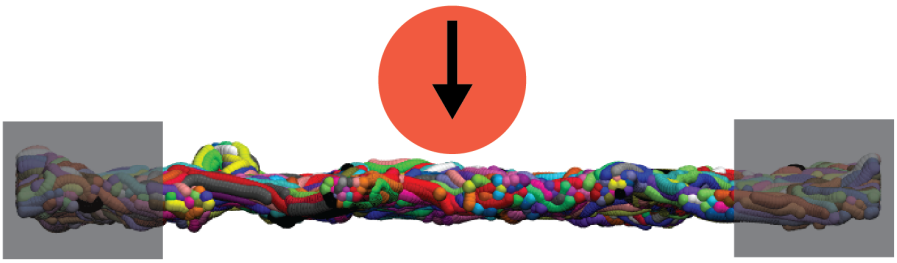

(a)

(b)

Figure 4-8: The indentation test setup used to emulate the three point bending of the amyloid-based film. The edges of the film are held fixed and a cylidrical indenter is depressed into the film at a constant velocity. (a) shows the initial setup and (b) shows the structure after the indenter has casued significcant bending in the film.

Figure 4-9 shows the force-displacement curve for the three point bending validation study along with a linear fit from the first 10 nm of displacement. The bending stiffness k_{eff} is found to be 1.177 N m^{-1} which corresponds to an elastic modulus of 2.7 GPa. This value is smaller than the values reported by Knowles *et al.* by a factor of ~ 2, however this difference could be attributed to a number of differences between the simulation and the experiment including the different structures tested or the small differences in the boundary conditions.

Importantly, the the modulus measured in the indentation study described here is on the same order of magnitude as the experimental results; this is considered to be reasonable quantitative agreement for a coarse-grained model of this nature. Even

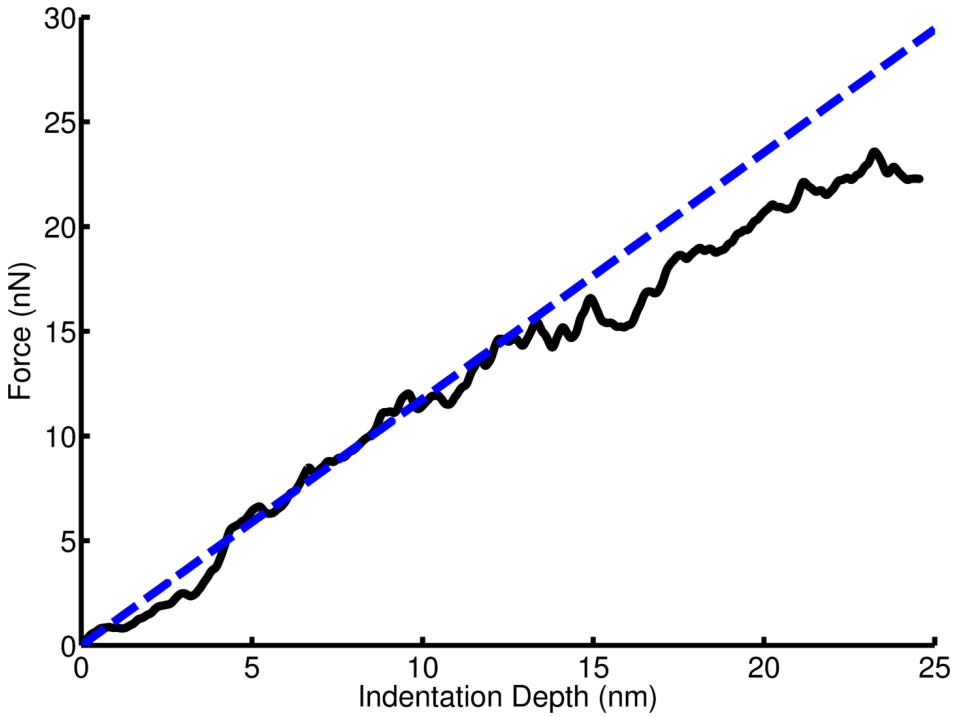

Figure 4-9: Force vs. indentation depth for the bending validation study. The blue line shows a linear fit from the first 10 nm of indentation from which the bendinging stiffness k_{eff} is determined. The elastic modulus of the film calculated from the bending stiffness agrees well with experimental values for similar structures.

though the model was not trained against any experimental data and was constructed purely in a bottom-up fashion, the results agree well with experimental results for similar systems, and thus this study provides validation for the model and the parameterization methods described in this chapter.

4.6 Chapter Summary

This chapter described the development of a new coarse-grained model for amyloid and amyloid-like protein fibrils. As discussed in Chapter 3, the specific amino acid sequence or molecular geometry of the amyloid or amyloid-like fibrils has very little effect on the deformation behavior and the character of the force-displacement (stress-strain) response. Thus the functional form of coarse-grained model was developed to capture this "universal" force-displacement response including the failure of the fibrils, and a parameterization method was followed such that the mechanical properties of the coarse-grained descriptions match those found in the atomistic scale training simulations. A method for creating film geometries was also discussed; these geometries are relevant in the broad field of functional amyloid based materials. Finally, since the parameterization method used in this work is based only on other simulation results, a simple validation study was performed to ensure that the coarse-grained description developed here can provide reasonable agreement with the results of experimental studies on similar functional amyloid-based materials. This study did find reasonable agreement with an experimental result for a three point bending test on amyloid-based films; the young's modulus found in the simulation is of the same order of magnitude as that found for similar protein fibrils, indicating the validity of the model.

The model discussed here is simple by design, but still captures the relevant physics and mechanical properties of amyloid and amyloid-like fibrils and thus can be easily extended to study a variety of cross-β protein fibrils and other similar structures. An investigation of the adhesive response of two different cross-β fibrils using this model is discussed in Chapter 6.

Chapter 5

Adhesive Modeling

This chapter takes a brief detour from the discussion of amyloid protein based materials; it describes the development and validation of an adhesion model for amorphous polymer adhesives. Although these types of adhesives are quite different in form and function from typical amyloid-based biomaterials, including amyloid-based adhesives, the model is general and is easily extended to investigate the adhesive properties of such materials (see Sections 5.2 and 6.3). Furthermore, the work described in this chapter elucidates some basic design principles which lead to optimal adhesive performance and which can be applied to amyloid-based functional materials to further aid in the materials selection and design processes. In addition, this chapter explores the interesting synergy between enhancing the design of *de novo* biomaterials via the study of synthetic materials (such as amorphous polymer adhesives), and the improvement and optimization of such synthetic materials through bioinspired material design.

5.1 Polymer Adhesive Model

In this section, a simple coarse-grained polymer model is developed and used to study the effects of crosslinking on the adhesive response of amorphous polymer films. Importantly the mechanical characterization methods discussed in this chapter provide a foundation on which the mechanical properties of functional amyloid-based materials

can be evaluated; this work is described in Chapter 6.

5.1.1 Background

Amorphous polymers are major components of both naturally occurring and synthesized adhesive materials, yet many simple effects including the interplay between crosslink density and the molecular scale mechanisms which control adhesive performance remain poorly understood. In nature, such adhesive materials are often found to play an important functional role at diverse interfaces. For example, spider silk uses groups of branching silks as glued to achieve it adhesion that is able to secure the edges of web structures subjected to wind or impact loading [115, 116]. Other examples include gecko feet, muscle and barnacle adhesion plaques, and amyloid protein biofilms, which generally also achieve impressive adhesion through amorphous protein structures which have only weak interactions such as Van der Waals forces [5,117–121]. The fascinating interfacial mechanics of these materials are found to be derived from the cooperative and synergistic integration of their building blocks [122], and these natural adhesives possess mechanisms to maximize adhesive performance in a variety of environments; they could prove invaluable as inspiration for the design of new synthetic adhesives. To apply these concepts to synthesized amorphous polymer adhesives, however, it is critical to understand how the mechanics and chemical interaction of the constituent polymer chains can be designed and tailored to control deformation mechanisms at the molecular scale and ultimately optimize the adhesive response.

One of the most common applications of synthesized amorphous polymer adhesives is in pressure sensitive adhesives (PSAs), used both in industrial and consumer grade tape and label products, in which temporary adhesion to diverse surfaces is required. These adhesives are characterized by their ability to form an adhesive bond just by the application of a small compressive force, as well as the ability to be completely removed without leaving a residue upon bonding [123, 124]. PSAs are commonly made a variety of polymers of low glass transition temperatures including natural rubbers, acrylics, and styrenic block copolymers [123, 125]. They are very

different from many irreversible adhesives such as epoxies that undergo some form of curing or setting process with phase transformations, which result in a drastic change in rheological properties, as well as the formation of chemical bonds between the adhesive and the adherend. In contrast, amorphous polymer PSAs do not undergo any phase transformations and they achieve adhesion in a similar manner to many natural adhesives, solely in the solid state via Van der Waals interactions [123, 125–127].

The performance of amorphous polymer adhesives is strongly dependent on the rheological properties of the constituent polymers. There is a clear trade-off in performance with changes in the stiffness of the polymer film. In general, the stiffness must be low enough that the adhesive is able to deform and make sufficient contact with the surface as described by the Dahlquist criterion [128], but the stiffness must also be large enough to provide sufficient resistance to deformation and to prevent cohesive failure [125]. Furthermore, a significant viscous response is desirable to promote energy dissipation during debonding (and thus achieve a more robust adhesive bond) [129]. Molecular weight can also have an important impact on the adhesive response via modulation of the rheological response [123–125, 130–133]. Low molecular weight polymers are found to perform well in peel and tack tests due to their ability to flow (and increased wettability) but they perform poorly in shear, and thus a higher molecular weight can lead to an optimal adhesive response [131]. Another factor which has been investigated extensively is the inclusion of tackifying resins and fillers [125, 134–137]. As with the molecular weight, the tack response is found to increase initially with increased concentration of tackifier and reaches an optimal response before decreasing with further addition of tackifier.

The extent of crosslinking in amorphous polymer films is yet another factor which plays an important role in PSA performance. Previous work has shown that an optimal degree of crosslinking in terms of the tack response exists just above the gel point [138], however the extent to which crosslinking affects mechanical properties such as the elastic modulus and the total work required to debond an adhesive film, as well as the molecular mechanisms which play a large role in adhesive performance have not yet been extensively studied.

Simple coarse-grained polymer models have proven extremely useful in elucidating polymer properties and behaviors at scales which currently are not accessible with experimental techniques. Such models have successfully been used to investigate a broad range of polymer systems and properties including basic dynamics and structure of amorphous polymers [139, 140], adhesion of end-tethered polymers [141, 142], and properties of highly crosslinked network polymer adhesives [143–146]. Similar models have also been used to demonstrate the importance of coupled effects of polymer-polymer and polymer-surface interaction in determining the elastic and adhesive properties of polymer films [147, 148]. In this section, a simple coarse-grained polymer model is used to directly investigate the extent to which crosslinking affects the adhesive response of amorphous polymer adhesives. Both qualitative and quantitative insights into how crosslinking affects adhesive response are provided and molecular scale mechanisms which can be harnessed to tune and ultimately optimize the adhesive performance are examined.

5.1.2 Methods

A simple bead-spring-like polymer model is used based on that of Kremer and Grest [139,140]. The polymer chains are treated as spherical beads of mass m which interact via a total energy function described by the sum of non-bonded, bonded, and angle interactions:

$$E = E_{NB} + E_b + E_\theta = \sum_{Pairs} \varphi_{LJ}(r_{ij}) + \sum_{Bonds} \varphi_b(r_{ij}) + \sum_{Angles} \varphi_\theta(\theta_{ijk}) \tag{5.1}$$

$$\varphi_{LJ}(r_{ij}) = 4\varepsilon \left[\left(\frac{\sigma}{r_{ij}} \right)^{12} - \left(\frac{\sigma}{r_{ij}} \right)^{6} \right] \quad r_{ij} < r_c \tag{5.2}$$

$$\varphi_b(r_{ij}) = -0.5 K_b R_0^2 \ln \left[1 - \left(\frac{r_{ij}}{R_0} \right)^2 \right] + \varphi_{LJ}(r_{ij}) \tag{5.3}$$

$$\varphi(\theta_{ijk}) = K_\theta \left(1 + \cos\theta\right) \tag{5.4}$$

All parameters used in this work are described in reduced Lennard-Jones units;

all distances and energies are defined in terms of the parameters σ and ε, respectively, and all other quantities are derived from those parameters. Here the cutoff distance $r_c = 2.5\sigma$, the bond stiffness $K_b = 30\varepsilon/\sigma^2$, the maximum bond length $R_0 = 1.3\sigma$, and the bending stiffness $K_\theta = 1.5\varepsilon$. The model is implemented in the LAMMPS simulation package [110–112, 149]; visualizations are performed with VMD [79].

Structure Generation

Amorphous polymer melt structures are created by following a simple three-step process shown schematically in Figure 5-1. First, the initial geometry is created by defining the simulation box and building independent random walk chains inside the box. The random walk chains are created in a stepwise manner; the position of the first bead (monomer unit) is chosen randomly, and then subsequent beads are placed by randomly picking a point on the surface of a sphere [150] of radius r_0 (where r_0 is the equilibrium bond length between bonds or monomer units) and placing the next bead at that point. Each generated structure comprises 1000 chains with 100 beads per chain.

The second step of the process is a relaxation of the overlapped structure; this step is implemented with a simple NVE ensemble. All MD simulations are run with the LAMMPS simulation package [110–112, 149] with a time step of $\Delta\tau = 0.006\tau$ where $\tau = \sigma(m/\varepsilon)^{1/2}$. During the relaxation process, the non-bonded (Lennard-Jones) interactions are replaced by a soft repulsive potential of the form

$$\varphi^*(r_{ij}) = A\left[1 + \cos\left(\frac{\pi r_{ij}}{r_c}\right)\right] \quad r_{ij} < r_c \tag{5.5}$$

where $r_c = 3\sigma$. Over the course of the relaxation phase, the value of A (the strength of the repulsive potential) is slowly ramped from zero to 15ε over 2×10^5 steps, and then the value is held at 15ε for an additional 3×10^5 steps. The final structure after relaxation comprises a dilute solution of extended chains as shown in Figure 5-1(a)(ii).

The final step for creating the polymer melt geometries is equilibrating the relaxed structure with isothermal-isobaric (NPT) MD to form a dense amorphous geometry.

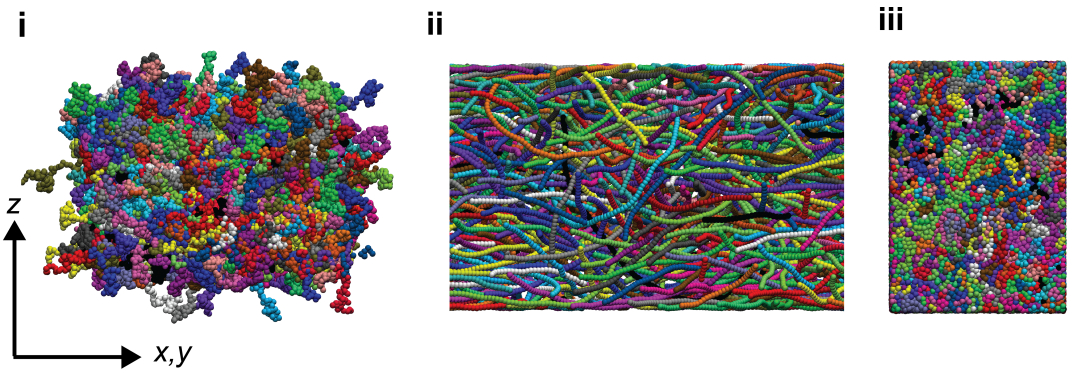

(a)

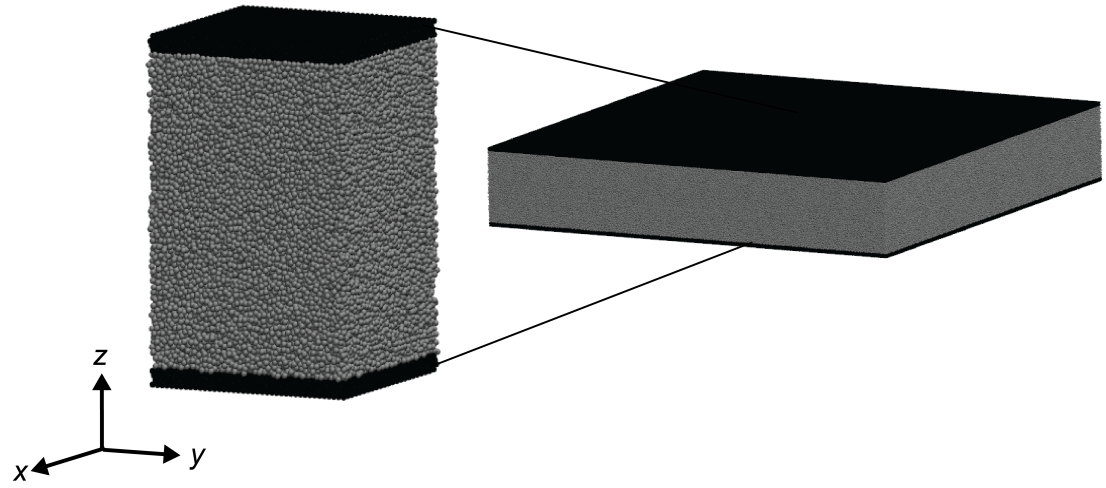

(b)

Figure 5-1: Representative snapshots from the three phases of structure preparation. The different colors indicate beads belonging to different polymer chains. (a)(i) shows the initial random walk structure in which chains are highly overlapped. (a)(ii) shows the structure following the relaxation process. This structure is a dilute collection of mostly extended chains. (a)(iii) shows the final structure following the equilibration and crosslinking steps. The structure becomes much more dense and the chains are highly entangled. A single unit cell with adhesive walls is shown in (b) as well as a 9×9 array of unit cells which demonstrates the thin film geometry achieved with the periodic boundary conditions.

The equilibration consists of three steps: initial equilibration at high temperature to promote dynamic mixing of the chains and to remove any structural artifacts introduced through the initial structure definition and relaxation process, low temperature equilibration and the formation of crosslinks, and final equilibration of the crosslinked structure. The high temperature equilibration is performed at at temperature of $T = 2.5\varepsilon/k_B$ for 7×10^5 steps, followed by a lower temperature run at $T = 1.0\varepsilon/k_B$ for 8×10^5 steps. Following the crosslinking step (described below), a final equilibration run is performed at $T = 1.0\varepsilon/k_B$ for 4.9×10^5 steps.

Over the course of the structure preparation process, a film-like geometry is enforced by imposing periodic boundary conditions in the $x-$ and $y-$directions and fixed boundary conditions in the $z-$direction as shown in Figure 5-1(b). For the relaxation and initial equilibration steps, simple reflecting walls are used to confine the chains in the $z-$direction; fore the subsequent equilibration steps, the reflecting walls are replaced by walls which interact with the polymer film through a 9-3 Lennard-Jones potential:

$$\varphi_{wall} = \varepsilon_{wall}\left[\frac{2}{15}\left(\frac{\sigma_{wall}}{r}\right)^9 - \left(\frac{\sigma_{wall}}{r}\right)^3\right] \quad r < r_c^{wall} \tag{5.6}$$

with $\varepsilon_{wall} = \varepsilon$, $\sigma_{wall} = 2\sigma$, and $r_c^{wall} = 6\sigma$. This wall potential approximates the interaction with the explicit walls used to investigate the adhesive performance (described below) and the parameters are chosen such that the polymer-polymer and polymer-wall interactions are similar in strength. All of the wall potentials are positioned such that the total thickness of the structure is maintained at $\sim 60\sigma$. During the equilibration phase, a zero pressure boundary condition is maintained in the $x-$ and $y-$directions to allow the structure to achieve a dense, stress-free configuration.

Polymer Crosslinks

Crosslinking is enabled in these structures via the incorporation of three distinct bead types during the generation of the initial structure. Beads designated as "type 1" are not allowed to form crosslinks, whereas those designated as "type 2" are able to form

crosslinks. Once a crosslink is formed, the two beads that comprise the new bond are changed to "type 3". Aside from the ability to form crosslinks, the three bead types are identical. When creating the initial random walk structure, each bead is assigned as type 1 or type 2 with a prescribed probability ranging from 0 (no crosslinkable beads) to 0.1, and the restriction that type 2 beads are not allowed to be adjacent on the same chain in order to prevent forming a crosslink bond to beads which are already bonded. During the structure equilibration process, a reaction step is implemented in which two type 2 beads within $1.1r_0$ are allowed to form a crosslink; the final crosslink density can be controlled by adjusting the initial concentration of type 2 beads as well as by modulating the duration of the reaction step. In this work, 1×10^4 steps are allowed for the reaction step for all systems considered. All crosslinks are described by the same parameters as bonds within chains and are thus considered covalent crosslinks.

Mechanical Characterization

A simple tack test is performed to characterize the adhesive response of the crosslinked amorphous polymer structures; the tack test setup is shown schematically in Figure 5-2. This test is performed with NVT MD with periodic boundary conditions in the polymer film plane. The Lennard-Jones wall potentials (equation 5.6) used in the equilibration process are replaced by three layers of beads arranged in an FCC lattice with the (1 1 1) face oriented along the $z-$direction with a lattice constant of 1.204σ; similar setups have been successfully used to asses adhesive performance in pervious work [146]. These wall beads interact with the polymer beads via Equation 5.2 with $\varepsilon_{wall} = \varepsilon$, $\sigma_{wall} = 2\sigma$, and $r_c^{wall} = 6\sigma$, but do not interact with each other. The walls are treated as independent rigid bodies; the bottom wall is always held fixed and the top wall is allowed to displace along the $z-$direction but not allowed to rotate. Before performing the tack test, an initial compression step is carried out in which a constant stress of $-0.2\varepsilon/\sigma^3$ is applied to the top wall for 2.5×10^5 steps to promote adhesion between the polymer film and the walls. This compression step also mimics the process by which PSAs are applied to surfaces in which a small amount of pressure

is applied to achieve the adhesive bond.

The tack test is then performed by displacing the upper wall at a constant velocity of $= 0.002\sigma/\tau$. It is noted that the strain rate can be an important factor in polymer film mechanics, but a single strain rate is used in the present work for all simulations to isolate the effects of crosslinking in determining the mechanical response. Adhesive performance is assessed through the stress-strain response, including changes in the elastic modulus and the plateau stress. Importantly, the toughness modulus is calculated from the area under the stress-strain curve for each case to provide a measure of the energy dissipated per unit volume during the debonding process. A total of three tack test simulations are performed for each crosslink density to account for stochastic effects; and additional 1×10^4 equilibration steps are performed prior to the inclusion of the adhesive walls in order to sample a new configuration. The results for the adhesive performance are then obtained by averaging over the results from the three runs; error bars indicate the minimum and maximum values observed.

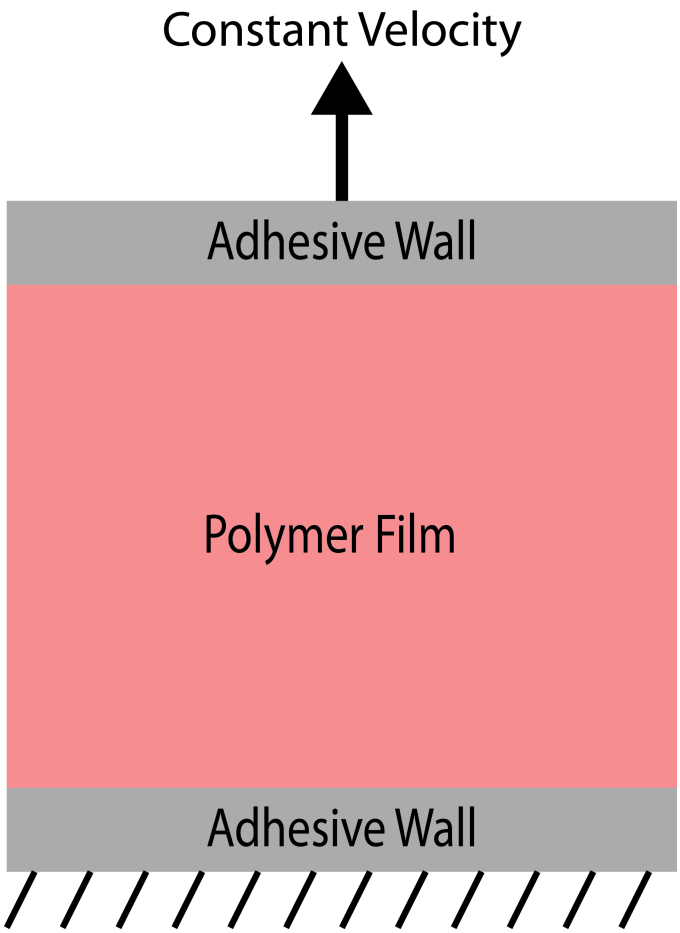

Figure 5-2: A schematic of the tack test setup used to characterize the adhesive response of the amorphous polymer films. Two adhesive walls are introduced to the system which interact with the polymer film via a simple Lennard-Jones interaction. The bottom wall is fixed, while the top wall is displaced at a constant velocity in the direction perpendicular to the film plane.

5.1.3 Results and Discussion

Seven crosslink densities ranging from 0 to 5.81 % are investigated. Figure 5-3 shows the final crosslink density in the amorphous structures as a function of the initial concentration of crosslinkable beads; here the crosslink density is defined as the fraction of beads involved in crosslinks (type 3):

$$\rho_{XL} = \frac{N_3}{N_{Total}} = \frac{2N_{XL}}{N_{Total}} \tag{5.7}$$

The factor of two arises since two beads participate in each crosslink. We note that these crosslink densities are not unique; the final value depends on the number of steps allowed for the reaction phase. In the present work the number of steps allowed for the reaction is limited to 1×10^4 in order to sample a representative range of crosslink densities.

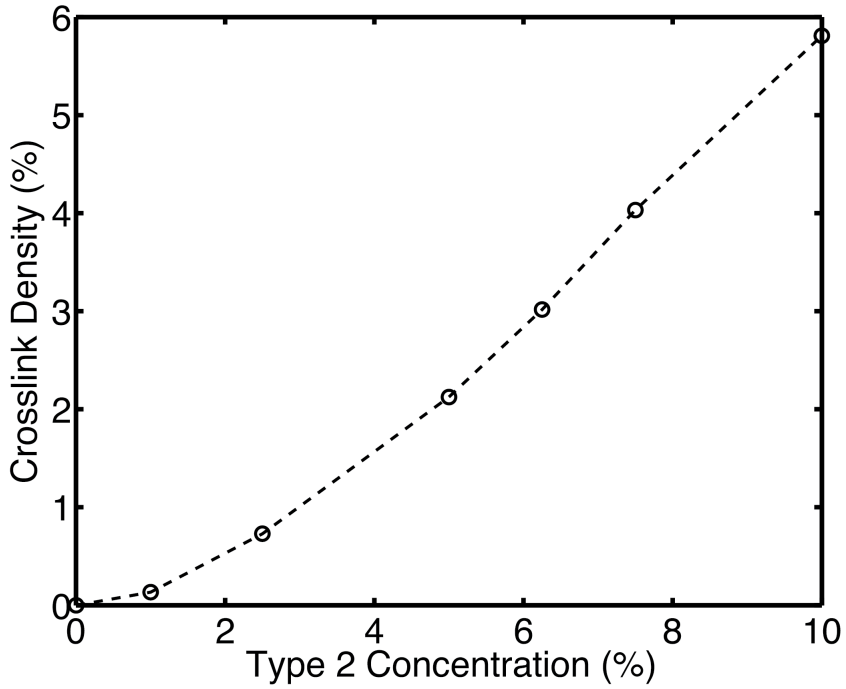

Figure 5-3: Variation of the final crosslink density with the concentration of crosslinkable (type 2) beads. Seven crosslink densities are studied ranging from 0 to 5.81 %.

The stress-strain responses of the seven structures investigated are shown in Figure 5-4(a); the inset shows the small strain response. All of the structures initially feature a similar elastic response followed by a sudden drop in the stress which corresponds to the initial formation of a defect (void) in the material. These results show excellent qualitative agreement experimental results for PSA tack tests in which an initial peak in the force-displacement response is followed by a drop in the force to a plateau value which extends to larger displacements 10-12, 14, 15, 25. The specific responses in the elastic regime are plotted in Figure 5-4(b) with all values normalized by the response of the non-crosslinked structure. As expected, the elastic modulus increases with increasing crosslink density due to the extra connectivity in the network,

however the increase is modest —the highest crosslink density studied only resulted in an 11% increase in the elastic modulus. A similar trend is observed in the value of the peak stress achieved in the elastic regime. For most of the structures considered, crosslinking results in an increase in the peak stress compared to the non-crosslinked structure, but again the effect is modest indicating that crosslinking alone is not an optimal strategy for enhancing the mechanical response of amorphous polymers in the small strain regime.

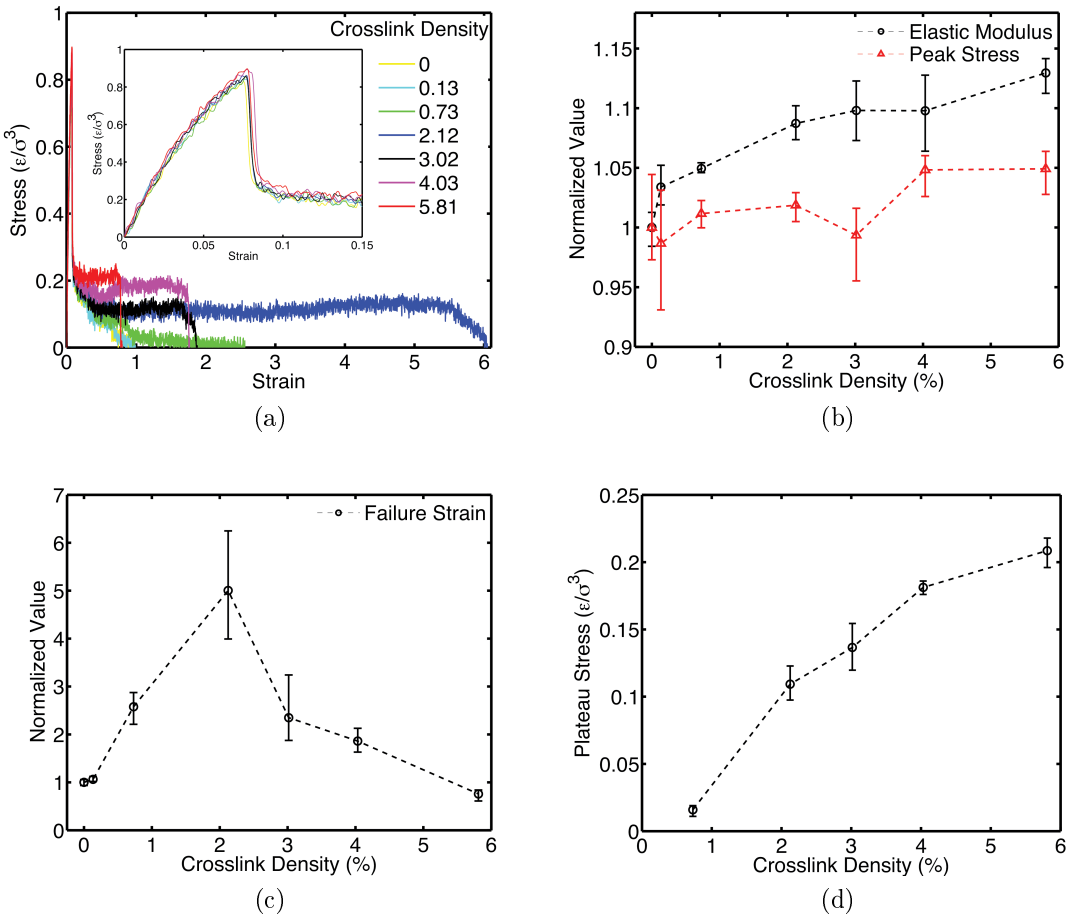

Figure 5-4: (a) shows the stress-strain response of the seven crosslinked structures investigated; the inset plots the small strain (elastic regime) response. (b) shows the variation of the elastic modulus and peak stress as a function of crosslink density. (c) shows the strain-to-failure with increasing crosslink density. (d) plots the plateua stress versus the crosslink density. The lowest two crosslink densities are excluded since those structures failed before supporting any steady applied stress. The mean values from three tack test simulations are plotted with error bars indicating the minimum and maximum observed values.

In contrast, crosslinking has a dramatic effect on the stress-strain response in the post-elastic regime. For the lowest two crosslink densities (0% and 0.13%), the response is quite similar with a gradual decrease in the stress until failure. Once the crosslink density is increased to 0.73%, however, the structure is able to sustain a non-zero stress (the plateau stress) to a much higher strain before failing. As the crosslink density is increased to 2.12%, a very large change in the response is observed as the additional connectivity allows for the polymer to achieve a much higher strain before failing, however further increases in the crosslink density cause the strain to failure to decrease as the additional connectivity causes the structure to respond in a more elastic rather than viscous manner (Figure 5-4(c)). Additionally, the plateau stress which is plotted in Figure 5-4(d) for the five structures which are able to sustain a non-zero stress, is found to increase significantly with increasing crosslink density; it increases 13-fold over the small range of crosslink densities investigated. This result clearly demonstrates how sensitive adhesive properties can be to small changes in crosslink density. In particular the plateau stress is an important indicator of the load magnitudes that an adhesive is able to sustain during typical usage.

Figure 5-5 shows representative simulation snapshots from the post-elastic regime. The snapshots demonstrate the key mechanisms that give rise to the dramatic variation in mechanical response. Figure 5-5(a) shows the fibril structures formed during the deformation process. With higher crosslink densities, the stable fibril grows in diameter due to the additional connectivity, and more importantly, it is clear from the relative amount of the material involved in the fibril that crosslinking results in a larger fraction of the polymer material being involved in the deformation response. We note that the relatively small system size use of periodic boundary conditions introduces a finite size effect into the systems which suppresses the typical crazing geometry in a single periodic cell. The two lowest crosslink density structures exhibit large volumes in which much of the polymer is not deformed, and only the small number of chains in the fibril participate in the deformation which accounts for the large global strain; this indicates that in these structures, the material is not utilized efficiently. The two high crosslink density structures, in contrast, exhibit deforma-

tion along most of the thickness of the sample, and thus the material is much more efficiently utilized. Figure 5-5(b) shows the same structures right before failure. In the structures with lower crosslink densities, the fibrils eventually neck down to a single chain, whereas with higher crosslink densities, a larger fraction of the material is extended and the deformed structure develops a more tortuous geometry with numerous smaller scale features. Furthermore, the cross-sectional area of the fibrils tends to increase with increasing crosslink density; this is likely the mechanism which results in the increase in the plateau stress.

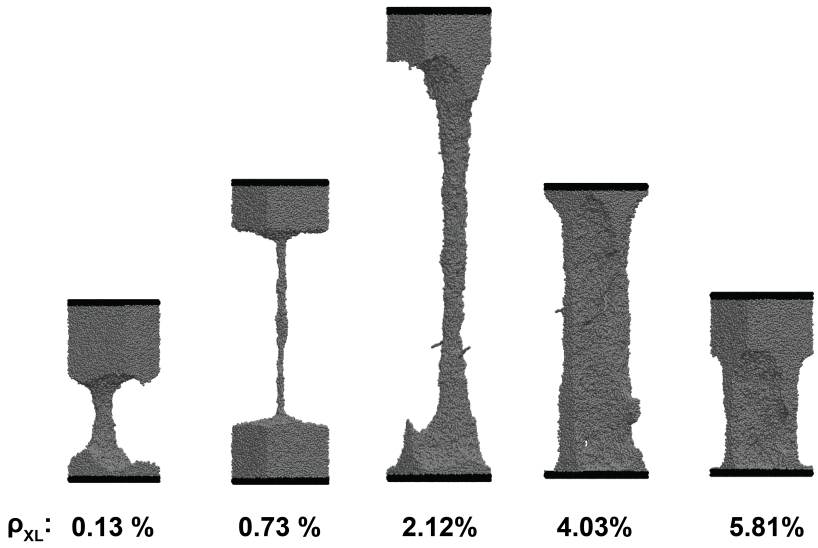

(a)

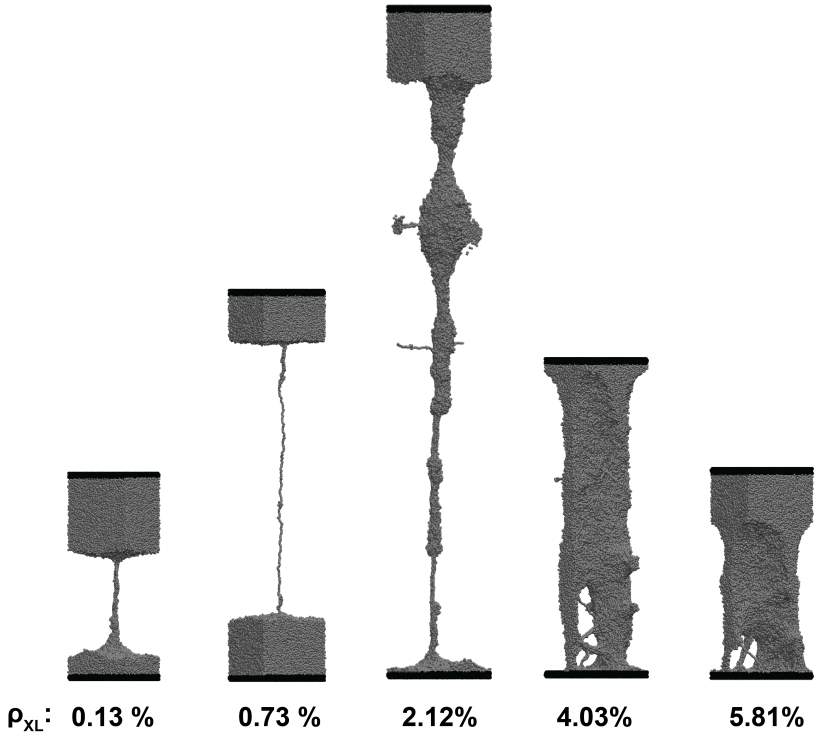

(b)

Figure 5-5: Representative simulation snapshots from the post-elastic regime. The crosslink density is shown under each snapshot. Representative fibril structures are shown in (a); various degrees of deformation are shown to highlight the diversity of the deformed geometries. Snapshots of the structures just prior to failure are shown in (b).

The failure response of the adhesives is shown in Figure5-6; a clear transition is observed from a cohesive failure mode in which failure occurs within the polymer material to an adhesive failure mode in which failure occurs by debonding of all of the polymer material from one of the adhesive walls. We note that the relatively smooth failure surfaces result from the fact that the polymers are tested above their glass transition temperature and thus the extended material seen in Figure 5-5 snaps back into the remaining material as the strain energy is relieved. It is interesting to note that even though the structure with $\rho_{XL} = 2.12\%$ displays an impressive deformed structure in which all of the material appears to be effectively utilized, it still fails cohesively as a small amount of material is left on the bottom wall after failure.

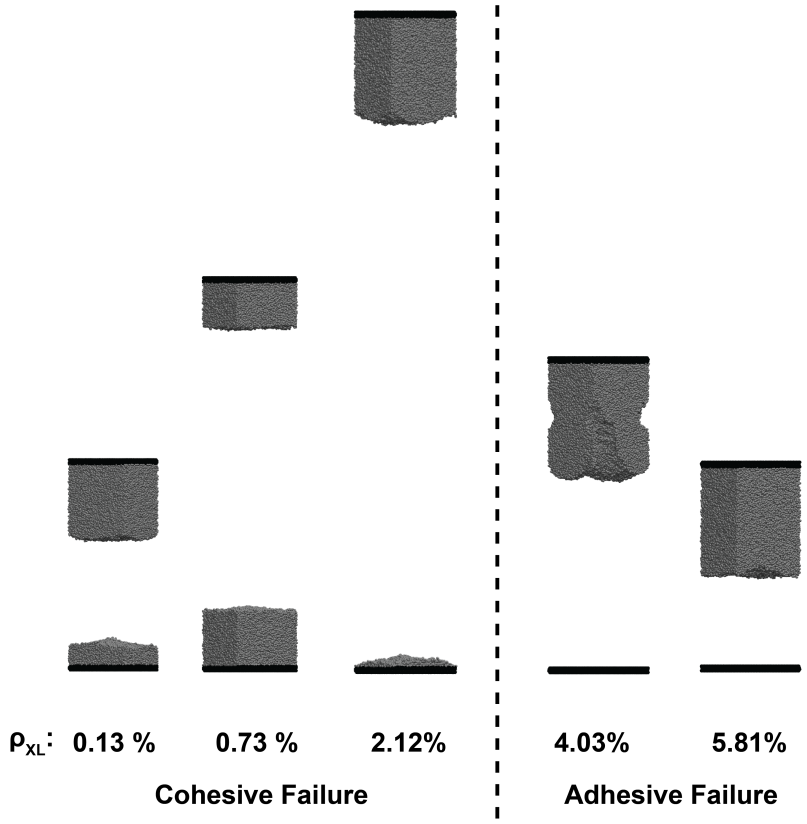

Figure 5-6: Representative simulation snapshots after failure. In each case the structure relaxes quickly after failure. Lower crosslink densities result in cohesive failure, while structures with larger crosslink densities fail adhesively. Adhesive failure is typically desirable as PSAs are often used in reusable adhesive applications.

The toughness modulus (normalized by the non-crosslinked response) is shown

in Figure 5-7(a). The toughness modulus is a measure of the energy dissipated per unit volume during deformation and thus here it demonstrates changes in the work required to debond the adhesive. We observe a very large range of responses, mostly in line with the failure strain response; an optimal response is reached at a modest degree of crosslinking, but the performance decreases with further increases in the crosslink density. We also note the importance of the interplay between the failure strain and the plateau stress in determining the toughness modulus as a function of crosslink density. Although the failure strain increases rapidly at low crosslink densities, the very small (or nonexistent) plateau stresses at these crosslink densities prevent an appreciable increase in the toughness modulus. Thus the toughness modulus increases more slowly than the failure strain for small amounts of crosslinking. In contrast, at higher crosslink densities where the failure strain drops off rapidly, the toughness modulus displays a less severe decline due to the increasing plateau stress.

Figure 5-7(b) shows schematics of competing molecular scale mechanisms which explain the observed peak in the toughness modulus as well as the transition from cohesive to adhesive failure. For low crosslink densities (Figure 5-7(b)(i)), crosslinks have the effect of increasing the average chain length and increasing the overall deformability of the crosslinked structure; the crosslinks inhibit the chain sliding mechanism which cause the non-crosslinked structures to fail by breaking the non-bonded interactions during the chain sliding at very low strains. As the crosslink density is increased further (Figure 5-7(b)(ii)), the crosslinks begin to reduce the deformability as an elastic network forms with short chains between connected nodes. Although the strength and stiffness of such a structure can be higher as adding crosslinks helps to stabilize the molecular conformation, the structure fails adhesively at the interface before a significant amount of energy can be dissipated in debonding inside the structure. This is made clear by the drop in the toughness modulus as the crosslink density is increased above the optimal value. The increased connectivity causes an increase in the plateau stress which would typically increase the toughness modulus, but the drastically decreased overall extensibility becomes the important factor in determining the amount of energy that the polymer can dissipate before failing at the

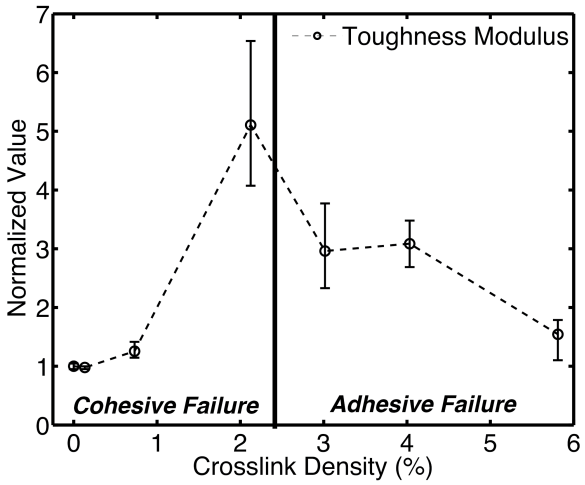

(a)

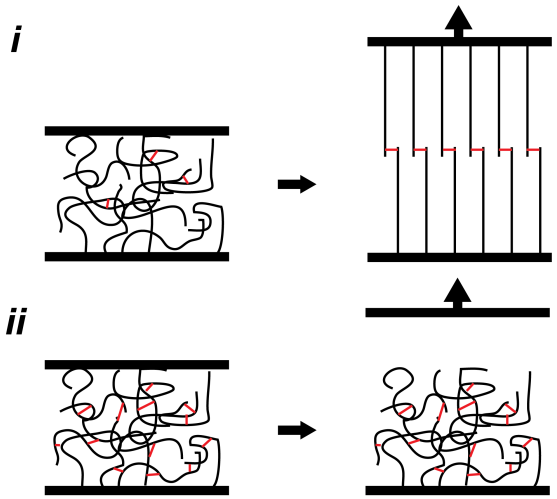

(b)

Figure 5-7: (a) plots the toughness modulus vs. crosslink density normalized by the value from the uncrosslinked structure; the mean result from three tack test simulations is shown with error bars indicating the minimum and maximum values observed. Increasing the crosslink density causes an initial increase in the toughness modulus due to increases in the plateau stress and strain-to-failure. However, further increases cause a drop in the toughness modulus due to the sharp decrese in the strain-to-failure. A schematic of the competing deformation mechanisms responsible for the observed response is shown in (b). For low crosslink densities (i), the chains are able to extend and the crosslinks effectively increase the average chain length and in turn increase the overall deformability. For larger crosslink densities (ii), the deformability decreases and the structure transitions to an adhesive failure mode.

interface.

Another mechanism that contributes to the transition between cohesive and adhesive failures is that for low crosslink densities, the polymer chains within the structure have weak interactions and behave more independently during failure, as a single defect or crack does not significantly affect the extensibility of the rest piece of material. For high crosslink densities, however, the interactions between polymer chains become much stronger, making the material less flaw tolerant. Thus a single defect or crack can cause stress concentration and can propagate by breaking the interfacial interactions, as illustrated in Figures 5-5(b) and 5-7(b), dissipating less energy before failure.

5.1.4 Conclusions

Molecular dynamics simulations were performed on simple coarse-grained polymer systems to directly investigate the effects that crosslinking has on the adhesive performance of amorphous polymer adhesives. Many properties were found to be highly sensitive to crosslink density, most notably the plateau stress, strain to failure and toughness modulus, all of which are important parameters to consider in the design of new adhesive materials which seek to maximize mechanical performance as well as to have predictable mechanical behavior before failure. The results demonstrate that the mechanical response of amorphous polymer adhesives can be systematically tuned by simply adjusting the crosslink density, and importantly, that optimal performance is achieved at an intermediate degree of crosslinking which coincides with the transition from cohesive to adhesive failure. This study also makes more clear the mechanisms which contribute to these two different failure modes.

The results demonstrate good qualitative agreement with deformation behavior of PSAs observed in experiments. The model described here is simple and general and can be extended to include the specific physical parameters of many polymer adhesives. Scaling of the adhesive properties with physical crosslink density could be investigated further for specific polymer systems of interest to provide further validation. Furthermore, this model is capable of providing insight into diverse molecular

scale mechanisms and thus it can be used to investigate many other properties which could affect adhesion including the organization of crosslink sites, dispersity of the polymer chains, the role of crosslinking in the presence of surface roughness, and the interplay between crosslinking and strain rate or temperature effects in adhesive films. Although the model is very simple, the results provide valuable insights which can guide the design of future polymer adhesive materials which optimize the adhesive response through careful engineering of crosslinks.

5.2 Extension to Amyloid-Based Adhesives

Although amyloid and amyloid-like fibrils are not amorphous polymers, the work described in this chapter is broadly relevant and aids in the understanding and design of a host of natural adhesive materials including functional amyloid-based biomaterials. Specifically, the model can be altered and parameterized to make the behavior of the polymer chains reflect the mechanical properties of amyloid and amyloid-like fibrils. More importantly, the methods for characterizing the polymer films can be used without significant modification to characterize the adhesive properties of films based on amyloid or amyloid-like fibrils (see Section 6.3).

Amyloid and amyloid-like fibrils constitute a diverse collection of materials with similar building blocks but with widely varying mechanical properties. Specifically, amyloid and amyloid-like fibrils are all based on the cross-β secondary structure motif and thus posses impressive mechanical properties, but as shown in Chapter 3, the specific mechanical response can vary greatly between specific amyloid structures. This is quite similar to the crosslinked amorphous polymer films described in this chapter which all have the same constituent polymer chains, but vary just in the degree of connectivity in the films and thus end up with a wide range of adhesive responses. The work presented in this chapter demonstrates that a simple model (in this case for polymer chains) is able to capture subtle relationships between available deformation pathways at the molecular scale and global mechanical performance. These types of relationships will be quite important to analyze when comparing amyloid and

amyloid-like fibrils and ultimately choosing structures which optimize performance in specific functional roles.

Besides the fact that the methods described in this section are broadly applicable to the field of soft matter, the insights gained from this work are also relevant to the problems addressed in this thesis. Specifically, the competition between enhanced strength and reduced deformability which ultimately results in an optimal adhesive response at an intermediate degree of crosslinking sheds light on some important competing mechanisms in amyloid-based functional materials. As shown in Chapter 3, amyloid and amyloid-like fibrils are brittle with tensile strengths that cover a wide range, and the diversity of geometries in amyloid and amyloid-like fibrils leads to very large differences in inter-fibril adhesion strength. The interplay between these properties at the mesoscale should lead to a competition between increased mechanical performance as the inter-fibril adhesion strength as increased (just as crosslinking increases the mechanical performance of the polymer films) and decreased deformability as inter-fibril sliding is inhibited and the structures transition to a more brittle failure mode. Thus, an intermediate set of fibril properties which provide a balance between inter-fibril adhesion strength and fibril tensile strength (to mitigate brittle failure) should provide an optimum in terms of the global functional response. It is noted, however, that this optimum may be different for different functional roles, and thus the amyloid or amyloid-like fibrils should be chosen or engineered appropriately for a given application.

5.3 Chapter Summary

The specific effect of crosslinking in amorphous polymer adhesives has not been studied extensively in the literature. A simple coarse-grained model was used to study this effect and examine the relationship between enhanced network strength and network deformability with increased crosslinking. Optimal adhesive performance is seen in those structures which effectively balance these effects. The results shown in this chapter are broadly relevant to the field of soft matter and provide some clear guide-

lines to aid in the design of functional amyloid-based materials including adhesive films.

Chapter 6

Mesoscale Modeling of Functional Amyloid-Based Materials

This chapter builds on the modeling efforts described in Chapters 4 and 5 to directly investigate mechanical properties of functional amyloid-based materials. A comparative analysis is performed on two distinct amyloid and amyloid-like fibrils: the Aβ (1-40) amyloid fibril and the YadA collagen binding β-helix. As demonstrated in Chapter 3, these two structures exhibit very different mechanical responses and thus a comparison of the behavior of large scale structures comprising these two fibrils can elucidate fundamental features which enhance the performance of functional amyloid-based materials.

First, the specific parameterization of the coarse-grained model for the two structures will be discussed. Next, a continuation of the preliminary coarse grained modeling discussed in Appendix A is performed to directly examine the properties of these structures in a nanowire-like geometry. Finally, an extension of the work described in Chapter 5 is be performed in order to directly investigate the performance of films based on two amyloid and amyloid-like fibrils in adhesive roles and to provide some basic insights into features of amyloid or amyloid-like materials which enhance and ultimately optimize adhesive performance.

6.1 Model Parameters

The two amyloid and amyloid-like fibrils investigated in this chapter are the Aβ (1-40) amyloid fibril and the YadA collagen binding β-helix. These two structures are chosen since they are qualitatively very disparate in their geometries and mechanical response. Aside from the difference in connectivity discussed in Section 3.1 (stacked vs. helical), the physical sizes of the two protein fibrils are quite different. More importantly, they feature a large difference in the *relative* energy scales of the tensile response versus the inter-fibril adhesion strength. As discussed in Section 3.1, these two structures require a similar amount of work to deform (and fail) in tension. However, as discussed in Section 3.3, the energy required for shear deformation is quite different between the two structures. Thus by comparing these structures, the effect of the relative strengths of the intra–and inter–fibril interactions can be directly investigated. The differences in these two structures are captured in the coarse-grained model via the specific parameters used to describe the behavior of the respective fibrils. The coarse-grained model parameters are summarized in Table 6.1.

Table 6.1: Summary of the parameters used for the coarse-grained model of the Aβ (1-40) amyloid fibril and the YadA collagen binding β-helix

Parameter		Units	Aβ (1-40)	YadA β-helix
Bead Mass	m	g mol^{-1}	10107	1256
Equilibrium bead spacing	r_0	Å	14.4	14.4
Bond Energy Parameter	D	kcal mol^{-1}	48.1	23.1
Bond Shape Parameter	α	Å^{-1}	0.9	0.55
Bond Shift Parameter	δ	kcal mol^{-1}	0.9	0.5
Bending Stiffness	K_{bend}	kcal mol^{-1}	1243	322
Equilibrium angle	θ_0	Deg	180	180
LJ energy parameter	ε	kcal mol^{-1}	120.9	6.2
LJ distance parameter	σ	Å	25.0	18.0

These parameters highlight the differences between the two fibrils: the Aβ structure features much more massive beads, and the spatial extent of the beads (represented by σ via Equation 4.8) is somewhat larger as well, corresponding to a larger cross-sectional area. More importantly, the large difference in the values for the bond

and LJ energy parameters captures the difference in the relative strength of the intra- and inter-fibril interactions.

6.2 Amyloid Nanowires Revisited

The preliminary coarse-grained modeling of amyloid "nanowire" structures discussed in Appendix A provides some basic insights into the effects of varying the properties of the constituent fibrils on the overall mechanics of larger scale amyloid-based structures. However, the model used in that work fails to capture some of the important deformation behavior of the individual fibrils. This section describes an extension of that work in which the same nanowire-like geometries are investigated but using the new coarse-grained model developed in this thesis and with the model parameters discussed above. The structures are generated via the same method as used in the earlier study, and the boundary conditions are applied identically; see Section A.1.2 for details. For each of the two amyloid fibrils, three independent nanowire structures are generated and tested, and the mean response is calculated by averaging the results of the three simulations.

6.2.1 Results and Discussion

The equilibrated nanowire structures comprising the two amyloid and amyloid-like fibrils reveal some interesting behaviors that result from the different intrinsic fibril properties. Figure 6-1 shows representative equilibrated structures; the structure based on the Aβ fibrils (Figure 6-1(a)) features many fractured fibrils, while the structure based on the YadA fibrils (Figure 6-1(b)) does not show any. On average, in the Aβ-based structure, 2% of the initial bonds in the structure broke during the equilibration process, but in contrast no bonds broke in any of the YadA fibril structures during equilibration. Clearly, the much stronger inter-fibril interactions in the Aβ structure prevent relaxation via inter-fibril sliding, and thus tensile failure is the favored deformation mechanism to alleviate residual stresses generated during the structure creation process. The YadA fibrils, with their much weaker inter-fibril

interactions, do allow for relaxation via inter-fibril sliding, and thus no tensile failure is observed during equilibration, and the relaxed structure is much more ordered.

(a)

(b)

Figure 6-1: Equilibrated nanowire structures comprising (a) Aβ (1-40) amyloid fibrils and (b) YadA collagen binding β-helix fibrils. The Aβ fibrils have a strong inter-fibril interaction and thus the equilibration process results in siginificant tensile failure of individual fibrils, whereas the YadA fibrils, with a relatively weak inter-fibril interaction, are able to equilibrate and relax via inter-fibril sliding. Color indicates beads belonging to different fibrils (based on intial structure definition).

Figure 6-2 shows the stress-strain plots for the nanowire structures comprising the two protein fibrils. A very large difference in the performance of the two constituent fibrils is apparent; the Aβ (1-40) amyloid fibril far outperforms the YadA β-helix in terms of the ultimate tensile strength and strain to failure (and by extension the toughness modulus which provides a measure of the overall robustness of the structures). This is in stark contrast to the atomistic scale tensile test results (Section 3.1) in which the YadA fibril was found to outperform the Aβ fibril.

The mechanical properties of the two nanowire structures are summarized in Table 6.2. In general, the nanowire structures exhibit mechanical properties approxi-

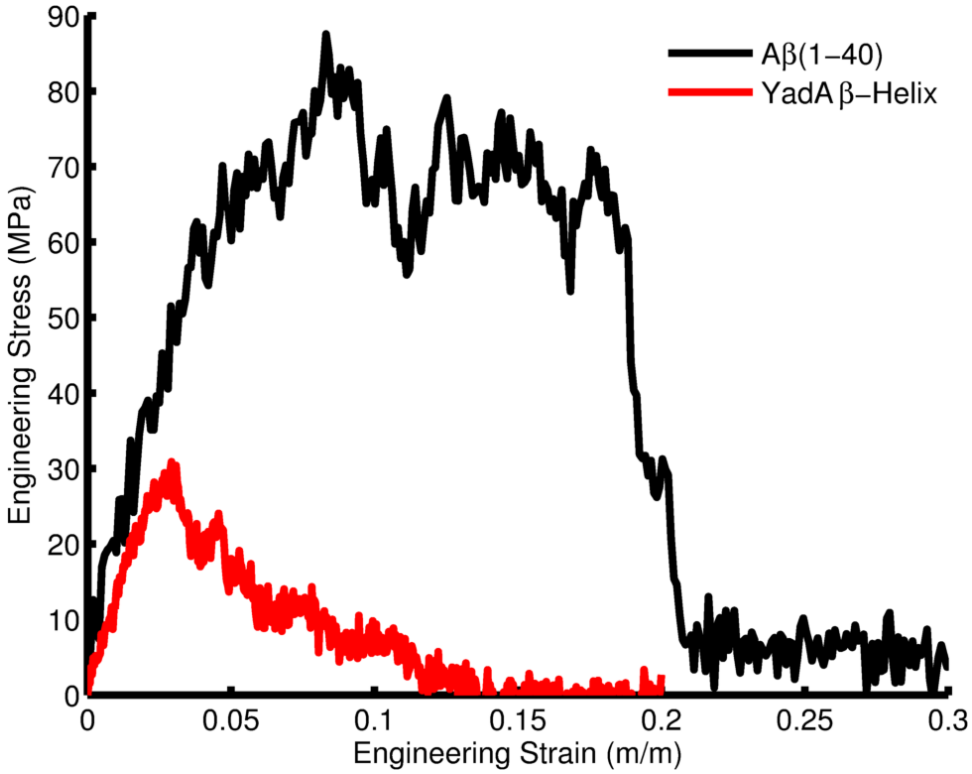

Figure 6-2: Stress-strain plots for the nanowire structures investigated in this study. The structures comprising the Aβ fibrils far outperform the YadA fibril based structures in both ultimate tensile strength and strain to failure.

mately one order of magnitude smaller than the properties of the constituent fibrils as reported in Section 3.1. This drop in mechanical performance can be attributed to the existence of deformation mechanisms at the mesoscale (sliding, unfolding of bent regions, etc.) which are not available at the single fibril scale. Thus the strength and stiffness achieved through the presence of the cross-β structure is mitigated by the weaker inter-fibril interactions. These deformation mechanisms, however, also allow the Aβ structure to achieve a failure strain of nearly twice the value achieved in the atomistic structure (in this context, the failure strain for the atomistic structures is defined by the onset of the low stress unfolding regime after which useful mechanical properties are lost (see Section 3.1)). Thus, although the strength and stiffness are reduced, the inter-fibril deformation mechanisms allow for the robustness of the assemblies to exceed that of the constituent fibrils.

Table 6.2: Summary of the mechanical properties of the amyloid-based nanowire structures calculated from this study

Property	Units	Aβ (1-40)	YadA β-helix
Young's Modulus	GPa	1.5	1.25
Ultimate Tensile Strength	MPa	87.6	30.9
Failure Strain	—	0.22	0.14
Toughness Modulus	MPa	14.0	1.6

Interestingly, the Aβ based structure also exhibits some flow-like behavior in which the stress remains constant with increasing strain, before failing abruptly, similar to brittle failure. In contrast, with the YadA β-helix fibrils, the stress continuously decays after the peak. This behavior is similar to that seen in the polymer adhesives discussed in Chapter 5 and also in the preliminary coarse-grained modeling work (Appendix A). It suggests that the stronger inter-fibril interactions in the Aβ-based structure allows for the structure to maintain its cross-sectional area during deformation and thus support a non-zero flow stress. The weaker interactions in the YadA-based structure simply result in necking down to a single fibril and the stress drops accordingly. These deformation and failure modes are illustrated in Figure 6-4.

Finally, a comparison of the evolution of broken bonds in the nanowire struc-

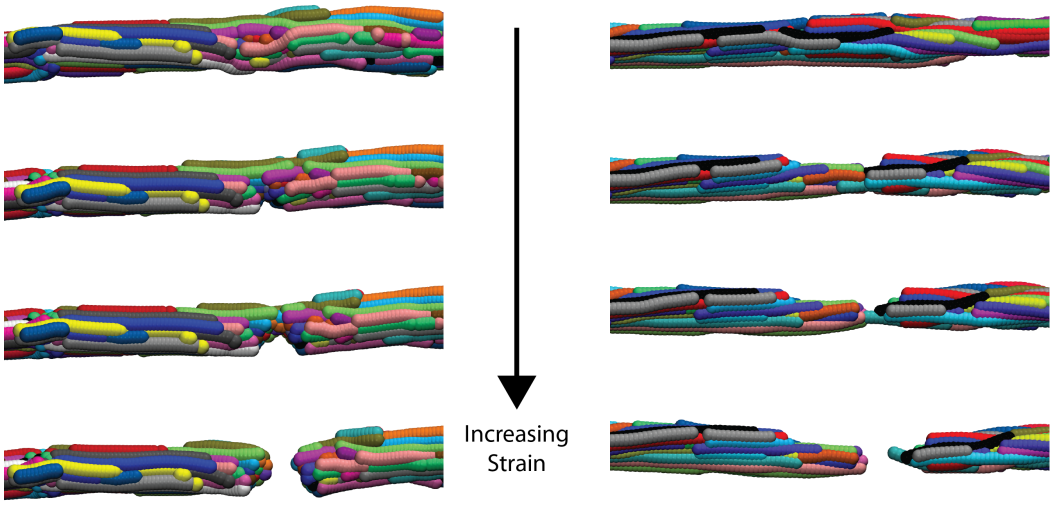

(a) (b)

Figure 6-3: Simulation snapshots illustrating the deformation and failure of nanowire structures comprising (a) Aβ (1-40) amyloid fibrils and (b) YadA collagen binding β-helix fibrils. The strong inter-fibril interactions in the Aβ fibrils result in mostly brittle failure, while the weaker interactions in the YadA fibrils result in necking before failure. Color indicates beads belonging to different fibrils (based on intial structure definition).

tures (fibril failure events) reveals some interesting behaviors as well. The nanowire comprising the Aβ fibrils (Figure 6-4(a)) exhibits bond breaking almost immediately, even in the linear (elastic) regime of the stress-strain curve. In contrast, in the YadA fibril-based structures, no bond breaking is observed until the peak in the stress-strain plot is reached, after which a relatively large number of bonds break rather quickly (Figure 6-4(b). Also interesting is that in the Aβ-based structures, the onset of the "flow" regime in the stress-strain curve is accompanied by a jump in the number of broken bonds, corresponding to the formation of a "crack-like" defect such as that seen in Figure 6-3(a). Importantly, even though the Aβ-based nanowires end up with almost twice as many broken bonds as those based on the YadA fibrils, the number of broken bonds at failure in either structure is very small, less than 1% of the total number of bonds. This again indicates that the inter-fibril interactions are the dominant interactions in determining the behavior of larger scale amyloid-based structures.

6.2.2 Conclusions

Nanowire-like geometries were created from coarse-grained representations of two amyloid and amyloid like fibrils with distinct intrinsic structural and mechanical characteristics. Tensile tests were performed on these structures to investigate the effect that the relative strength of the intra- versus the inter-fibril interactions has on the overall performance of larger scale amyloid-based structures. The two structures were found to have significant differences in their performance; the Aβ fibril with its much stronger inter-fibril interactions produced nanowire structures with superior mechanical properties. This result is somewhat surprising considering that on the single fibril scale, the YadA structure was found to outperform the Aβ fibril.

Overall, this study demonstrates that as amyloid-based materials are scaled up beyond the single fibril length scales, the mechanical response becomes dominated by the inter-fibril interactions; the intra-fibril interactions are comparatively much less impactful on the mesoscale performance. Furthermore, the drop in mechanical performance due to the presence of new deformation mechanisms at the mesoscale

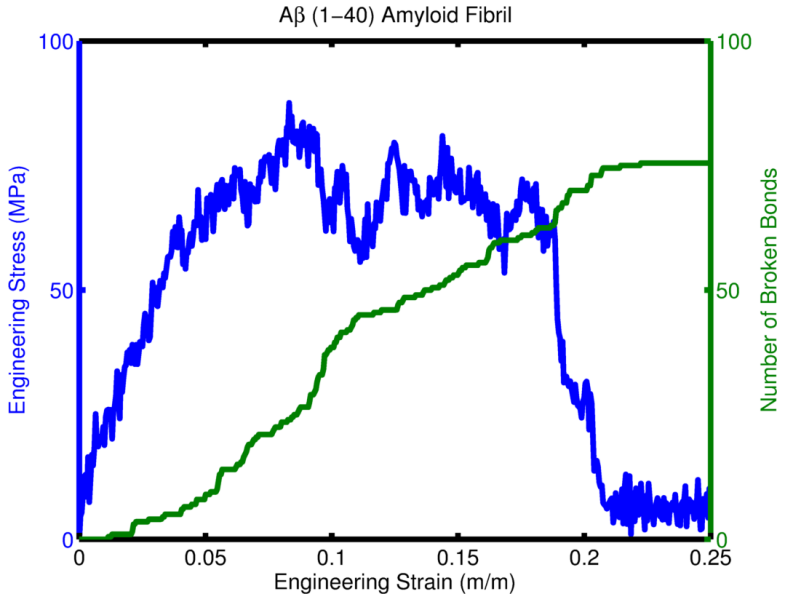

(a)

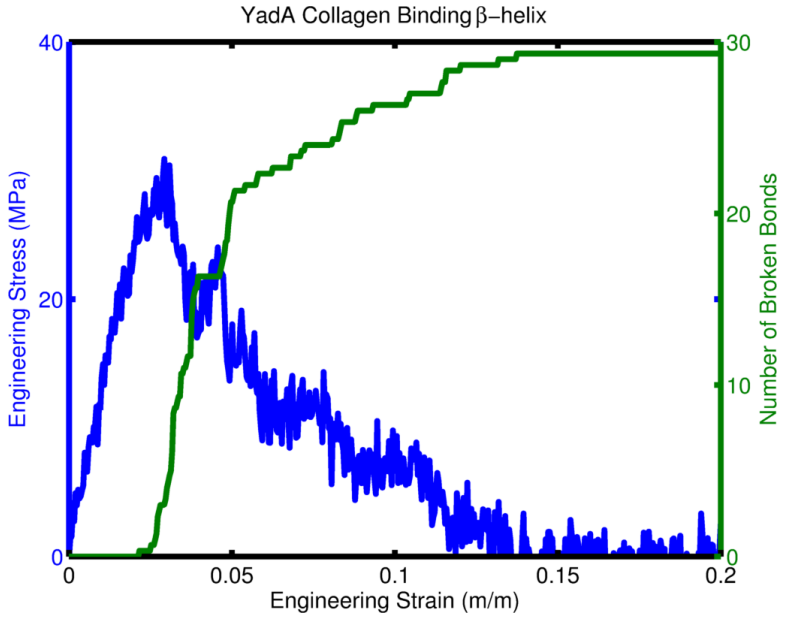

(b)

Figure 6-4: Number of bonds broken vs. strain overlayed on the stress vs. strain plots for (a) the Aβ fibrils and (b) the YadA collagen binding fibrils.

suggests that functional amyloid based materials may not in fact outperform simple polymer based materials in terms of overall mechanical performance; however, the high propensity to self assemble may still make amyloid based materials highly desirable.

The results of this study provide the initial steps towards developing materials selection guidelines for the development and design of functional amyloid-based materials. Clearly, amyloid or amyloid-like fibrils should be chosen to have strong inter-fibril interactions in order to enhance the mechanical properties of the large scale structures. However, more work must be done to identify structures with properties which *optimize* the behavior, and in particular mechanisms to tune the inter-fibril interactions must be studied in order to more fully understand how to control the mesoscale response.

6.3 Amyloid-Based Adhesives

In this section, the coarse-grained amyloid fibril model is implemented along with methods described in Chapter 5 to directly investigate the adhesive performance of amyloid-based films. As described in Sections 1.2.2 and 1.3, amyloid fibrils are utilized in nature in adhesive roles and there is much interest in developing amyloid-based engineered adhesive materials which could provide adhesion in a variety of environments. Engineered amyloid-based adhesives are still in the earliest stages of development, and thus the work described in this section can provide valuable insights which can guide the future development of amyloid-based or amyloid-inspired adhesive materials.

6.3.1 Methods

Thin film structures based on the two amyloid fibril parameterizations discussed above in Section 6.1 are generated according to the methods described in Section 4.4; each film structure comprises 100 fibrils with an initial length of 720 nm (500 beads). After equilibration, an adhesion test is carried out following the methods described in Sec-

tion 5.1.2, but with a small modification: in place of the explicitly defined wall beads, implicit walls which interact with the amyloid fibrils according to Equation 4.11. The 9-3 Lennard-Jones wall potential simulates an interaction of an infinite half-plane of particles which interact via the standard 12-6 Lennard-Jones potential. This modification simplifies the simulation setup and improves simulation performance without a loss of detail in the mechanical characterization. As with the polymer adhesive simulations, an initial compression step is performed to promote adhesion of the amyloid film to the wall potential, followed by a constant velocity tack test (as illustrated in Figure 5-2). A deformation rate of 10 m s^{-1} is used; although this is a very fast deformation rate, it allows for the large strains necessary to fully examine the adhesion behavior to be observed in a reasonable amount of simulation time. Furthermore, since the rate is consistent between structures based on the two constituent amyloid and amyloid-like fibrils, direct comparisons of their respective performance can be made, including effects and behaviors resulting from the different intra- versus inter-fibril interaction strengths.

Furthermore, for each film structure, tack test simulations are performed with four values of the wall interaction strength, ε_{wall}; the four values of ε_{wall} investigated are all greater than the inter-fibril interaction strength for the YadA collagen binding fibrils, and less than that of the Aβ fibrils. This allows for the investigation of the effects of interactions with different surfaces, and to understand the interplay between the intra- and inter-fibril interactions and the interactions with the adhesive substrate across a range of relative interaction strengths.

6.3.2 Results and Discussion

Figures 6-5(a) and 6-5(b) show the equilibrated structure of the Aβ amyloid fibril and YadA collagen binding fibril based films, respectively. Interestingly, in both cases the randomness of the starting structure (similar to that shown in Figure 4-7a is lost, and the strong inter-fibril interactions result in the formation of small bundles which then form a larger scale network. In the case of the Aβ fibrils, the stronger inter-fibril interactions cause this effect to be more prominent. Furthermore, as with the nanowire

structure, there is significant fibril fracture during the equilibration process; the fibrils utilize this deformation mechanism as a method for relieving residual stresses which build up due to the inter-fibril interactions.

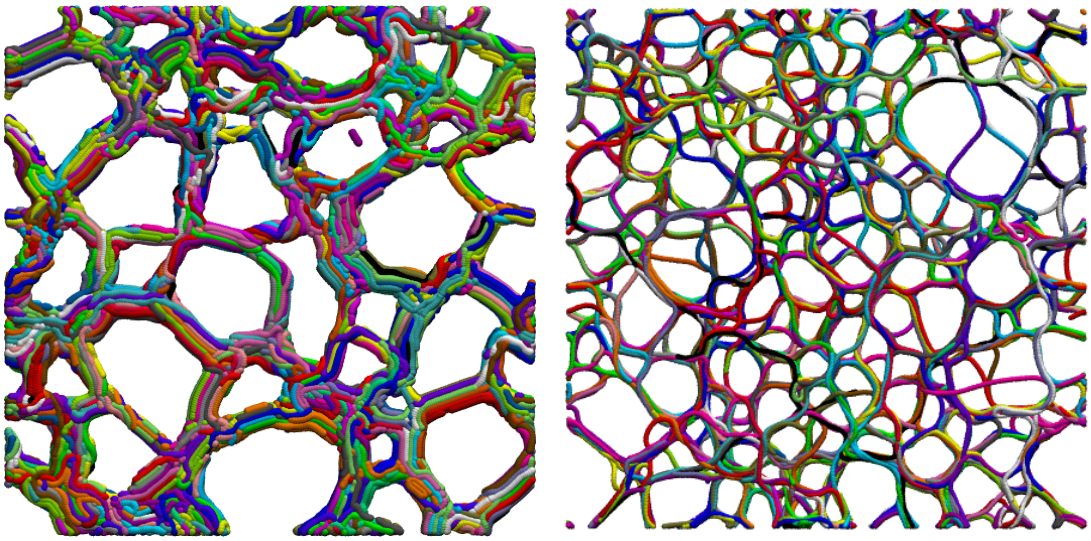

(a) (b)

Figure 6-5: Equilibrated structure of a film comprising (a) the Aβ (1-40) amyloid fibrils and (b) the YadA collagen binding fibrils. In each case, the inter-fibril interactions result in the formation of small bundles and subsequently the loss of much of the initial randomness exhbitied by the as-deposited structures.

The adhesive response of the films comprising the two structures is shown in Figure 6-6 for the four different wall adhesion energies tested. Although the YadA fibril based films slightly outperform the Aβ films in terms of the peak stress and strain to failure for the smaller two adhesion energies, the Aβ films clearly outperform the YadA structures for the larger adhesion energies. Furthermore, the results of these tack test simulations compare quite favorably to results for amorphous polymer PSAs which typically exhibit peak stresses in the range of 0.5 to 5 MPa, indicating that amyloid based films could allow for the development of a new class of strong engineered adhesives. [123, 135, 151].

As with the nanowire structures, the difference in performance stems from the drastically different inter-fibril interaction energies. The strong inter-fibril interaction in the Aβ structures allow the film to maintain cohesion during the adhesion test and

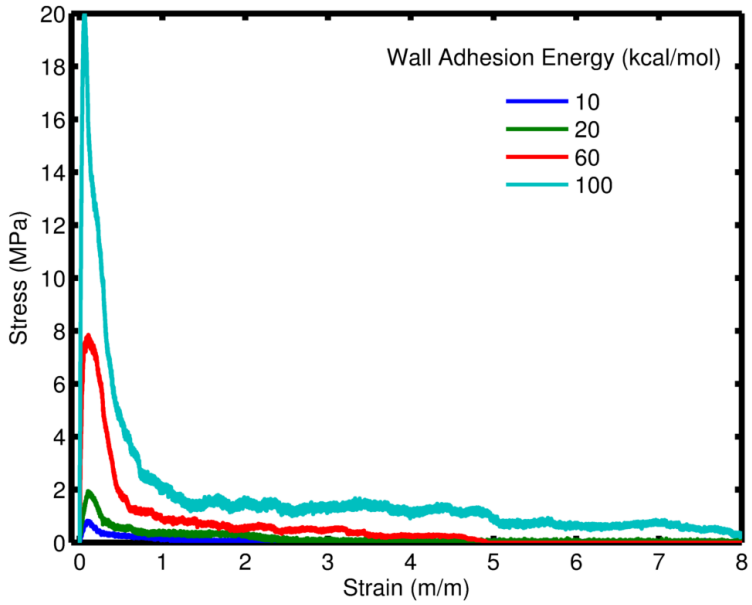

(a)

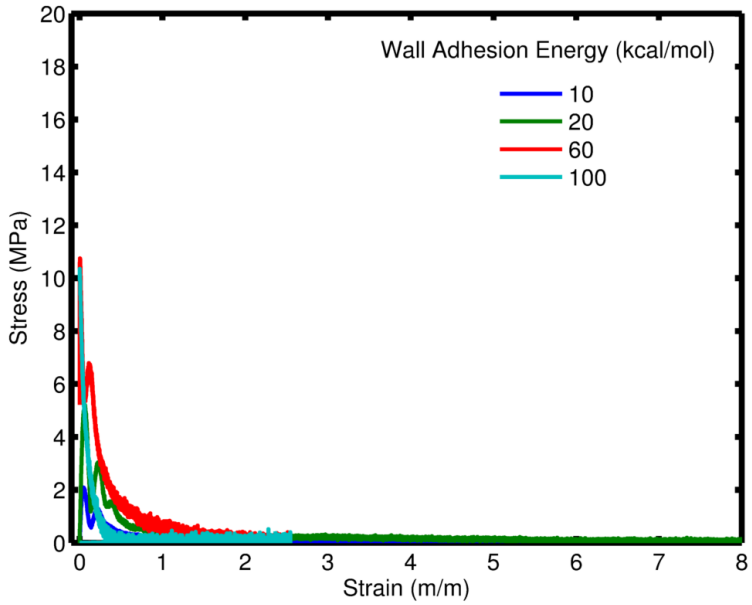

(b)

Figure 6-6: Stress-strain curves for (a) the Aβ based films and (b) the YadA based films. Both structures exhibit significant changes in their mechanical response with varied wall adhesion energies, and for the larger adhesion stregnths, the Aβ based films significantly outperform the YadA structures.

behave similarly to medium to highly crosslinked polymer films. In contrast, in the YadA fibril films, the interaction between the adhesive walls and the fibrils dominates the inter-fibril interactions and the films fail cohesively before significant deformation is applied. These deformation mechanisms are illustrated in Figure 6-7.

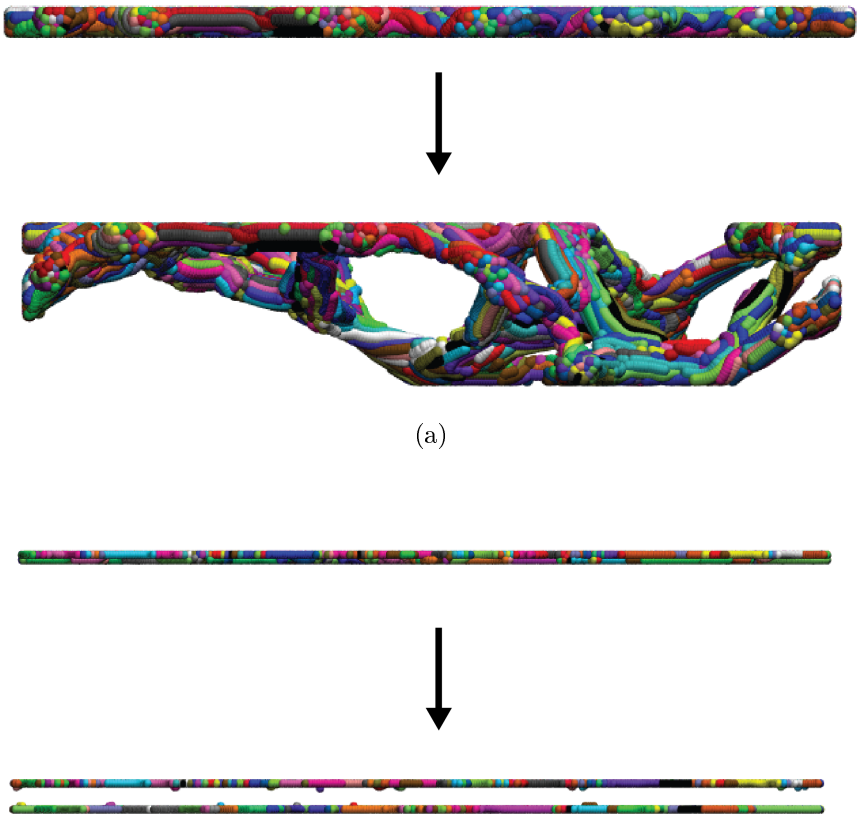

(a)

(b)

Figure 6-7: Deformation response of films comprising (a) the Aβ amyloid fibrils and (b) the YadA collagen binding fibrils. The stronger inter-fibril interactions in the Aβ structures result in increased cohesion and allow the structures to fail adhesively at relatively large strains. In contrast, the weak inter-fibril interactions in the YadA based fims lead to cohesive failure at small strains

Finally, the toughness modulus, measured as the area under the stress strain curves, is shown in Figure 6-8. The results demonstrate that for the smaller adhesion energies, the ability of the YadA based structure to deform via inter-fibril sliding

allows the structure to achieve a somewhat higher strain to failure than the Aβ based films, in which the much stronger inter-fibril interactions lead to adhesive failure very early in the adhesion test. As the adhesion strength is increased, however, the relatively weak interactions in the YadA films lead to cohesive failure at small strains, while the Aβ films are able to maintain cohesion resulting in significantly superior mechanical properties.

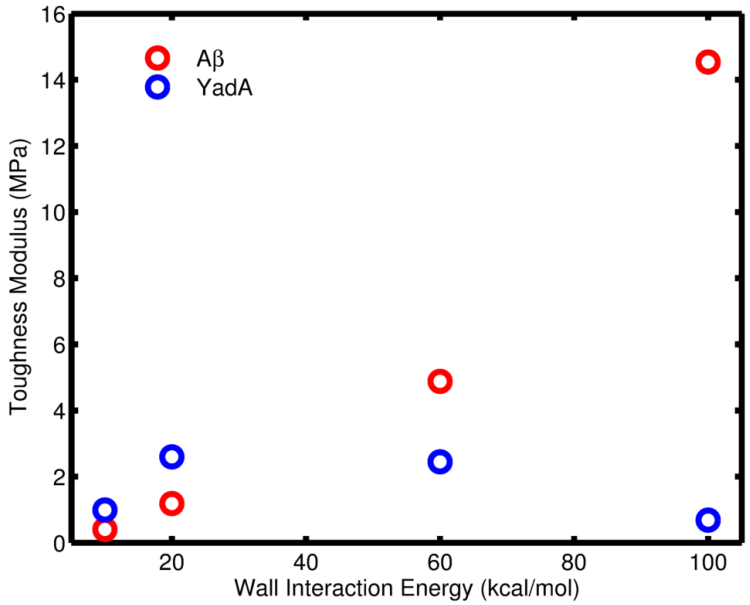

Figure 6-8: Toughness modulus vs. wall adhesion energy for the Aβ and YadA fibril based adhesive films. The much stronger interfibril interactions in the Aβ structures allow the films to maintain cohesion and significantly outperform the YadA based structures as the wall adhesion energy is increased.

6.3.3 Conclusions

Simulated tack tests were performed on coarse grained systems comprising films of two different amyloid or amyloid-like fibrils with four different adhesion strengths for the tack test substrate. As with the study of nanowire structures, the results exhibit significant dependance on the inter-fibril interaction strength, again indicating that the specific properties of the individual fibrils are not as important in determining the mesoscale response as are the inter-fibril properties. For the adhesive film structures,

the Aβ based films with their stronger inter-fibril interactions allow the films to maintain cohesion during the tack test and thus provide superior performance as the wall adhesion strength is increased.

Both film structures also exhibit significant variation in the adhesion response with variation of the wall adhesion strength. This again reinforces the idea that at the mesoscale, it is the inter-fibril interactions which dominate the overall mechanical response, and thus amyloid or amyloid-like fibrils should be chosen which optimize the properties based on these interactions.

6.4 Chapter Summary

This chapter presented some simple modeling efforts to understand how the molecular scale mechanics of single amyloid and amyloid-like fibrils translates into the mechanical performance of larger scale functional amyloid-based biomaterials. The coarse-grained model in this thesis was implemented to effectively compare the properties of mesoscale structures comprising two distinct amyloid fibrils with very different relative energy scales for the intra- and inter-fibril interactions.

Although amyloid fibrils are often noted for their excellent mechanical properties, the existence of new deformation mechanisms at the mesoscale (most notably inter-fibril sliding) results in a significant decrease in the mechanical performance of mesoscale assemblies of amyloid or amyloid-like fibrils. This also leads to a significant dependence of the mesoscale properties on the inter-fibril interaction strength. For both simple nanowire-like structures and more complex adhesive films, the inter-fibril interactions are found to be much more important than the intra-fibril interactions in determining the mesoscale mechanical response. Structures comprising fibrils which feature stronger inter-fibril interactions are generally found to perform better. This is likely due to the fact that stronger inter-fibril interactions limit the amount of inter-fibril sliding, and thus allow the larger scale structures to better utilize the strength and stiffness of the constituent fibrils.

Chapter 7

Conclusions

7.1 Summary of Key Findings and Significance

This thesis presented an investigation of the mechanics of amyloid and amyloid-like protein based materials at different length scales relevant to their hierarchical structures. A multiscale modeling and simulation approach was used to integrate the results of studies on disparate length scales into a more unified description of the mechanics of functional amyloid based materials, and to provide guidance in the development of new engineered amyloid-based and amyloid-inspired biomaterials for diverse applications.

The first step in understanding the structure-property relationships in amyloid and amyloid-like materials is understanding their behavior at the smallest length scale of their hierarchical structure. This was accomplished by performing full atomistic simulations on single amyloid and amyloid-like fibrils to directly probe their mechanical response. The cooperative deformation of hydrogen bonds forming the backbone of the cross-β structure was found to play a vital role in determining the overall mechanical response of the protein fibrils. Structures with a higher areal density of hydrogen bonds in the fibril cross-section were found to be the best performers. Although the specific geometry of the fibrils had a large effect on mechanical performance, it was not found to play a significant role in determining the deformation and failure behavior. Next the bending behavior of amyloid and amyloid-like fibrils was examined;

it was shown that beyond the shortest length scales where shear effects can influence the deformation response, the bending behavior of the fibrils is well described by classical bending theory. Finally the inter-fibril interactions were investigated through an atomistic scale shear test, and the strength of the interaction, and importantly the relative strength of the intra- versus inter-fibril interactions were found to vary greatly among the amyloid and amyloid-like structures investigated. This range of mechanical responses illustrates that amyloid and amyloid-like fibrils are a set of materials with a rich diversity of mechanical behaviors, and thus they provide an excellent set of building block materials for the design of functional biomaterials.

Next, these findings from atomistic scale simulations are synthesized into a coarse-grained description which is capable of elucidating structure-property relationships at larger length scales in the hierarchical structure of of amyloid and amyloid-like protein fibrils. This model captures the relevant physics of single fibrils observed at the atomistic scale, and is flexible in that it can be parameterized to study diverse amyloid and amyloid-like structures. The model was validated by comparing results to a three-point bending simulation to those of experiments performed on structures based on similar protein fibrils; the good agreement to the experimental results demonstrates the validity of the model as well as the methods used to train the model.

Since amyloids are widely regarded as being quite "sticky", much interest lies in utilizing them in engineered adhesives. Thus,n investigation into the adhesive performance of amorphous polymers was performed in order to identify fundamental features which enhance the performance of adhesive films. The properties of the films were modulated via crosslinking, which in the context of amyloid based materials, can be thought of as relating to the inter-fibril interaction strength. An optimum in the adhesive performance was identified at an intermediate crosslink density which corresponded to the transition from cohesive to adhesive failure. These results indicate that the response amyloid based or amyloid-inspired adhesives can be tuned via the strength of the inter-fibril interactions, and that optimal adhesive performance may be achieved in these materials by utilizing amyloid or amyloid-like fibrils which feature an inter-fibril interaction strength which is strong enough to improve the me-

chanical performance while not being so strong as to inhibit deformation and limit the overall adhesive performance.

Finally, the coarse-grained model developed in this thesis was implemented to directly study the deformation response and mechanical properties of mesoscale structures comprising two amyloid and amyloid-like fibrils, and to investigate the importance of the relative strength of the intra- versus inter-fibril interactions in determining the response of larger scale structures. A study of a nanowire-like geometry revealed that stronger inter-fibril interactions produce better performing structures, and that the intrinsic brittleness of the constituent amyloid fibrils does not limit the robustness of the larger scale structures. However, the existence of new deformation mechanisms at the mesoscale, notably inter-fibril sliding, results in a decrease in performance relative to the single fibril properties. Thin films based on these amyloid fibrils were also investigated to study their adhesive response. As with the nanowire structures, the inter-fibril interaction strength was found to significantly affect the response; films comprising weakly interacting fibrils fail cohesively before exhibiting useful adhesive properties, while more strongly interacting fibrils are able to maintain cohesion throughout the tack test and thus provide useful adhesive performance. The strength of the interaction with the adhesive substrate was also found to be significant in determining the adhesive response, especially in the case of the structures with stronger inter-fibril interactions. These results clearly demonstrate that although single amyloid or amyloid-like fibrils may exhibit impressive mechanical properties, the properties of mesoscale assemblies of the same fibrils are limited by the strength of the interactions between the fibrils; in many cases the inter-fibril interactions are not strong enough to allow the mesoscale structures to take advantage of the intrinsic strength and stiffness of the constituent fibrils. Thus when engineering functional amyloid based materials for mechanical purposes, careful attention must be paid to the inter-fibril interaction strength.

7.2 Opportunities for Future Work

The work presented in this thesis addressed the aims of the study outline in Section 1.4; however, amyloid and amyloid-like protein materials, as well as amyloid-inspired structures, comprise a very rich field with many opportunities for further research. This thesis developed uncovered some fundamental structure-property relationships in amyloid and amyloid-like structures, but many more effects can be considered, including strain rate, temperature, or environmental conditions including effects of different solvents or pH. The understanding of these effects could have an impact beyond functional amyloid-based materials, including in developing therapies for amyloid-based diseases. Furthermore, while the work described in Chapter 3 aimed to study diverse amyloid and amyloid-like geometries, the structures studied comprise only a small fraction of the known amyloid structures. Thus a more extensive investigation into additional amyloid and amyloid-like geometries may reveal further avenues for optimizing the mechanical response of the structures at the single fibril scale.

The application of the coarse-grained model developed in this thesis served as a proof of concept of the model, and although the mesoscale studies uncovered some basic design guidelines for the development of amyloid-based functional biomaterials, further application of the model for various amyloid and amyloid-like fibrils (including synthetic amyloid inspired structures such as those described in Section 1.3.1) could reveal strategies for optimizing the design of amyloid-based materials. Furthermore, since the inter-fibril interactions were found to be so important in determining the mesoscale response, much work could be done on understanding the specific atomistic scale features which control this response and ultimately could enable the response to be tuned. Structures such as cyclic peptide nanotubes which can be readily functionalized with crosslinkable polymer chains could provide a very interesting avenue to accomplish this tunability of the inter-fibril interactions, and such systems could be studied with only small modifications to the coarse grained model described in Chapter 4.

It is the hope of this author that the work discussed in this thesis will be built upon to truly inform and enable the design of myriad amyloid-based functional materials. These proteins, which have so long been studied for their destructive pathological roles, exhibit tremendous opportunity for forming the foundation of a new class of biomaterials with diverse applications, and their utilization in these roles could be greatly enhanced by further study.

Appendix A

Preliminary Coarse-Grained Modeling of Amyloid "Nanowires"

This chapter describes preliminary coarse-grained modeling efforts to understand simple deformation mechanisms in amyloid-based materials. The model is based on atomistic simulation results which were carried out under force-control boundary conditions, and thus the functional form of the model as well as the specific mechanical properties of the constituent amyloid fibrils do not match the results presented in Section 3.1 or the updated coarse-grained modeling efforts described in Chapter 4. Even so, the work in this chapter explores the interplay between intra- and inter-fibril interactions and the model used here, along with that described in Chapter 5, provide the foundation and motivation for the coarse-grained modeling described in Chapter 4.

The mesoscale structure studied in this work is a "nanowire" structure composed of many individual amyloid fibrils. Much theoretical work has been performed on similar geometries including bundles of carbon nanotubes, and it was shown that the properties of the bundle structures depend greatly on the properties of the constituent nanotubes (which vary due to both geometry and the presence of defects) [152–154]. While the nanowire studied here is a relatively simple structure, it can provide key insight into the dominant deformation mechanisms and elucidate trends that emerge upon varying the properties of the constituent amyloid fibrils.

A.1 Model and Methods

A.1.1 Mesoscale Amyloid Model

A coarse-grain model is used to enable the exploration of the mechanical response of amyloid structures that are beyond the size scale accessible with a fully atomistic description. Individual amyloid fibrils are described by a simple bead-spring model as described in a series of earlier papers [68, 107]. In this model three layers of the β-sheet structure of the amyloid fibril are represented by a single bead with an inter-bead separation of 1.272 nm; all parameters in that model were identified from full-atomistic simulations. The total energy of the system is given by

$$E_{Total} = E_{Bonds} + E_{Angles} + E_{NB} \tag{A.1}$$

where E_{Bonds} describes the axial deformation of the individual fibrils, E_{Angles} describes the bending deformation of the fibrils, and E_{NB} describes the non-bonded interactions which control inter-fibril adhesion.

The amyloid fibrils studied in this work feature a stiffening behavior in both compression and tension as determined from the force-controlled atomistic simulations [68]. For small deformation the elastic modulus is 2.34 GPa but for compressive strains exceeding 0.1% and tensile strains exceeding 0.2%, the modulus increases to 12.43 GPa and 18.05 GPa, respectively. To account for this behavior, the bonding energy is described by

$$E_{Bonds} = \sum_{Bonds} \varphi_b \tag{A.2}$$

$$\varphi_b = \frac{1}{2} \begin{cases} k_b^s \left(r_{stiff}^c - r_0\right)^2 + k_b^c \left(r - r_{stiff}^c\right)^2 & : r \leq r_{stiff}^c \\ k_b^s \left(r - r_0\right)^2 & : r_{stiff}^c < r < r_{stiff}^t \\ k_b^s \left(r_{stiff}^t - r_0\right)^2 + k_b^t \left(r - r_{stiff}^t\right)^2 & : r_{stiff}^t \leq r \leq r_{break} \\ k_b^s \left(r_{stiff}^t - r_0\right)^2 + k_b^t \left(r_{break} - r_{stiff}^t\right)^2 & : r > r_{break} \end{cases} \tag{A.3}$$

The parameters k_b^i are the spring constants for the relevant strain ranges (c for com-

pression, t for tension, and s for small strain) and are parameterized so that the fibrils have the moduli given above. The bending behavior of the amyloid fibrils is described by the harmonic angle potential; the total bending energy is given by:

$$E_{Angles} = \sum_{Angles} \varphi_a \tag{A.4}$$

$$\varphi_a = \frac{1}{2} k_\theta \left(\theta - \theta_0\right)^2 \tag{A.5}$$

A Lennard-Jones potential is used to model the non-bonded interactions which control the inter-fibril adhesion with

$$E_{NB} = \sum_{Pairs} \varphi_{LJ} \tag{A.6}$$

$$\varphi_{LJ} = 4A \left[\left(\frac{B}{r}\right)^{12} - \left(\frac{B}{r}\right)^{6} \right] \tag{A.7}$$

All amyloid fibrils studied in this work have an initial length of 100nm, and the nominal values of all parameters are given in Table A.1. This mesoscale model is implemented and run in the LAMMPS simulation package [149].

Table A.1: Summary of the parameters used for the mesoscale model of the Aβ (1-40) amyloid fibril

Parameter		Units	Nominal Value
Stiffness in small strain	k_b^s	kcal mol^{-1} Å^{-2}	18.72
Stiffness in compression	k_b^c	kcal mol^{-1} Å^{-2}	99.42
Stiffness in tension	k_b^t	kcal mol^{-1} Å^{-2}	144.37
Bending stiffness	k_θ	kcal mol^{-1}	4369.8
Equilibrium bead spacing	r_0	Å	12.72
Bead spacing for onset of stiffening in compression	r_{stiff}^c	Å	12.70
Bead spacing for onset of stiffening in tension	r_{stiff}^t	Å	12.75
Bead spacing for bond breaking	r_{break}	Å	12.78
Equilibrium angle	θ_0	Deg	180
LJ energy parameter	A	kcal mol^{-1}	27.94
LJ distance parameter	B	Å	38.15

A.1.2 Nanowire Assembly and Mechanical Characterization

To create the amyloid nanowire geometry used in this study, 100 coarse-grain amyloid fibrils, each 100 nm long, are randomly positioned along the nanowire axis. The fibrils are oriented along a random angle within 30 degrees of the fibril axis in both transverse directions, and the ends of the fibrils are placed within 10 Å of the nanowire axis. Energy minimization is performed to bring the fibrils together into a single structure followed by equilibration to eliminate any residual stress. Figure A-1(a) shows images of both the starting configuration with randomly oriented fibrils as well as the equilibrated structure. The initial length of the amyloid nanowire structure is approximately 575 nm.

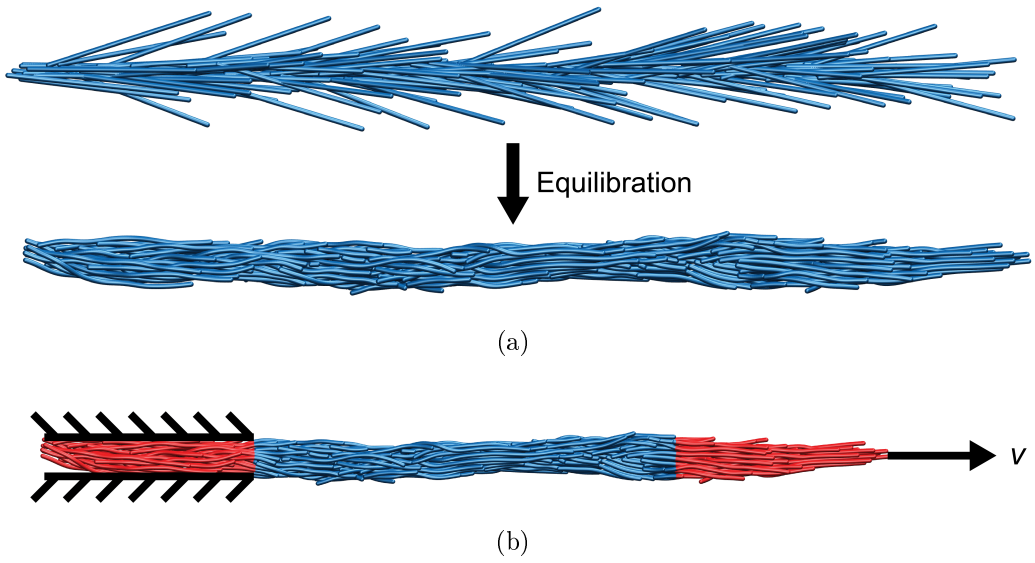

Figure A-1: Amyloid nanowire structure and boundary conditions. (a) shows the initial structure with randomly oriented fibrils as well as the nanowire structure after equilibration. (b) shows a schematic of the loading conditions used. The red sections are those to which the boundary conditions are applied. The left end is held fixed and the right end is moved at a constant displacement rate. The blue section in the middle is unconstrained and free to deform.

Two parameters are varied in order to examine the effect of the fibril properties on the response of the overall nanowire structure: the breaking strain (controlled by changing r_{break}) and the strength of the inter-fibril adhesion (A). The breaking strain is varied between approximately 0.8 and 2 times the nominal breaking strain (0.48%)

and the adhesion strength is varied between 0.1 and 3.5 times its nominal value. In all cases an additional equilibration run is performed after varying the fibril properties to ensure that each structure starts from a stress-free configuration.

The amyloid nanowire structures are subjected to uniaxial tension to examine their mechanical properties and deformation behavior. Deformation is applied by holding one end of the nanowire fixed and moving the other end at a constant velocity of 0.5 m/s as shown schematically in Figure A-1(b); the groups of particles to which the boundary conditions are applied are each approximately 150 nm in length. During pulling, both the virial stress and the engineering strain in the unfixed section are recorded. Since the virial stress is reported as a stress-volume product, all stress values are calculated by dividing by the initial volume of the free section of the nanowire with nominal fibril properties. Furthermore, to more clearly show changes in behavior that result from varying the fibril properties, all calculations are normalized by the results from the nominal fibril property nanowire structure. Visual analysis is performed with VMD [79] to examine changes in deformation mechanisms that result from varying the fibril properties.

A.2 Results and Discussion

A.2.1 Deformation Mechanisms

One of the most apparent changes that the amyloid nanowire structures undergo upon varying the fibril properties is seen in the mechanism by which they deform. Even when varying the fibril failure strain, the individual amyloid fibrils are always quite brittle —the maximum failure strain is below 1%. However, in the nanowire structure, deformation is not limited to axial stretching and bending as it is for single fibrils. Instead, deformation is controlled by a competition between two mechanisms: sliding of fibrils passed each other and failure of individual fibrils (due to axial stretching beyond the breaking strain).

In the case of the nominal fibril properties, the nanowire displays mostly brittle

behavior. While some fibril sliding is observed, the majority of the deformation is accommodated by failure of individual fibrils. As seen in Figure A-2(a), as the fibril breaking strain is increased and the individual fibrils become more resistant to failure, there is a clear transition to ductile behavior. Very little fibril failure is observed and the large amount of fibril sliding results in the nanowires exhibiting some necking before ultimately failing due to the finite length of the fibrils.

A similar transition between ductile and brittle behavior is observed upon varying the inter-fibril adhesion strength. For low adhesion strengths, there is little resistance to fibril sliding and the nanowires feature ductile behavior, but increasing the adhesion strength results in much more fibril failure and an overall brittle response in the nanowire as seen in Figure A-2(b).

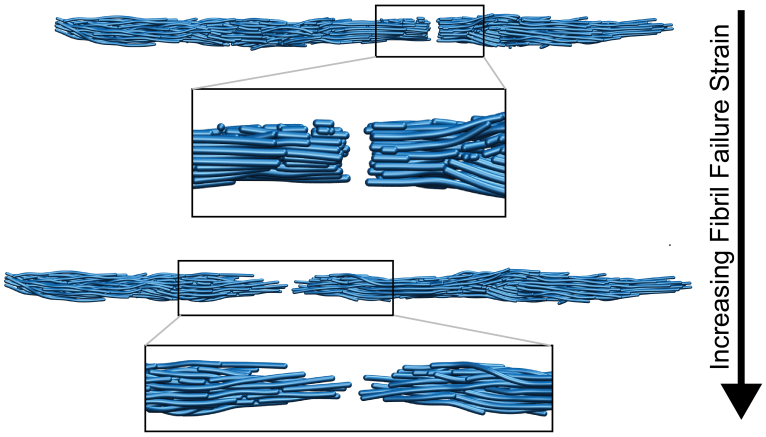

(a)

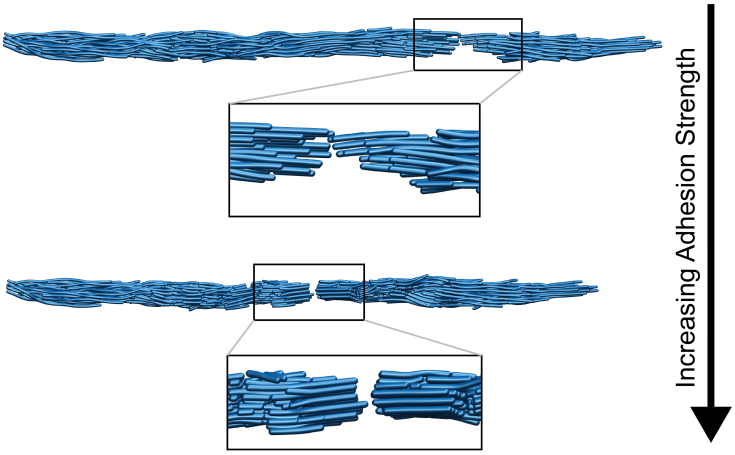

(b)

Figure A-2: The deformation mechanisms seen in the amyloid nanowires depend strongly on the properties of the fibrils. (a) shows the clear transition from brittle to ductile behavior that occurs upon increasing the fibril failure strain; the opposite trend is observed in (b) upon increasing the interfibral adhesion strength. For small fibril failure strains and large interfibral adhesion strength, deformation is dominated by failure of individual fibrils and the fracture surface of nanowire is mostly flat. In contrast, for large fibril failure strains and small interfibral adhesion strength, fibril sliding is the dominant deformation mechanism and a necking behavior is seen before failure.

A.2.2 Elastic Properties

The effect of varying the fibril properties on the Young's Modulus of the nanowire structures is examined next. To provide a consistent measure between all cases, the modulus is obtained by performing a linear fit on the stress-strain curve up to 0.05% strain. As seen in A-3(a), the fibril failure strain has little to no effect on the modulus of the nanowire. This result is not surprising; in the very small strain range from which the Young's Modulus is determined, the strain in individual fibrils does not exceed the breaking strain and thus the nanowire properties remain constant.

In contrast, varying the inter-fibril adhesion strength has a large effect on the modulus of the nanowire as seen in A-3(b). Increasing the adhesion strength reduces the ability of the fibrils to slide passed each other and thus results in an increased stiffness. These results indicate that in the elastic regime, the mechanical response of larger scale amyloid structures is dominated by the interactions between fibrils rather than the elastic properties of the fibrils themselves.

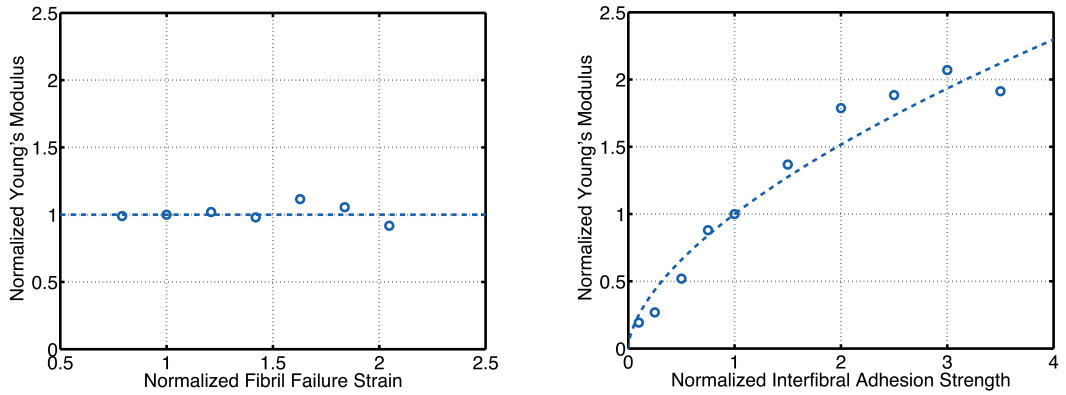

(a) (b)

Figure A-3: Effect of amyloid fibril properties on the Young's Modulus of the nanowire structure. (a) shows that varying the fibril failure strain has little effect on the modulus of the nanowire structure, while (b) shows that the interfibral adhesion strength strongly affects the nanowire modulus. The dashed lines in each panel qualitatively demonstrate the trends.

It is noted that the value found for the Young's modulus of the nanowire structure with the nominal fibril properties is 0.612 GPa, about one fourth of the modulus of

an individual fibril (in the small strain regime). This result is not surprising since the fibril sliding deformation mechanism in the nanowire allows the structure to deform without axially stretching the individual fibrils and thus significantly reduces the modulus of the larger structure.

A.2.3 Ultimate Strength and Failure Strain

Figure A-4 shows how the ultimate tensile strength and failure strain of the nanowires varies with the fibril properties. As expected, increasing the fibril breaking strain allows the nanowire to achieve a higher strength and strain to failure as seen in Figure A-4(a). However, since the deformation mechanism shifts to one dominated by fibrils sliding past each other as described above, once the fibril breaking strain is increased sufficiently such that the fibrils will always slide out before breaking, the ultimate strength and failure strain of the nanowires are not expected to continue to increase with increasing fibril failure strain. Instead they are limited by the amount of overlap among the fibrils in the structure. Nanowires constructed from longer fibrils or with a higher linear density of fibrils would be expected to achieve higher strains before failure, but these effects are not examined in this study.

The effect of the inter-fibril adhesion strength is shown in Figure A-4(b). The ultimate strength increases initially with increasing adhesion strength but levels off when the adhesion becomes too large because the strength of attraction between fibrils begins to exceed the strength of the bonds within the fibrils. This causes the fibrils to break even under small applied loads. The dramatic decrease of failure strain with increasing adhesion strength demonstrates the transition to brittle behavior and highlights the inherent tradeoff between enhanced strength and reduced ductility.

A.2.4 Toughness Modulus

Finally, the toughness modulus of the amyloid nanowires is calculated from these *in silico* experiments to explore how varying the fibril properties affects the ability of the structures to absorb energy during deformation. Since increasing the fibril fail-

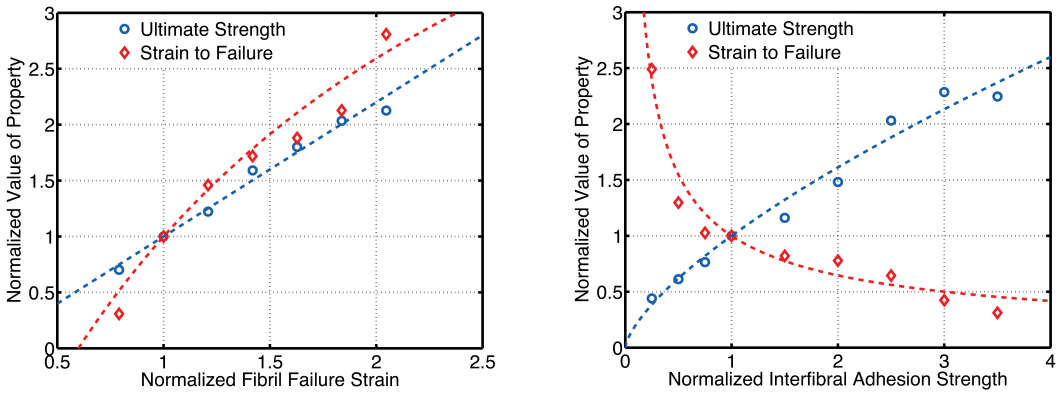

(a) (b)

Figure A-4: Variation of the ultimate tensile strength and strain to failure of the amyloid nanowire with varying amyloid fibril properties. (a) shows that increasing the failure strength of individual fibrils results in a higher ultimate strength and failure strain for the nanowire. In contrast, (b) demonstrates the tradeoff between enhanced strength and reduced ductility that occurs upon increasing the inter-fibril adhesion strength. The dashed lines in each panel qualitatively demonstrate the trends.

ure strain resulted in an increase in both the ultimate strength and strain to failure, it is not surprising that a large increase in the toughness modulus is also observed (Figure A-5(a)). This indicates that by finding ways to increase the failure strain of individual fibrils or by identifying amyloid or amyloid-like fibrils which posses this combination of properties (as discussed in Section 3.1), structures can be created that are very mechanically robust. In contrast, the tradeoff of enhanced strength and increased brittleness with increasing inter-fibril adhesion strength causes the toughness modulus to remain mostly unchanged over the range of adhesion strengths studied as shown in Figure A-5(b).

More notably, the toughness modulus of an individual amyloid fibril is indicated in each plot by the dashed red line, and in almost every case the toughness modulus of the nanowire structure exceeds that of the individual fibril. For the nanowire with nominal fibril properties, the toughness modulus is almost 2.5 times the value for the single fibril. Thus the robustness of larger scale structures is not limited by the brittle nature of the constituent fibrils; the existence of new deformation mechanisms such as fibril sliding in the nanowires provides an avenue to offset the brittleness of

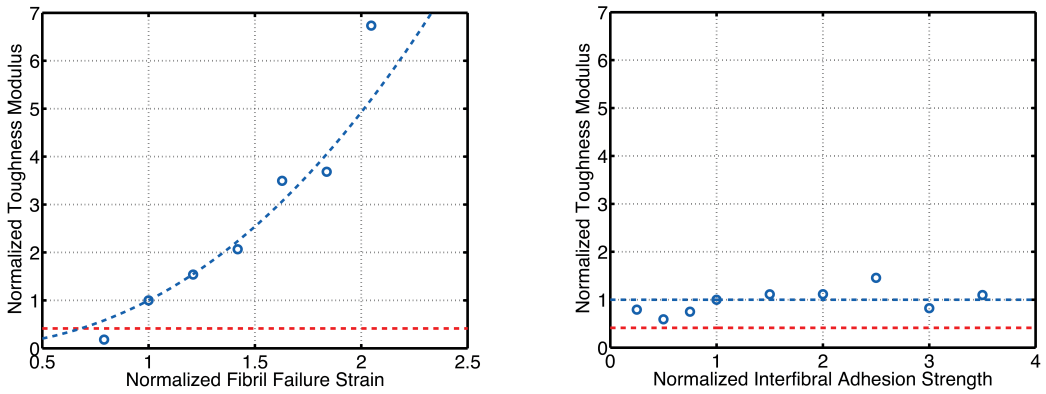

(a) (b)

Figure A-5: Effect of fibril properties on the toughness modulus of the amyloid nanowire structures. The dashed red line in each plot shows the toughness modulus of a single amyloid fibril. (a) clearly shows that increasing the fibril failure strain results in a large increase in the toughness modulus. However, due to competition between enhanced strength and reduced strain to failure, increasing the inter-fibril adhesion strength has little effect on the toughness modulus as shown in (b). Also noteworthy is the fact that in almost every case, the larger scale amyloid nanowire has a higher toughness modulus than the individual fibrils. The dashed blue lines in each plot qualitatively demonstrate the trends.

amyloid fibrils and increase their utility in large scale structures.

A.3 Conclusions and Chapter Summary

These results demonstrate a clear link between the properties of individual amyloid fibrils and the mechanical behavior of larger scale structures made from them. Small changes in either the fibril breaking strain or the inter-fibril adhesion strength result in dramatic changes in deformation mechanism and a transition from a rather brittle to a more ductile behavior, and changes in the mechanical properties of the nanowires are in general strongly correlated with the changing deformation mechanisms that result from varying the fibril properties. We also show that structures such as the nanowires studied in this work can be made from brittle building blocks like amyloid fibrils but still display ductility and robustness; and the emergence of new deformation mechanisms at larger length scales mitigates some of the brittleness of the individual

fibrils.

The scope of these results is not limited to amyloid protein fibrils. The large increase in performance that is observed upon increasing the fibril failure strain indicates that the use of other protein structures could give better results than amyloid fibrils for different applications. For example, β-helical protein fibrils such as those described in Chapter 3 possess a continuous covalently bonded backbone [155] which could allow them to reach much higher strains before failing, and thus nanowire structures made from them could have a very large toughness modulus.

Although the specific model for the amyloid fibrils used does not match what was found in Chapter 3, the results lay the groundwork for the updated coarse-grained modeling described in Chapter 6 and demonstrate a proof of concept that the diverse library of amyloid and amyloid-like fibrils could allow for the development of functional amyloid based biomaterials with tunable mechanical properties.

Appendix B

MATLAB Code for Coarse-Grained Model Fitting

This chapter includes the MATLAB code used to perform the brute-force parameter search method for the determination of the coarse grained model parameters which provide the best fit to the atomistic scale simulation results. The code for the bond potential parameterization is shown below; the code for the non-bonded potential parameterization is not shown as it is identical to the bond potential code with the exception that it only loops over a single parameter ε.

B.1 Main Code

```
clear all; close all; clc;

load averagepmf.mat; % Load atomistic scale results
count = 1;

% Define Search Interval for D Parameter
Dmin=10;
Dmax=80;
Dint=2;
totalD = ((Dmax-Dmin)/Dint) + 1;

% Define Search Interval for Alpha Parameter
alphamin = 0.25;
```

```
alphamax = .95;
alphaint = .05;
totalalpha = ((alphamax - alphamin)/alphaint)+1;

% Define Search Interval for Shift Parameter
smin = 0;
smax = 2;
sint =.1;
totals = ((smax -smin)/sint)+1;

total = totalD*totalalpha*totals

%% Perform Parameter Sweep
h= waitbar(0,'Running...');
for D = Dmin:Dint:Dmax

    for alpha = alphamin:alphaint:alphamax

        for shift = smin:sint:smax
            waitbar(count/total,h,['Running ',num2str(count),'/',num2str(total)])
            tic
            runlammps(D,alpha,shift); % Run Coarse-grained Simulation in LAMMPS
            processpull; % Process LAMMPS Output

            outarray(count,1) = D;
            outarray(count,2) = alpha;
            outarray(count,3) = shift;
            outarray(count,4) = sum((cgpmf- average_pmf.pmf).^2); % Calculate the
                square error

            count = count + 1;
            toc
        end
    end
end
%%

close(h)
% Determine parameters which minimize the square error
[c,I] = min(outarray(:,4));
minvals = outarray(I,:);
min_D = minvals(1);
min_alpha = minvals(2);
min_shift = minvals(3);
sprintf('D: %.3f  alpha: %.3f  shift: %.3f',min_D,min_alpha,min_shift)
```

```
58
59
60 runlammps(min_D,min_alpha,min_shift);
61 processpull;
62
63 plot_pmf;
64 save 'outaray.mat' outarray
```

B.2 Additional Functions

This section includes the code for the additional functions called by the main code above.

Run LAMMPS Simulation

```
1 function [] = runlammps(D,alpha,shift)
2 %% This function edits the LAMMPS input file to include the current model parameters
      from
3 $%% the parameter search loop and runs the LAMMPS simulation.
4 lammpscmd = 'lmp_29May14 < cgtest.in 1>NUL 2>NUL';
5 insed = ['sed -i ''28cbond_coeff 1 ',num2str(D),' ',num2str(alpha),' 14.4 ',num2str(
      shift), ''' cgtest.in'];
6
7 system(insed);
8 system(lammpscmd);
9 end
```

Process LAMMPS Output

```
1 %% This script proccess the output from LAMMPS and calculates the PMF from the
2 %% coarse-grained simulation.
3 pull_file_cmd = 'sed -i ''1,2d'' forces.pull';
4 system(pull_file_cmd);
5 a=load('forces.pull');
6 load averagepmf.mat
7 left = a(:,2);
8 right = a(:,3);
9 dispcg = right - left;
10 dispcg = (dispcg-dispcg(1));
11 force = -1*a(:,6);
12 [dispcg2,pmf] = calcPMF(dispcg,force);
13 cgpmf=zeros(size(average_pmf.pmf));
14 cgdisp=zeros(size(average_pmf.pmf));
```

```
for k = 1:length(average_pmf.disp)
    [c,I] = min(abs(average_pmf.disp(k)*10 - dispcg2));
    cgpmf(k) = pmf(I);
    cgdisp(k) = dispcg2(I);
end
```

Calulate PMF from LAMMPS Output

```
function [ disp2, pmf ] = calcPMF( disp,force )
%% This function calculates the potential of mean force (PMF) from an array
    containing
%% force-displacement data.
for i = 1:size(force,2)
    force1(:,i) = (force(1:end-1,i)+ force(2:end,i))/2;
    disp2(:,i) = disp(2:end,i);
    dx(:,i) = disp2(:,i) - disp(1:end-1,i);
    pmf(:,i) = cumsum(dx(:,i).*force1(:,i));
end


end
```

References

[1] D. J. Selkoe, "Folding proteins in fatal ways," *Nature*, vol. 426, no. 6968, pp. 900–904, 2003.

[2] C. M. Dobson, "Protein misfolding, evolution and disease," *Trends in Biochemical Sciences*, vol. 24, no. 9, pp. 329–332, 1999.

[3] C. M. Dobson, "Protein folding and misfolding," *Nature*, vol. 426, no. 6968, pp. 884–890, 2003.

[4] F. Chiti and C. M. Dobson, "Protein misfolding, functional amyloid, and human disease," *Annual Review of Biochemistry*, vol. 75, pp. 333–366, 2006.

[5] T. P. J. Knowles and M. J. Buehler, "Nanomechanics of functional and pathological amyloid materials," *Nature Nanotechnology*, vol. 6, no. 8, pp. 469–479, 2011.

[6] J. Sipe and A. Cohen, "Review: History of the amyloid fibril," *Journal of Structural Biology*, vol. 130, no. 2-3, pp. 88–98, 2000.

[7] A. Aguzzi, "Beyond the prion principle," *Nature*, vol. 459, no. 7249, pp. 924–925, 2009.

[8] S. K. Maji, M. H. Perrin, M. R. Sawaya, S. Jessberger, K. Vadodaria, R. A. Rissman, P. S. Singru, K. P. R. Nilsson, R. Simon, D. Schubert, D. Eisenberg, J. Rivier, P. Sawchenko, W. Vale, and R. Riek, "Functional amyloids as natural storage of peptide hormones in pituitary secretory granules," *Science*, vol. 325, no. 5938, pp. 328–332, 2009.

[9] M. R. Chapman, L. S. Robinson, J. S. Pinkner, R. Roth, J. Heuser, M. Hammar, S. Normark, and S. J. Hultgren, "Role of escherichia coli curli operons in directing amyloid fiber formation," *Science*, vol. 295, no. 5556, pp. 851–855, 2002.

[10] D. M. Fowler, A. V. Koulov, W. E. Balch, and J. W. Kelly, "Functional amyloid - from bacteria to humans," *Trends in Biochemical Sciences*, vol. 32, no. 5, pp. 217–224, 2007.

[11] M. J. Buehler, "Strength in numbers," *Nature Nanotechnology*, vol. 5, no. 3, pp. 172–174, 2010.

[12] C. P. Jaroniec, C. E. MacPhee, V. S. Bajaj, M. T. McMahon, C. M. Dobson, and R. G. Griffin, "High-resolution molecular structure of a peptide in an amyloid fibril determined by magic angle spinning nmr spectroscopy," *Proceedings of the National Academy of Sciences of the United States of America*, vol. 101, no. 3, pp. 711–716, 2004.

[13] T. Luhrs, C. Ritter, M. Adrian, D. Riek-Loher, B. Bohrmann, H. Doeli, D. Schubert, and R. Riek, "3d structure of alzheimer's amyloid-beta(1-42) fibrils," *Proceedings of the National Academy of Sciences of the United States of America*, vol. 102, no. 48, pp. 17342–17347, 2005.

[14] M. R. Sawaya, S. Sambashivan, R. Nelson, M. I. Ivanova, S. A. Sievers, M. I. Apostol, M. J. Thompson, M. Balbirnie, J. J. W. Wiltzius, H. T. McFarlane, A. O. Madsen, C. Riekel, and D. Eisenberg, "Atomic structures of amyloid cross-beta spines reveal varied steric zippers," *Nature*, vol. 447, no. 7143, pp. 453–457, 2007.

[15] S. Keten and M. J. Buehler, "Geometric confinement governs the rupture strength of h-bond assemblies at a critical length scale," *Nano Letters*, vol. 8, no. 2, pp. 743–748, 2008.

[16] S. Keten, Z. P. Xu, B. Ihle, and M. J. Buehler, "Nanoconfinement controls stiffness, strength and mechanical toughness of beta-sheet crystals in silk," *Nature Materials*, vol. 9, no. 4, pp. 359–367, 2010.

[17] S. R. Collins, A. Douglass, R. D. Vale, and J. S. Weissman, "Mechanism of prion propagation: Amyloid growth occurs by monomer addition," *Plos Biology*, vol. 2, no. 10, pp. 1582–1590, 2004.

[18] J. Shorter and S. Lindquist, "Destruction or potentiation of different prions catalyzed by similar hsp104 remodeling activities," *Molecular Cell*, vol. 23, no. 3, pp. 425–438, 2006.

[19] T. P. J. Knowles, T. W. Oppenheim, A. K. Buell, D. Y. Chirgadze, and M. E. Welland, "Nanostructured films from hierarchical self-assembly of amyloidogenic proteins," *Nature Nanotechnology*, vol. 5, no. 3, pp. 204–207, 2010.

[20] P. Fratzl and R. Weinkamer, "Nature's hierarchical materials," *Progress in Materials Science*, vol. 52, no. 8, pp. 1263–1334, 2007.

[21] T. P. Knowles, A. W. Fitzpatrick, S. Meehan, H. R. Mott, M. Vendruscolo, C. M. Dobson, and M. E. Welland, "Role of intermolecular forces in defining material properties of protein nanofibrils," *Science*, vol. 318, no. 5858, pp. 1900–1903, 2007.

[22] N. Kol, L. Adler-Abramovich, D. Barlam, R. Z. Shneck, E. Gazit, and I. Rousso, "Self-assembled peptide nanotubes are uniquely rigid bioinspired supramolecular structures," *Nano Letters*, vol. 5, no. 7, pp. 1343–1346, 2005.

[23] R. Paparcone and M. J. Buehler, "Microscale structural model of alzheimer a beta(1-40) amyloid fibril," *Applied Physics Letters*, vol. 94, no. 24, 2009.

[24] R. Paparcone and M. J. Buehler, "Failure of alzheimer's a beta(1-40) amyloid nanofibrils under compressive loading," *JOM*, vol. 62, no. 4, pp. 64–68, 2010.

[25] R. Paparcone, S. Keten, and M. J. Buehler, "Atomistic simulation of nanomechanical properties of alzheimer's a beta(1-40) amyloid fibrils under compressive and tensile loading," *Journal of Biomechanics*, vol. 43, no. 6, pp. 1196–1201, 2010.

[26] Z. P. Xu, R. Paparcone, and M. J. Buehler, "Alzheimer's a beta(1-40) amyloid fibrils feature size-dependent mechanical properties," *Biophysical Journal*, vol. 98, no. 10, pp. 2053–2062, 2010.

[27] J. F. Smith, T. P. J. Knowles, C. M. Dobson, C. E. MacPhee, and M. E. Welland, "Characterization of the nanoscale properties of individual amyloid fibrils," *Proceedings of the National Academy of Sciences of the United States of America*, vol. 103, no. 43, pp. 15806–15811, 2006.

[28] A. Aguzzi and L. Rajendran, "The transcellular spread of cytosolic amyloids, prions, and prionoids," *Neuron*, vol. 64, no. 6, pp. 783 – 790, 2009.

[29] L. Goldschmidt, P. K. Teng, R. Riek, and D. Eisenberg, "Identifying the amylome, proteins capable of forming amyloid-like fibrils," *Proceedings of the National Academy of Sciences of the United States of America*, vol. 107, no. 8, pp. 3487–3492, 2010.

[30] P. M. Tessier and S. Lindquist, "Unraveling infectious structures, strain variants and species barriers for the yeast prion [psi+]," *Nature Structural and Molecular Biology*, vol. 16, no. 6, pp. 598–605, 2009.

[31] R. Paparcone, J. Sanchez, and M. J. Buehler, "Comparative study of polymorphous alzheimer's a beta(1-40) amyloid nanofibrils and microfibers," *Journal of Computational and Theoretical Nanoscience*, vol. 7, no. 7, pp. 1279–1286, 2010.

[32] C. Wasmer, A. Lange, H. Van Melckebeke, A. B. Siemer, R. Riek, and B. H. Meier, "Amyloid fibrils of the het-s(218âĂŞ289) prion form a Îš solenoid with a triangular hydrophobic core," *Science*, vol. 319, no. 5869, pp. 1523–1526, 2008.

[33] R. Brookmeyer, E. Johnson, K. Ziegler-Graham, and H. M. Arrighi, "Forecasting the global burden of alzheimer's disease," *Alzheimers and Dementia*, vol. 3, no. 3, pp. 186–191, 2007.

[34] L. M. L. de Lau and M. M. B. Breteler, "Epidemiology of parkinson's disease," *Lancet Neurology*, vol. 5, no. 6, pp. 525–535, 2006.

[35] M. Meyer-Luehmann, T. L. Spires-Jones, C. Prada, M. Garcia-Alloza, A. de Calignon, A. Rozkalne, J. Koenigsknecht-Talboo, D. M. Holtzman, B. J. Bacskai, and B. T. Hyman, "Rapid appearance and local toxicity of amyloid-beta plaques in a mouse model of alzheimer's disease," *Nature*, vol. 451, no. 7179, pp. 720–U5, 2008.

[36] A. S. DeToma, S. Salamekh, A. Ramamoorthy, and M. H. Lim, "Misfolded proteins in alzheimer's disease and type ii diabetes," *Chemical Society Reviews*, vol. 41, no. 2, pp. 608–621, 2012.

[37] D. B. Teplow, N. D. Lazo, G. Bitan, S. Bernstein, T. Wyttenbach, M. T. Bowers, A. Baumketner, J. E. Shea, B. Urbanc, L. Cruz, J. Borreguero, and H. E. Stanley, "Elucidating amyloid beta-protein folding and assembly: A multidisciplinary approach," *Accounts of Chemical Research*, vol. 39, no. 9, pp. 635–645, 2006.

[38] J. Hardy and D. J. Selkoe, "Medicine - the amyloid hypothesis of alzheimer's disease: Progress and problems on the road to therapeutics," *Science*, vol. 297, no. 5580, pp. 353–356, 2002.

[39] D. M. Fowler, A. V. Koulov, C. Alory-Jost, M. S. Marks, W. E. Balch, and J. W. Kelly, "Functional amyloid formation within mammalian tissue," *Plos Biology*, vol. 4, no. 1, pp. 100–107, 2006.

[40] M. F. B. G. Gebbink, D. Claessen, B. Bouma, L. Dijkhuizen, and H. A. B. Wosten, "Amyloids - a functional coat for microorganisms," *Nature Reviews Microbiology*, vol. 3, no. 4, pp. 333–341, 2005.

[41] J. W. Kelly and W. E. Balch, "Amyloid as a natural product," *Journal of Cell Biology*, vol. 161, no. 3, pp. 461–462, 2003.

[42] J. Shorter and S. Lindquist, "Prions as adaptive conduits of memory and inheritance," *Nature Reviews Genetics*, vol. 6, no. 6, pp. 435–450, 2005.

[43] A. S. Mostaert, C. Giordani, R. Crockett, U. Karsten, R. Schumann, and S. P. Jarvis, "Characterisation of amyloid nanostructures in the natural adhesive of unicellular subaerial algae," *The Journal of Adhesion*, vol. 85, no. 8, pp. 465–483, 2009.

[44] N. D. Hammer, J. C. Schmidt, and M. R. Chapman, "The curli nucleator protein, csgb, contains an amyloidogenic domain that directs csga polymerization," *Proceedings of the National Academy of Sciences*, vol. 104, no. 30, pp. 12494–12499, 2007.

[45] S. Barrau, F. Zhang, A. Herland, W. Mammo, M. R. Andersson, and O. Inganas, "Integration of amyloid nanowires in organic solar cells," *Applied Physics Letters*, vol. 93, no. 2, 2008.

[46] T. Scheibel, R. Parthasarathy, G. Sawicki, X. M. Lin, H. Jaeger, and S. L. Lindquist, "Conducting nanowires built by controlled self-assembly of amyloid fibers and selective metal deposition," *Proceedings of the National Academy of Sciences of the United States of America*, vol. 100, no. 8, pp. 4527–4532, 2003.

[47] O. Carny, D. E. Shalev, and E. Gazit, "Fabrication of coaxial metal nanocables using a self-assembled peptide nanotube scaffold," *Nano Letters*, vol. 6, no. 8, pp. 1594–1597, 2006.

[48] R. Paparcone, M. A. Pires, and M. J. Buehler, "Mutations alter the geometry and mechanical properties of alzheimer's a beta(1-40) amyloid fibrils," *Biochemistry*, vol. 49, no. 41, pp. 8967–8977, 2010.

[49] C. X. Li, J. Adamcik, and R. Mezzenga, "Biodegradable nanocomposites of amyloid fibrils and graphene with shape-memory and enzyme-sensing properties," *Nature Nanotechnology*, vol. 7, no. 7, pp. 421–427, 2012.

[50] M. I. Solar and M. J. Buehler, "Composite materials: Taking a leaf from nature's book," *Nature Nanotechnology*, vol. 7, no. 7, pp. 417–419, 2012.

[51] J. D. Hartgerink, J. R. Granja, R. A. Milligan, and M. R. Ghadiri, "Self-assembling peptide nanotubes," *Journal of the American Chemical Society*, vol. 118, no. 1, pp. 43–50, 1996.

[52] K. Rosenthal-Aizman, G. Svensson, and A. UndÃľn, "Self-assembling peptide nanotubes from enantiomeric pairs of cyclic peptides with alternating d and l amino acid residues," *Journal of the American Chemical Society*, vol. 126, no. 11, pp. 3372–3373, 2004.

[53] L. Ruiz and S. , "Multiscale modeling of elasticity and fracture in organic nanotubes," *Journal of Engineering Mechanics*, vol. 140, no. 3, pp. 431–442, 2014.

[54] M. J. Buehler, *Atomistic Modeling of Materials Failure*. Springer US, 2008.

[55] B. J. Alder and T. E. Wainwright, "Studies in molecular dynamics i: General method," *Journal of Chemical Physics*, vol. 31, p. 459, 1959.

[56] A. Rahman, "Correlations in the motion of atoms in liquid argon," *Phys. Rev.*, vol. 136, 1964.

[57] A. D. MacKerell, D. Bashford, M. Bellott, R. L. Dunbrack, J. D. Evanseck, M. J. Field, S. Fischer, J. Gao, H. Guo, S. Ha, D. Joseph-McCarthy, L. Kuchnir, K. Kuczera, F. T. K. Lau, C. Mattos, S. Michnick, T. Ngo, D. T. Nguyen, B. Prodhom, W. E. Reiher, B. Roux, M. Schlenkrich, J. C. Smith, R. Stote, J. Straub, M. Watanabe, J. Wiorkiewicz-Kuczera, D. Yin, and M. Karplus, "All-atom empirical potential for molecular modeling and dynamics studies of proteins," *Journal of Physical Chemistry B*, vol. 102, no. 18, pp. 3586–3616, 1998.

[58] W. D. Cornell, P. Cieplak, C. I. Bayly, I. R. Gould, K. M. Merz, D. M. Ferguson, D. C. Spellmeyer, T. Fox, J. W. Caldwell, and P. A. Kollman, "A second generation force field for the simulation of proteins, nucleic acids, and organic molecules," *Journal of the American Chemical Society*, vol. 117, no. 19, pp. 5179–5197, 1995.

[59] S. L. Mayo, B. D. Olafson, and W. A. Goddard, "Dreiding: a generic force field for molecular simulations," *The Journal of Physical Chemistry*, vol. 94, no. 26, pp. 8897–8909, 1990.

[60] A. K. Rappe, C. J. Casewit, K. S. Colwell, W. A. Goddard, and W. M. Skiff, "Uff, a full periodic table force field for molecular mechanics and molecular dynamics simulations," *Journal of the American Chemical Society*, vol. 114, no. 25, pp. 10024–10035, 1992.

[61] M. Christen, P. H. HÃijnenberger, D. Bakowies, R. Baron, R. BÃijrgi, D. P. Geerke, T. N. Heinz, M. A. Kastenholz, V. KrÃďutler, C. Oostenbrink, C. Peter, D. Trzesniak, and W. F. van Gunsteren, "The gromos software for biomolecular simulation: Gromos05," *Journal of Computational Chemistry*, vol. 26, no. 16, 2005.

[62] W. L. Jorgensen and J. Tirado-Rives, "The opls [optimized potentials for liquid simulations] potential functions for proteins, energy minimizations for crystals of cyclic peptides and crambin," *Journal of the American Chemical Society*, vol. 110, no. 6, pp. 1657–1666, 1988.

[63] A. D. Mackerell, "Empirical force fields for biological macromolecules: Overview and issues," *Journal of Computational Chemistry*, vol. 25, no. 13, 2004.

[64]

[65] T. Ackbarow and M. J. Buehler, "Superelasticity, energy dissipation and strain hardening of vimentin coiled-coil intermediate filaments: atomistic and continuum studies," *Journal of Materials Science*, vol. 42, no. 21, pp. 8771–8787, 2007.

[66] S. Keten and M. J. Buehler, "Asymptotic strength limit of hydrogen-bond assemblies in proteins at vanishing pulling rates," *Physical Review Letters*, vol. 100, no. 19, 2008.

[67] S. Keten and M. J. Buehler, "Large deformation and fracture mechanics of a beta-helical protein nanotube: Atomistic and continuum modeling," *Computer Methods in Applied Mechanics and Engineering*, vol. 197, no. 41-42, pp. 3203–3214, 2008.

[68] R. Paparcone, S. Cranford, and M. J. Buehler, "Compressive deformation of ultralong amyloid fibrils," *Acta Mechanica Sinica*, vol. 26, no. 6, pp. 977–986, 2010.

[69] S. J. Marrink, H. J. Risselada, S. Yefimov, D. P. Tieleman, and A. H. de Vries, "The martini force field:âĂĽ coarse grained model for biomolecular simulations," *The Journal of Physical Chemistry B*, vol. 111, no. 27, pp. 7812–7824, 2007.

[70] L. Monticelli, S. K. Kandasamy, X. Periole, R. G. Larson, D. P. Tieleman, and S.-J. Marrink, "The martini coarse-grained force field: Extension to proteins," *Journal of Chemical Theory and Computation*, vol. 4, no. 5, pp. 819–834, 2008.

[71] T. Schneider and E. Stoll, "Molecular-dynamics study of a three-dimensional one-component model for distortive phase transitions," *Phys. Rev. B*, vol. 17, pp. 1302–1322, 1978.

[72] M. Solar and M. J. Buehler, "Comparative analysis of nanomechanics of protein filaments under lateral loading," *Nanoscale*, vol. 4, no. 4, pp. 1177–1183, 2012.

[73] F. C. Bernstein, T. F. Koetzle, G. J. B. Williams, E. F. Meyer, M. D. Brice, J. R. Rodgers, O. Kennard, T. Shimanouchi, and M. Tasumi, "Protein data bank - computer-based archival file for macromolecular structures," *Journal of Molecular Biology*, vol. 112, no. 3, pp. 535–542, 1977.

[74] W. Qiang, W. M. Yau, Y. Q. Luo, M. P. Mattson, and R. Tycko, "Antiparallel beta-sheet architecture in iowa-mutant beta-amyloid fibrils," *Proceedings of the National Academy of Sciences of the United States of America*, vol. 109, no. 12, pp. 4443–4448, 2012.

[75] H. Nummelin, M. C. Merckel, J. C. Leo, H. Lankinen, M. Skurnik, and A. Goldman, "The yersinia adhesin yada collagen-binding domain structure is a novel left-handed parallel beta-roll," *Embo Journal*, vol. 23, no. 4, pp. 701–711, 2004.

[76] A. J. Middleton, C. B. Marshall, F. Faucher, M. Bar-Dolev, I. Braslavsky, R. L. Campbell, V. K. Walker, and P. L. Davies, "Antifreeze protein from freeze-tolerant grass has a beta-roll fold with an irregularly structured ice-binding site," *Journal of Molecular Biology*, vol. 416, no. 5, pp. 713–724, 2012.

[77] K. Brown, F. Pompeo, S. Dixon, D. Mengin-Lecreulx, C. Cambillau, and Y. Bourne, "Crystal structure of the bifunctional n-acetylglucosamine 1-phosphate uridyltransferase from escherichia coli: a paradigm for the related pyrophosphorylase superfamily," *Embo Journal*, vol. 18, no. 15, pp. 4096–4107, 1999.

[78] H. Van Melckebeke, C. Wasmer, A. Lange, E. AB, A. Loquet, A. Bockmann, and B. H. Meier, "Atomic-resolution three-dimensional structure of het-s(218-289) amyloid fibrils by solid-state nmr spectroscopy," *Journal of the American Chemical Society*, vol. 132, no. 39, pp. 13765–13775, 2010.

[79] W. Humphrey, A. Dalke, and K. Schulten, "Vmd: Visual molecular dynamics," *Journal of Molecular Graphics and Modelling*, vol. 14, no. 1, pp. 33–38, 1996.

[80] H. J. C. Berendsen, D. Vanderspoel, and R. Vandrunen, "Gromacs - a message-passing parallel molecular-dynamics implementation," *Computer Physics Communications*, vol. 91, no. 1-3, pp. 43–56, 1995.

[81] B. Hess, C. Kutzner, D. van der Spoel, and E. Lindahl, "Gromacs 4: Algorithms for highly efficient, load-balanced, and scalable molecular simulation," *Journal of Chemical Theory and Computation*, vol. 4, no. 3, pp. 435–447, 2008.

[82] E. Lindahl, B. Hess, and D. van der Spoel, "Gromacs 3.0: a package for molecular simulation and trajectory analysis," *Journal of Molecular Modeling*, vol. 7, no. 8, pp. 306–317, 2001.

[83] D. Van der Spoel, E. Lindahl, B. Hess, G. Groenhof, A. E. Mark, and H. J. C. Berendsen, "Gromacs: Fast, flexible, and free," *Journal of Computational Chemistry*, vol. 26, no. 16, pp. 1701–1718, 2005.

[84] T. Darden, D. York, and L. Pedersen, "Particle mesh ewald - an n.log(n) method for ewald sums in large systems," *Journal of Chemical Physics*, vol. 98, no. 12, pp. 10089–10092, 1993.

[85] U. Essmann, L. Perera, M. L. Berkowitz, T. Darden, H. Lee, and L. G. Pedersen, "A smooth particle mesh ewald method," *Journal of Chemical Physics*, vol. 103, no. 19, pp. 8577–8593, 1995.

[86] W. G. Hoover, "Canonical dynamics - equilibrium phase-space distributions," *Physical Review A*, vol. 31, no. 3, pp. 1695–1697, 1985.

[87] S. Nose, "A unified formulation of the constant temperature molecular-dynamics methods," *Journal of Chemical Physics*, vol. 81, no. 1, pp. 511–519, 1984.

[88] S. Nose and M. L. Klein, "Constant pressure molecular-dynamics for molecular-systems," *Molecular Physics*, vol. 50, no. 5, pp. 1055–1076, 1983.

[89] M. Parrinello and A. Rahman, "Polymorphic transitions in single-crystals - a new molecular-dynamics method," *Journal of Applied Physics*, vol. 52, no. 12, pp. 7182–7190, 1981.

[90] B. Hess, H. Bekker, H. J. C. Berendsen, and J. G. E. M. Fraaije, "Lincs: A linear constraint solver for molecular simulations," *Journal of Computational Chemistry*, vol. 18, no. 12, pp. 1463–1472, 1997.

[91] B. Hess, "P-lincs: A parallel linear constraint solver for molecular simulation," *Journal of Chemical Theory and Computation*, vol. 4, no. 1, pp. 116–122, 2008.

[92] M. Sotomayor and K. Schulten, "Single-molecule experiments in vitro and in silico," *Science*, vol. 316, no. 5828, pp. 1144–1148, 2007.

[93] L. Ruiz, P. VonAchen, T. D. Lazzara, T. Xu, and S. Keten, "Persistence length and stochastic fragmentation of supramolecular nanotubes under mechanical force," *Nanotechnology*, vol. 24, no. 19, p. 195103, 2013.

[94] Z. Qin and M. J. Buehler, "Cooperative deformation of hydrogen bonds in beta-strands and beta-sheet nanocrystals," *Physical Review E*, vol. 82, no. 6, 2010.

[95] S. Keten, Z. P. Xu, and M. J. Buehler, "Triangular core as a universal strategy for stiff nanostructures in biology and biologically inspired materials," *Materials Science and Engineering C-Materials for Biological Applications*, vol. 31, no. 4, pp. 775–780, 2011.

[96] S. V. Strelkov, H. Herrmann, N. Geisler, T. Wedig, R. Zimbelmann, U. Aebi, and P. Burkhard, "Conserved segments 1a and 2b of the intermediate filament dimer: their atomic structures and role in filament assembly," *Embo Journal*, vol. 21, no. 6, pp. 1255–1266, 2002.

[97] Z. Qin, A. Fabre, and M. Buehler, "Structure and mechanism of maximum stability of isolated alpha-helical protein domains at a critical length scale," *The European Physical Journal E*, vol. 36, no. 5, 2013.

[98] M. T. Nelson, W. Humphrey, A. Gursoy, A. Dalke, L. V. Kale, R. D. Skeel, and K. Schulten, "Namd: A parallel, object oriented molecular dynamics program," *International Journal of Supercomputer Applications and High Performance Computing*, vol. 10, no. 4, pp. 251–268, 1996.

[99] J. J. Connor, *Introduction to structural motion control*. MIT-Prentice Hall series on civil, environmental, and systems engineering, Upper Saddle River, N.J.: Prentice Hall Pearson Education, Inc., 2003.

[100] P. J. Flory, *Statistical mechanics of chain molecules*. New York,: Interscience Publishers, 1969.

[101] M. J. Buehler, "Nature designs tough collagen: Explaining the nanostructure of collagen fibrils," *Proceedings of the National Academy of Sciences of the United States of America*, vol. 103, no. 33, pp. 12285–12290, 2006.

[102] M. A. Deriu, M. Soncini, M. Orsi, M. Patel, J. W. Essex, F. M. Montevecchi, and A. Redaelli, "Anisotropic elastic network modeling of entire microtubules," *Biophysical Journal*, vol. 99, no. 7, pp. 2190–2199, 2010.

[103] R. Paparcone and M. J. Buehler, "Failure of a beta(1-40) amyloid fibrils under tensile loading," *Biomaterials*, vol. 32, no. 13, pp. 3367–3374, 2011.

[104] Z. P. Xu and M. J. Buehler, "Mechanical energy transfer and dissipation in fibrous beta-sheet-rich proteins," *Physical Review E*, vol. 81, no. 6, 2010.

[105] P. Papadopoulos, I. Schnell, I. Lieberwirth, T. Q. Nguyen, H. A. Klok, and G. Floudas, "Thermodynamic confinement and alpha-helix persistence length in poly(gamma-benzyl-l-glutamate)-b-poly(dimethyl siloxane)-b-poly(gamma-benzyl-l-glutamate) triblock copolymers," *Biomacromolecules*, vol. 7, no. 2, pp. 618–626, 2006.

[106] T. Su and P. K. Purohit, "Fluctuating elastic filaments under distributed loads," *Molecular and Cellular Biomechanics*, vol. 8, no. 3, 2011.

[107] R. Paparcone, S. W. Cranford, and M. J. Buehler, "Self-folding and aggregation of amyloid nanofibrils," *Nanoscale*, vol. 3, no. 4, pp. 1748–1755, 2011.

[108] A. Magno, R. Pellarin, and A. Caflisch, "Mechanisms and kinetics of amyloid aggregation investigated by a phenomenological coarse-grained model," in *Computational Modeling of Biological Systems* (N. V. Dokholyan, ed.), Biological and Medical Physics, Biomedical Engineering, pp. 191–214, Springer US, 2012.

[109] G. Yoon, J. Kwak, J. I. Kim, S. Na, and K. Eom, "Mechanical characterization of amyloid fibrils using coarse-grained normal mode analysis," May 2011.

[110] W. M. Brown, P. Wang, S. J. Plimpton, and A. N. Tharrington, "Implementing molecular dynamics on hybrid high performance computers - short range forces," *Comp. Phys. Comm.*, vol. 182, pp. 898–911, 2011.

[111] W. M. Brown, A. Kohlmeyer, S. J. Plimpton, and A. N. Tharrington, "Implementing molecular dynamics on hybrid high performance computers - particle-particle particle-mesh," *Comp. Phys. Comm.*, vol. 183, pp. 449–459, 2012.

[112] W. M. Brown and Y. Masako, "Implementing molecular dynamics on hybrid high performance computers - three-body potentials," *Comp. Phys. Comm.*, vol. 184, pp. 2785–2793, 2013.

[113] S. Izvekov and G. A. Voth, "A multiscale coarse-graining method for biomolecular systems," *The Journal of Physical Chemistry B*, vol. 109, no. 7, pp. 2469–2473, 2005.

[114] A. M. Kosevich, E. M. Lifshitz, L. D. Landau, and L. P. Pitaevskii, *Theory of Elasticity*. Butterworth-Heinemann, 1986.

[115] N. M. Pugno, S. W. Cranford, and M. J. Buehler, "Synergistic material and structure optimization yields robust spider web anchorages," *Small*, vol. 9, no. 16, p. 2747, 2012.

[116] S. W. Cranford, A. Tarkanova, N. M. Pugno, and M. J. Buehler, "Nonlinear material behaviour of spider silk yields robust webs," *Nature*, vol. 482, no. 7383, p. 72, 2012.

[117] D. E. Barlow, G. H. Dickinson, B. Orihuela, J. L. Kulp, D. Rittschof, and K. J. Wahl, "Characterization of the adhesive plaque of the barnacle balanus amphitrite: Amyloid-like nanofibrils are a major component," *Langmuir*, vol. 26, no. 9, pp. 6549–6556, 2010.

[118] M. J. Buehler, H. M. Yao, H. J. Gao, and B. H. Ji, "Cracking and adhesion at small scales: atomistic and continuum studies of flaw tolerant nanostructures," *Modelling and Simulation in Materials Science and Engineering*, vol. 14, no. 5, pp. 799–816, 2006.

[119] V. Sahni, T. A. Blackledge, and A. Dhinojwala, "A review on spider silk adhesion," *Journal of Adhesion*, vol. 87, no. 6, pp. 595–614, 2011.

[120] Z. Qin and M. J. Buehler, "Molecular mechanics of mussel adhesion proteins," *Journal of the Mechanics and Physics of Solids*, vol. 62, pp. 19 – 30, 2014.

[121] Z. Qin and M. J. Buehler, "Impact tolerance in mussel thread networks by heterogeneous material distribution," *Nature Communications*, vol. 4, no. 2187, 2013.

[122] M. J. Buehler, "Tu(r)ning weakness into strength," *Nano Today*, vol. 5, pp. 379–383, 2010.

[123] C. Creton, "Pressure-sensitive adhesives: An introductory course," *Mrs Bulletin*, vol. 28, no. 6, pp. 434–439, 2003.

[124] M. A. Krenceski and J. F. Johnson, "Shear, tack, and peel of polyisobutylene - effect of molecular-weight and molecular-weight distribution," *Polymer Engineering and Science*, vol. 29, no. 1, pp. 36–43, 1989.

[125] I. Khan and B. T. Poh, "Natural rubber-based pressure-sensitive adhesives: A review," *Journal of Polymers and the Environment*, vol. 19, no. 3, pp. 793–811, 2011.

[126] C. Gay and L. Leibler, "On stickiness," *Physics Today*, vol. 52, no. 11, pp. 48–52, 1999.

[127] A. Zosel, "Adhesive failure and deformation-behavior of polymers," *Journal of Adhesion*, vol. 30, no. 1-4, pp. 135–149, 1989.

[128] C. Dahlquist, *Pressure-Sensitive Adhesives*, pp. 219–260. New York: Marcel Dekker, 1969.

[129] A. N. Gent and J. Schultz, "Effect of wetting liquids on strength of adhesion of viscoelastic materials," *Journal of Adhesion*, vol. 3, no. 4, 1972.

[130] B. T. Poh, Y. F. Giam, and F. P. A. Yeong, "Tack and shear strength of adhesives prepared from styrene-butadiene rubber (sbr) using gum rosin and petro resin as tackifiers," *Journal of Adhesion*, vol. 86, no. 8, pp. 844–856, 2010.

[131] B. T. Poh and A. T. Yong, "Effect of molecular weight of epoxidized natural rubber on shear strength of adhesives," *Journal of Applied Polymer Science*, vol. 114, no. 6, pp. 3976–3979, 2009.

[132] B. T. Poh and A. T. Yong, "Effect of molecular weight of rubber on tack and peel strength of smr l-based pressure-sensitive adhesives using gum rosin and petroresin as tackifiers," *Journal of Macromolecular Science Part a-Pure and Applied Chemistry*, vol. 46, no. 1, pp. 97–103, 2009.

[133] B. T. Poh and A. T. Yong, "Dependence of peel adhesion on molecular weight of epoxidized natural rubber," *Journal of Adhesion*, vol. 85, no. 7, pp. 435–446, 2009.

[134] B. T. Poh, P. G. Lee, and S. C. Chuah, "Adhesion property of epoxidized natural rubber (enr)-based adhesives containing calcium carbonate," *Express Polymer Letters*, vol. 2, no. 6, pp. 398–403, 2008.

[135] H. Lakrout, C. Creton, D. C. Ahn, and K. R. Shull, "Influence of molecular features on the tackiness of acrylic polymer melts," *Macromolecules*, vol. 34, no. 21, pp. 7448–7458, 2001.

[136] M. Sherriff, R. W. Knibbs, and P. G. Langley, "Mechanism for action of tackifying resins in pressure-sensitive adhesives," *Journal of Applied Polymer Science*, vol. 17, no. 11, pp. 3423–3438, 1973.

[137] S. D. Tobing and A. Klein, "Molecular parameters and their relation to the adhesive performance of emulsion acrylic pressure-sensitive adhesives. ii. effect of crosslinking," *Journal of Applied Polymer Science*, vol. 79, no. 14, pp. 2558–2564, 2001.

[138] A. Zosel, "Effect of cross-linking on tack and peel strength of polymers," *Journal of Adhesion*, vol. 34, no. 1-4, pp. 201–209, 1991.

[139] R. Auhl, R. Everaers, G. S. Grest, K. Kremer, and S. J. Plimpton, "Equilibration of long chain polymer melts in computer simulations," *Journal of Chemical Physics*, vol. 119, no. 24, pp. 12718–12728, 2003.

[140] K. Kremer and G. S. Grest, "Dynamics of entangled linear polymer melts - a molecular-dynamics simulation," *Journal of Chemical Physics*, vol. 92, no. 8, pp. 5057–5086, 1990.

[141] S. W. Sides, G. S. Grest, and M. J. K. Stevens, "Large-scale simulation of adhesion dynamics for end-grafted polymers," *Macromolecules*, vol. 35, no. 2, pp. 566–573, 2002.

[142] S. W. Sides, G. S. Grest, M. J. Stevens, and S. J. Plimpton, "Effect of end-tethered polymers on surface adhesion of glassy polymers," *Journal of Polymer Science Part B-Polymer Physics*, vol. 42, no. 2, pp. 199–208, 2004.

[143] M. J. Stevens, "Manipulating connectivity to control fracture in network polymer adhesives," *Macromolecules*, vol. 34, no. 5, pp. 1411–1415, 2001.

[144] M. J. Stevens, "Interfacial fracture between highly cross-linked polymer networks and a solid surface: Effect of interfacial bond density," *Macromolecules*, vol. 34, no. 8, pp. 2710–2718, 2001.

[145] M. Tsige, C. D. Lorenz, and M. J. Stevens, "Role of network connectivity on the mechanical properties of highly cross-linked polymers," *Macromolecules*, vol. 37, no. 22, pp. 8466–8472, 2004.

[146] M. Tsige and M. J. Stevens, "Effect of cross-linker functionality on the adhesion of highly cross-linked polymer networks: A molecular dynamics study of epoxies," *Macromolecules*, vol. 37, no. 2, pp. 630–637, 2004.

[147] W. J. Xia and S. Keten, "Coupled effects of substrate adhesion and intermolecular forces on polymer thin film glass-transition behavior," *Langmuir*, vol. 29, no. 41, pp. 12730–12736, 2013.

[148] W. J. Xia, S. Mishra, and S. Keten, "Substrate vs. free surface: Competing effects on the glass transition of polymer thin films," *Polymer*, vol. 54, no. 21, pp. 5942–5951, 2013.

[149] S. Plimpton, "Fast parallel algorithms for short-range molecular-dynamics," *Journal of Computational Physics*, vol. 117, no. 1, pp. 1–19, 1995.

[150] Marsagli.G, "Choosing a point from surface of a sphere," *Annals of Mathematical Statistics*, vol. 43, no. 2, p. 645, 1972.

[151] B. Lestriez, H. Lakrout, A. Criche, A. Roos, and C. Creton, "Probe tack tests as a characterization tool in pressure-sensitve-adhesives,"

[152] N. M. Pugno, "The role of defects in the design of space elevator cable: From nanotube to megatube," *Acta Materialia*, vol. 55, no. 15, pp. 5269–5279, 2007.

[153] N. M. Pugno, "Space elevator: Out of order?," *Nano Today*, vol. 2, no. 6, pp. 44–47, 2007.

[154] N. M. Pugno, "The design of self-collapsed super-strong nanotube bundles," *Journal of the Mechanics and Physics of Solids*, vol. 58, no. 9, pp. 1397–1410, 2010.

[155] D. L. Cox, H. Lashuel, K. Y. C. Lee, and R. R. P. Singh, "The materials science of protein aggregation," *Mrs Bulletin*, vol. 30, no. 6, pp. 452–457, 2005.